Generation and Characterization of Substructures in Graphene

Inaugural-Dissertation
to obtain the academic degree
Doctor rerum naturalium (Dr. rer. nat.)

submitted to the Department of Biology, Chemistry,
Pharmacy of Freie Universität Berlin

by

Fabian Grote

May 2024

The work presented in this dissertation was carried out from November 2019 to May 2024 at Freie Universität Berlin in the Department of Biology, Chemistry and Pharmacy under the supervision of Prof. Dr. Siegfried Eigler.

1st reviewer: Prof. Dr. Siegfried Eigler (Freie Universität Berlin)
2nd reviewer: Prof. Dr. Kannan Balasubramanian (Humboldt-Universität zu Berlin)

Date of defense: 10.10.2024

.

To my family

Table of Contents

1 Summary

1.1 Overview of Presented Topics

In this cumulative dissertation the following topics are presented:

1. The photochemical reaction of defect-free graphene with iodine and characterization of the resulting *trans*-oligoene substructures in the graphene lattice
2. The influence of lattice defects on the formation of *trans*-oligoene substructures in graphene

1.2 Overview of Collaborations

The research was conducted in collaboration with the research groups of:

- Prof. Dr. Kirill I. Bolotin, Department of Physics, FU Berlin
- Dr. Patryk Kusch, Department of Physics, FU Berlin

The detailed results and experimental information can be found in the attached publications in section 6.1 and 6.2.

1.3 Summary of Results

The covalent functionalization of graphene allows to tailor the properties of graphene by opening a bandgap and controlling the chemical structure and is therefore under extensive investigation. Radical addition reactions of halogens such as fluorine and chlorine are among the most common reactions, while iodine has so far not shown any reaction with high-quality graphene due to its lower reactivity.

This work demonstrates the first photochemical reaction between defect-free graphene and iodine and provides a reaction mechanism for this unique reactivity. Novel Raman modes with unprecedented intensity were observed after the reaction that exceeded graphene's characteristic signals. Therefore, the first part of this work focuses on elucidating the properties of the novel material and understanding the observed reactivity. For this, graphene was reacted with iodine and Raman spectra were recorded with various excitation energies showing the dispersive nature of the new Raman signals and a lack of graphene D-mode formation despite a coverage of around one iodine atom per 300 carbon atoms, as measured by X-ray photoelectron spectroscopy. The high temperature of 400 °C needed for the reverse reaction signifies a thermodynamically stable structure, and transport measurements (in collaboration with Prof. Kirill I. Bolotin) revealed a strong hysteresis and a p-doping effect exceeding non-covalent iodine doping that was further confirmed by Kelvin probe force microscopy (in collaboration with Dr. Patryk Kusch). Based on these observations a reaction mechanism was proposed where the bulky iodine radicals selectively add to graphene by blocking the most reactive addition sites close to them and form *trans*-oligoene substructures by isolation of

double bonds between sp^3-defects. Based on these results, the influence of lattice defects on *trans*-oligoene substructure formation was explored using graphene with defined defect densities. It was confirmed that no Raman-active defects are introduced by the reaction and that substructure formation can occur in graphene with lattice defects. Due to their own set of characteristic Raman signals and the lack of contribution to the graphene D-mode *trans*-oligoene substructures could be monitored relative to the defect density. Statistical Raman analysis clearly showed the strong hinderance of substructure formation by lattice defects and a critical defect spacing of around 1 nm, below which no substructure formation is observed. This explains the absence of substructures in previous studies using highly defective graphene. It also defines a lower length limit of substructures observed at 532 nm excitation wavelength and comparison with model molecules suggest an average substructure length of about eleven double bonds. The formation of the *trans*-oligoene substructure demonstrates the importance of addend size and shape for regioselective addition reactions that was previously only achieved by supramolecular networks of complex organic molecules. This work further establishes the use of this novel functionality as a strong p-dopant that can be easily fabricated by laser patterning. The crucial discovery of a model system with strong spectroscopic signals will allow further investigation of substructure formation and the improved methodology for statistical analysis of separate structures in graphene with Raman spectroscopy provides a powerful tool for future research.

1.4 Zusammenfassung der Ergebnisse

Diese kumulative Dissertation beschreibt die erste Untersuchung von *trans*-Oligoen Substrukturen in Graphen, die durch die Reaktion von Graphen mit Iod erzeugt wurden. Des Weiteren wurde der Einfluss von Gitterdefekten auf die Bildung von *trans*-Oligoen-Substrukturen in Graphen untersucht.
Die Forschung wurde in Zusammenarbeit mit den Gruppen von Prof. Dr. Kirill I. Bolotin und Dr. Patryk Kusch vom Fachbereich Physik der Freien Universität Berlin durchgeführt.
Die ausführlichen Ergebnisse und experimentelle Informationen finden sich in den Publikationen in den Abschnitten 6.1 und 6.2.

Die kovalente Funktionalisierung von Graphen wird intensiv untersucht da es ermöglicht die Eigenschaften durch Öffnen einer Bandlücke und Kontrolle der chemischen Struktur anzupassen. Radikal-Additionsreaktionen von Halogenen wie Fluor und Chlor gehören zu den am häufigsten untersuchten Reaktionen, während Iod aufgrund seiner geringeren Reaktivität bisher keine Reaktion mit defektfreiem Graphen gezeigt hat.
Diese Arbeit beschreibt die erste photochemische Reaktion zwischen defektfreiem Graphen und Iod und liefert einen Reaktionsmechanismus für die einzigartige beobachtete Reaktivität. Nach der Reaktion wurden neuartige Raman-Moden mit beispielloser Intensität beobachtet, die über die Intensität der charakteristischen Signale von Graphen hinausgehen. Daher konzentrierte sich der erste Teil dieser Arbeit darauf, die Eigenschaften des neuartigen Materials aufzuklären und die beobachtete Reaktivität zu verstehen. Dazu wurde Graphen mit

Iod umgesetzt und Raman-Spektren mit verschiedenen Anregungsenergien gemessen, die die dispersive Natur der neuen Raman-Signale aufzeigten. Trotz einer Bedeckung von etwa einem Iod-Atom pro 300 Kohlenstoffatome, wie durch Röntgen-Photoelektronen-Spektroskopie gemessen, trat keine Graphen-D-Mode auf. Die hohe Temperatur von 400 °C, die für die Umkehrreaktion erforderlich ist, deutet auf eine thermodynamisch stabile Struktur hin, und Transportmessungen (in Zusammenarbeit mit Prof. Kirill I. Bolotin) ergaben eine starke Hysterese sowie einen p-Dotierungseffekt, der über die nicht-kovalente Dotierung mit Iod hinausgeht. Dies konnte zudem durch Raster-Kelvin-Mikroskopie (in Zusammenarbeit mit Dr. Patryk Kusch) mit einer komplementären Technik bestätigt werden. Auf der Grundlage dieser Beobachtungen wurde ein Reaktionsmechanismus vorgeschlagen, bei dem die sterisch anspruchsvollen Iodradikale selektiv an das Graphen addieren, indem sie die reaktivsten Additionsstellen in ihrer Nähe blockieren und *trans*-Oligoen-Substrukturen durch Isolierung von Doppelbindungen zwischen sp^3-Defekten bilden. Auf der Grundlage dieser Ergebnisse wurde anschließend der Einfluss von Gitterdefekten auf die Bildung von *trans*-Oligoen-Substrukturen mit Hilfe von Graphen mit definierten Defektdichten untersucht. Es wurde bestätigt, dass durch die Reaktion keine Raman-aktiven Defekte eingeführt werden und dass die Substrukturbildung in Graphen mit Gitterdefekten stattfinden kann. Aufgrund ihres eigenen Satzes charakteristischer Raman-Signale und des fehlenden Beitrags zur Graphen-D-Mode konnte die Bildung von *trans*-Oligoen-Substrukturen als Funktion der Defektdichte verfolgt werden. Die statistische Raman-Analyse zeigte deutlich die starke Hinderung der Substrukturbildung durch Gitterdefekte und einen kritischen Defektabstand von etwa 1 nm, unterhalb dessen keine Substrukturbildung beobachtet werden konnte. Dies erklärt das Fehlen von Substrukturen in früheren Studien, in denen hochdefektes Graphen verwendet wurde. Dieser Defektabstand definiert auch eine untere Längengrenze für Substrukturen, die bei einer Laserwellenlänge von 532 nm beobachtet werden, und der Vergleich mit Modellmolekülen lässt auf eine durchschnittliche Substrukturlänge von etwa elf Doppelbindungen schließen. Die Bildung von *trans*-Oligoen-Substrukturen zeigt die Bedeutung der Größe und Form von Addenden für die Regioselektivität auf, die bisher nur durch supramolekulare Netzwerke komplexer organischer Moleküle erreicht werden konnte. Des Weiteren zeigt diese Arbeit die Verwendung dieser neuen Art von Funktionalität für die p-Dotierung von Graphen auf, das durch Laserstrukturierung einfach hergestellt werden kann. Die wesentliche Entdeckung eines Modellsystems mit starken spektroskopischen Signalen wird die weitere Untersuchung der Substrukturbildung in Graphen ermöglichen, und die verbesserte Methodik zur statistischen Analyse separater Strukturen in Graphen mit Hilfe der Raman-Spektroskopie bietet ein neues, leistungsfähiges Instrument für die künftige Forschung.

2 Introduction

2.1 Carbon and Its Allotropes

Carbon plays a special role in chemistry since approximately 95 % of all known chemical compounds today contain it.[1] This is due to its unique ability to form strong covalent bonds with itself and many other elements. Carbon is the sixth element of the periodic table and has a $1s^2 2s^2 2p^2$ electron configuration, where four outer electrons occupy the 2s and 2p orbitals (**Figure 1A**). To obtain a noble gas configuration carbon can therefore either receive or take four electrons by forming up to four covalent bonds. This versatility is also reflected in the number of carbon allotropes, different structural modifications of the same element. Carbon's ability to form covalent bonds in different hybridization states (sp, sp^2, sp^3) allows the formation of several allotropes with distinct properties. While graphite and diamond have been known to man since ancient times several new allotropes have been discovered since the 1980s and the realm of possibilities is not exhausted yet, making it a dynamic field of research.[2] In addition, the big breakthroughs over the past decades inspired many new fields in chemistry, physics and material science, especially the field of two-dimensional crystalline materials.[3]

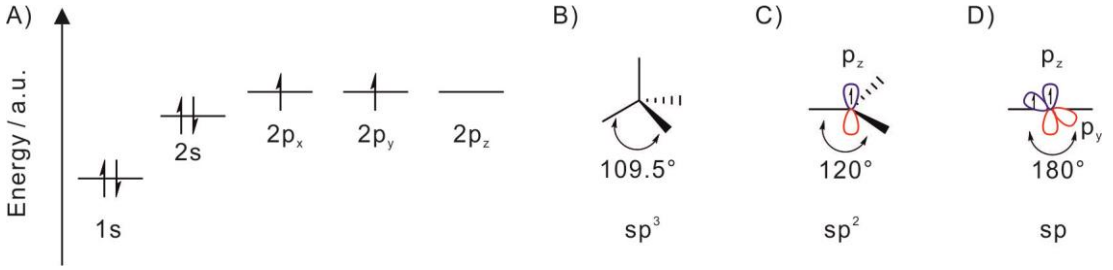

Figure 1: A) Electronic structure of carbon with four valence electrons. B) Carbon with sp^3-hybridization with a tetrahedral structure that can form four σ-bonds with neighboring carbon atoms. C) sp^2-hybridized carbon where three valence electrons can form σ-bonds and one electron in the $2p_z$-orbital can form a π-bond with neighboring carbons. D) Carbon with sp-hybridization, where two sp-hybridized orbitals can form σ-bonds with 180° bond angle and two unpaired electrons in 2p-orbitals can form two π-bonds with neighboring carbon atoms.

In diamond every carbon is sp^3-hybridized and forms four covalent σ-bonds with a bond angle of 109.5° to its neighboring carbon atoms with a bond length of 154 pm (**Figure 1B**).[4] This results in a face-centered cubic crystal lattice structure (**Figure 2A**), where the four strong bonds form a covalent three-dimensional network making diamond an extremely hard material and an electrical insulator (bandgap 5.5 eV).[5] It is typically grown at high temperatures and high pressures, where it becomes the most stable phase of carbon.[6] Recently Gong *et al.* reported the synthesis of diamonds in liquid metal alloy at ambient pressure where the meta-stable diamond crystallizes out of a saturated carbon solution.[7]

At ambient conditions graphite (**Figure 2B**) is the thermodynamically most stable carbon allotrope.[6] Here, each carbon atom is sp^2-hybridized and three of its electrons (2s, $2p_x$, $2p_y$) form three covalent σ-bonds with a bond angle of 120° (trigonal-planar) to its neighboring carbon atoms with a bond length of 142 pm resulting in a hexagonal two-dimensional graphene lattice. The remaining electron in the $2p_z$-orbital (**Figure 1C**) perpendicular to the plane of the

carbon lattice is delocalized across the graphene sheet and forms a conjugated π-system with its neighbors. Two sublattices form since there are two carbon atoms per unit cell, as shown in **Figure 2C**.[8] Because of the binding situation of carbon atoms graphite consists of many layers called graphene that are stacked on top of each other by weak van der Waals and π-π-interactions resulting in an approximate distance of 335 pm between the graphene sheets. It has a high electrical conductivity along the graphene sheets due to the delocalized π-system, but in orthogonal direction is much lower.[9] Graphene was the first example of a two-dimensional (2D) carbon allotrope and will be discussed in detail in section 2.2. Since its discovery, several other 2D carbon allotropes have been synthesized, for example covalently-linked fullerene sheets[10] or biphenylene networks.[11]

In 1985 the fullerenes were discovered as the first of a growing number of new carbon allotropes[12] and Robert F. Curl, Harold W. Kroto and Richard E. Smalley were awarded the Nobel Prize in chemistry in 1996 for their discovery. Fullerenes are a class of spherical or ellipsoidal molecules that can be denoted by the empirical formula C_n, where n is an even number. The prototypical C_{60} fullerene (**Figure 2D**) consists of 20 hexagons and 12 pentagons that result in a spheric shape due to the positive curvature induced by the pentagons. Due to the inherent strain fullerenes are quite reactive compared to the other sp^2-carbon allotropes and due to their excellent electron accepting properties they are used as electron transfer layers in organic photovoltaics.[13]

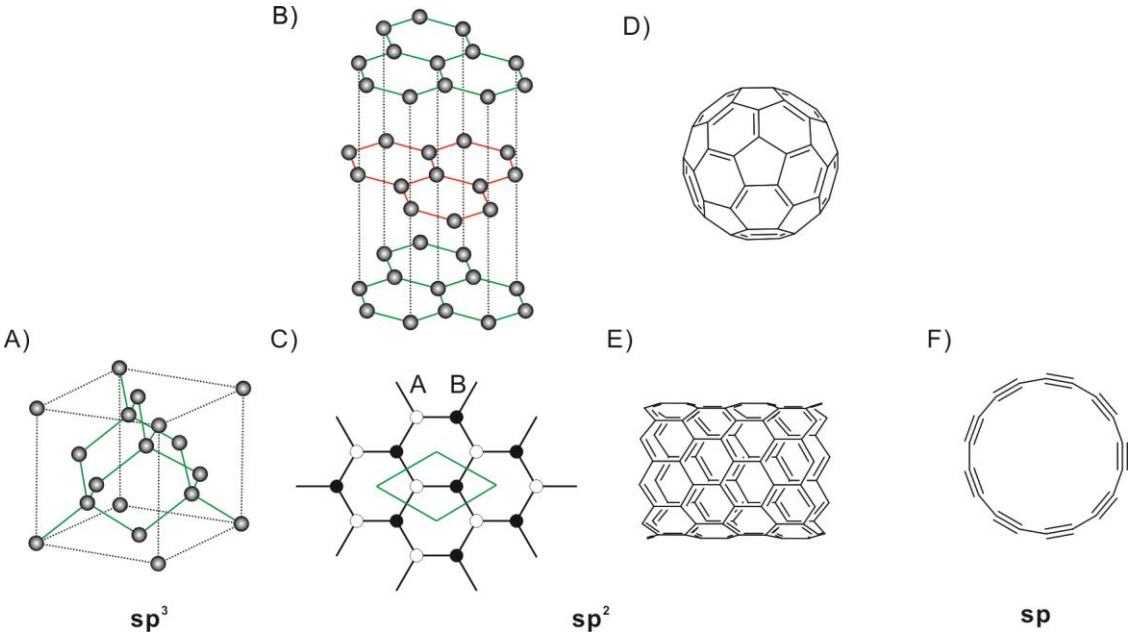

Figure 2: Overview of some carbon allotropes arranged by their hybridization. A) Diamond unit cell with face-centered cubic crystal structure, in which all carbons are sp^3-hybridizd and are bound to four other carbons. B) AB-stacked graphite with sp^2-hybridized carbon atoms. The double bonds have been omitted for clarity. C) Graphene with its two-atom unit cell (green) forming two sublattices A (white) and B (black). D) Fullerene C_{60}, a spherical molecule made of 20 hexagons and 12 pentagons with sp^2-hybridization. E) Carbon nanotube (9,0) with zigzag edges and metallic properties. F) Cyclo[18]carbon the first example of an all-sp-hybridized carbon allotrope.

In 1991 carbon nanotubes (CNTs, **Figure 2E**) were discovered by Iijima and Ichihashi[14] that have a hexagonal carbon lattice arranged in a cylindrical tube. Depending on the direction that

the lattice is oriented relative to the axis of the cylinder, their properties such as the diameter and edge structure vary and thus the electronic properties can be varied between semiconducting or metallic. These tunable properties make carbon nanotubes candidates for carbon-based electronics.[15] Recently Lin *et. al* demonstrated the fabrication of transistor devices from aligned carbon nanotube films that are comparable to state-of-the-art 10 nm-node silicon-based devices.[16]

Carbyne is a hypothetical carbon allotrope in which all carbons are sp-hybridized and thus have a linear geometry forming two σ-bonds with a 180° bond angle, while the two unhybridized 2p-orbitals form two π-bonds (**Figure 1D**).[17] Synthetically, polyynes with up to 48 carbon atoms have been synthesized, however the ends of the chains are terminated by sterically demanding end groups to stabilize the highly reactive molecule.[18] The first carbon allotrope in which carbon is exclusively sp-hybridized was synthesized by Kaiser *et al.* in 2019.[19] They synthesized a C_{18} ring (**Figure 2F**) by an on-surface atom manipulation method at cryogenic temperatures and due to the high reactivity of carbon triple bonds and the strain induced by the circular structure this novel class of carbon allotropes is only stable at such temperatures. These new ring structures offer new synthons for carbon material synthesis and their unique electron structures allow to test theories of aromaticity.[20]

Allotropes with mixed carbon hybridization states have been predicted to yield even more novel properties but are also more challenging to synthesize.[21]

2.2 Graphene

A single layer of graphite is called graphene and can not only be viewed as a two-dimensional crystal but also as a polycyclic hydrocarbon with enormous extent in the plane of the carbon lattice.[22] The properties of graphene and how they emerge can be understood by looking at the smallest aromatic carbon structure with a hexagonal lattice, the benzene molecule (**Figure 3A**). Each sp^2-carbon atom forms three σ-bonds and adds one electron, located in a $2p_z$-orbital, to the π-system, which is therefore half-filled. The six π-electrons occupy defined molecular orbitals resulting in three bonding π- and three anti-bonding π*-orbitals that are located below and above the Fermi energy (E_F), respectively (**Figure 3A**). Larger nanographenes (sizes between 1-100 nm) can be constructed by fusing benzene rings and thus increasing the delocalization of the π-electrons, which decreases the energy gap between the highest occupied molecular orbital (HOMO) and the lowest unoccupied molecular orbital (LUMO). Their synthesis becomes increasingly difficult due to the decreasing solubility in organic solvents.[23] The largest nanographene reported to date is the C_{222} nanographene with a size of around 3.2 nm, that could be solubilized by attaching 2,6-dimethyl-phenyl groups at the edges.[24] By extending the size only in one dimension graphene nanoribbons (GNRs) can be constructed.[25] Their properties are also dominated by edge effects.[26] Thus, GNRs with zigzag edges are metallic while other edge structures are semiconducting, and the size of the bandgap decreases with further extension of the ribbons.[26] Such edge and quantum confinement effects dominate the properties due to the relatively small size of the structures in at least one dimension.[27]

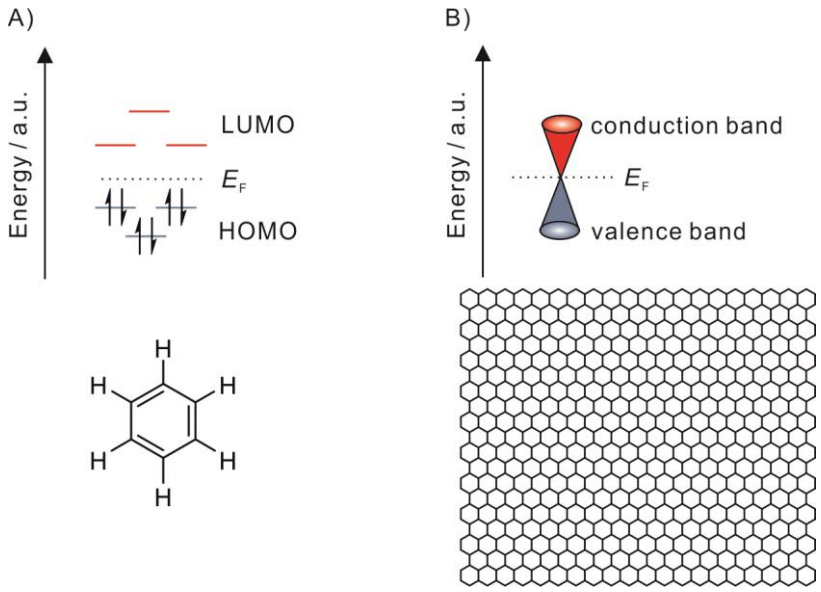

Figure 3: A) Geometric and electronic structure of benzene. The electrons occupy defined molecular orbitals below E_F and the LUMO is located above E_F. B) Structure of graphene (300 carbon atom cutout) constructed from fused benzene rings and electronic structure with cone-shaped valence and conduction that intersect at E_F.

At sizes larger than 100 nm the material can be considered as graphene[22] since the influence of the edges becomes insignificant due to the large surface-to-edge ratio that results in a large surface area of 2630 m^2g^{-1}.[28] Before its first successful fabrication in 2004 by Novoselov *et al.*[29] it was believed that two-dimensional crystals would not be thermodynamically stable above 0 K, as stated by the Mermin-Wagner theorem.[30] Later research found that intrinsic ripples stabilize graphene and explain its existence at ambient temperatures.[31] Andre Geim and Konstantin Novoselov were awarded the Nobel Prize in physics in 2010 for their discovery. The graphene lattice is defined by the two atom unit cell (**Figure 2B**) and therefore two bands are formed in its electronic structure.[32] Due to the large number of valence electrons and their extensive delocalization its orbitals form a valence and conduction band that intersect at the so called Dirac points, that have the shape of a cone in momentum space with a linear dispersion (**Figure 3B**) meaning that the electron´s energy increases proportionally with the change of momentum.[8] Graphene is therefore a bandgap-less semimetal and the electrons in graphene behave as massless Dirac fermions.[32] The linear dispersion allows the electrons to travel at high speeds with minimal scattering allowing exceptionally high charge carrier mobilities around $3 \cdot 10^6$ $cm^2V^{-1}s^{-1}$ in encapsulated graphene.[33] Together with its high thermal conductivity of 5500 WmK^{-1}[34] this makes graphene an ideal candidate for high performance electronic devices (see section 4.5).[35]

Stacking of graphene layers leads to the formation of Moiré superlattices that change the properties of the material, for example causing superconductivity at a tilting angle of 1.1° and at 1.7 K.[36] The superlattices also affect the reactivity of graphene.[37] The outstanding properties of graphene depend on the intactness of the graphene lattice and is strongly affected by defects, as discussed in the next section.

2.2.1 Defects in Graphene

Any deviation from the infinite hexagonal carbon lattice of graphene is considered a defect and there are several different types of defects. These defects alter the properties of graphene and controlling the kind and density of defects can create new properties beyond the pristine material.[38] The long-range order of the carbon lattice can be disturbed by edge structures (**Figure 4A** and **B**), [39] non-hexagonal ring structures e.g. in Stone-Wales defects (**Figure 4C**)[40] or line defects, single and multiple carbon vacancy defects forming holes inside graphene (**Figure 4E** and **G**),[41] and heteroatom substitution (**Figure 4D**).[42] Furthermore, the reaction of an in-plane carbon atom with another atom or molecule can result in covalent bond formation, converting the sp^2-carbon to a sp^3-carbon and hence disrupting the conjugated π-system (**Figure 4F**).[43]

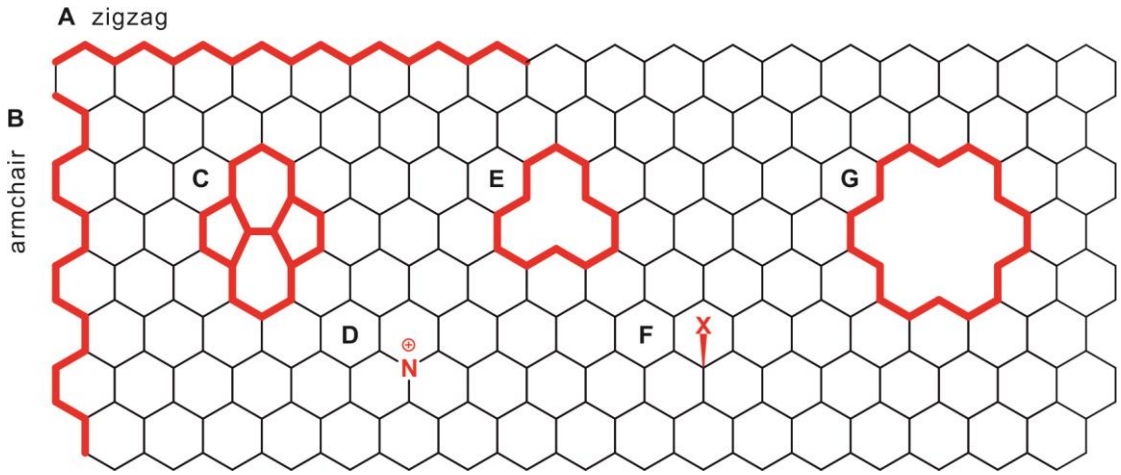

Figure 4: Examples of defects in graphene. A) Zigzag edge. B) Armchair edge. C) Non-hexagonal ring structures, e.g. Stone-Wales defect, where one carbon-carbon bond is rotated 90°. D) Heteroatom substitution, here by a nitrogen atom. E) Single carbon vacancy. F) sp^3-defect by covalent addition of addends (X, atoms or molecules) creating an out-of-plane C-X bond. G) Multiple carbon vacancies can lead to hole formation influencing the mechanical properties and permeability of graphene sheets. Holes can be up to several 100 nm.[44] Double bonds have been omitted for clarity.

In the simplest case edges terminate the carbon lattice and determine the electronic structure of GNRs, CNTs and nanographenes, as discussed earlier.[26] Due to its large surface-to-edge ratio, the edges of graphene generally play a minor role but influence the electronic structure at grain boundaries.[39] Armchair and zigzag edges (**Figure 4A** and **B**) can be distinguished and in real graphene crystals also disordered edges occur.[45] At edges and holes graphene is terminated by heteroatoms that allow selective functionalization.[46] All-carbon defects occur in the form of rearranged carbon atoms. They can form during crystal lattice formation and thus occur in natural graphite and graphene derived out of it.[47] In a Stone-Wales defect (**Figure 4C**) four hexagons are transformed into two heptagons and two pentagons by rotating one C-C bond by 90°. They show a low barrier for proton permeation and can thus cause an unexpectedly high proton permeability and isotope selectivity in graphene membranes.[48] When several carbon atoms are missing from the lattice holes (**Figure 4G**) can form that are big enough to strongly change the properties of graphene and e.g. allow the diffusion of small molecules through the otherwise impermeable graphene plane.[49] Such holes can be formed by

overoxidation during the synthesis of graphene oxide with excess oxidizer or by a thermal disproportionation reaction upon thermal reduction of graphene oxide.[50] The carbon atoms are lost as CO_2 and the resulting lattice defects will therefore remain after reduction of oxo-functional groups but can be restored by chemical vapor deposition.[51] Porous graphene with large holes up to several 100 nm in diameter can be synthesized from graphene with small vacancy defects.[44, 52]

While defects on the one hand alter the unique properties of pristine graphene, they extend on the other hand the range of achievable properties.[53] Especially the covalent functionalization of graphene that will be discussed in detail in the next chapter offers a plethora of new materials with distinct properties.[43] Vacancy and hole defects for example strongly increase the reactivity of the relatively inert graphene, by inducing strain on the neighboring carbon atoms. Therefore, structural defects are favored reaction sites even for highly reactive radicals and allow to functionalize such materials on the plane while greatly preserving the intact graphene lattice.[54]

2.2.2 Covalent Functionalization of Graphene

As discussed in the previous chapter, edges, and in-plane defects such as carbon vacancies or holes activate surrounding unsaturated carbon atoms, while carbon atoms within the hexagonal lattice are more stable. Here, we focus on the covalent functionalization of in-plane carbon atoms rather than edge or defect sites. Generally, sp^3-defects allow to fabricate covalent heterostructures out of the plane of the carbon lattice and to attach additional functionality e.g. for sensing applications.[55] Direct laser writing allows to create arbitrary shapes, while their resolution is limited by the spot size of the laser used.[56] The controlled addition of functional groups at the atomic scale remains limited to being largely guided by structural defects present in the graphene starting material or statistical addition to the graphene plane.

By reaction with other atoms or molecules the in-plane sp^2-carbon atoms of the graphene lattice can form new carbon-heteroatom bonds. Thus, new functional groups such as hydroxy or epoxy groups can be introduced and further be used for derivatization.[57] The carbon atoms become sp^3-hybridized and the bond angle decreases from 120° in the plane of the C-C bonds to 109.5° in a tetrahedral geometry.

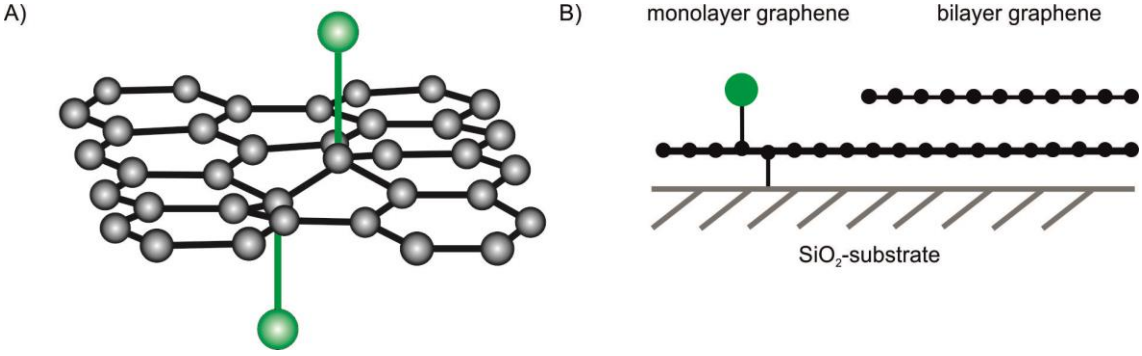

Figure 5: A) Structural model of bitopically 1,2-functionalized graphene by forming new C-X bonds (green). B) Reaction of substrate-supported graphene, releasing strain by addition reaction with the SiO_2-substrate.[58]

In the absence of defects or strain, approaches for covalent functionalization suffer from the low reactivity of the graphene lattice that makes functionalization challenging and typically requires preactivation or harsh reaction conditions such as high temperatures or highly reactive reactants.[43] Many different functionalization techniques have therefore been developed to form new in-plane carbon bonds to take advantage of the large accessible surface area. Among the most prominent are cycloaddition reactions and radical addition reactions.[43] In addition to the modification of graphene properties, functionalization allows to attach molecules to the large graphene plane, e.g. for sensor applications or drug delivery.[43] The low reactivity compared to fullerenes and carbon nanotubes can be explained by the lack of strain in the pristine graphene lattice, causing an increase of strain in the system upon functionalization that makes reactions unfavorable.[59] In other curved carbon systems, reactions release strain from the sp^2-system due to the smaller bond angle of sp^3-carbon atoms. Therefore, one strategy to increase the reactivity of graphene without introduction of structural defects is to introduce local curvature by deposition of graphene onto a surface covered with nanoparticles.[60]

The introduction of a sp^3-defect forms a reactive π-radical that can interact with either another reagent molecule or the substrate. By reaction with a carbon atom next to the first reaction site a 1,2-addition can saturate the reactive π-radical and release a part of the strain from the lattice if the addition happens from the opposite side (**Figure 5A**). Schäfer *et al.* have demonstrated the substrate-dependent functionalization of graphene, where SiO_2 surfaces, where carbon-oxygen bonds can be formed increased the reactivity towards the aryl radical reagent while no reaction occurred on bilayer graphene (**Figure 5B**).[58] Spatial control of functionalization on the microscopic scale can be achieved in various ways, e.g. by patterning approaches using a resist that is developed to leave arbitrary shapes on the surface exposed while the rest is covered by the resist and does not react at the applied conditions. By repeating this procedure graphene materials with defined patterns of various substituents can be fabricated.[61] Importantly, spatial control here is only achieved by deposition of the resist defining reactive and blocked graphene areas without any regioselectivity towards various areas of the graphene lattice.

2.2.3 Spatial Arrangement of Functional Groups

In addition to the introduction of sp^3-defects in the graphene lattice by covalent functionalization the spatial arrangement of the substituent substantially influences the properties of the graphene derivative.[62] In the absence of factors that guide the reactivity of graphene or the reaction partners, addition reactions should result in a statistical distribution of substituents, but the addition of a single radical breaks the symmetry of the graphene and affects subsequent addition reactions. Due to the two sublattices of graphene (**Figure 2C**) addition to the A lattice will cause the delocalization of the π-radical on the B lattice and *vice versa*, breaking the symmetry of the periodic lattice. The addition of a second radical is more likely on the B lattice and scanning tunnelling microscopy (STM) studies with hydrogen radicals have shown that the addition in the 1,2 and *cis*-1,4 adjacent to first addition sites are the most reactive sites (**Figure 6A**).[63] In addition, reaction in 1,2-position from either side of the graphene plane can

relieve some of the strain induced by the sp^3-defects (**Figure 5B**), making the 1,2-addition even more preferable when both sides of graphene are accessible for the reaction partner.[58] The addition of hydrogen therefore occurs in an island fashion (**Figure 6B**), leaving pristine graphene domains next to them. As these islands extend, they confine the sp^2-domains causing an increase of the fluorescence of hydrogenated graphene.[64]

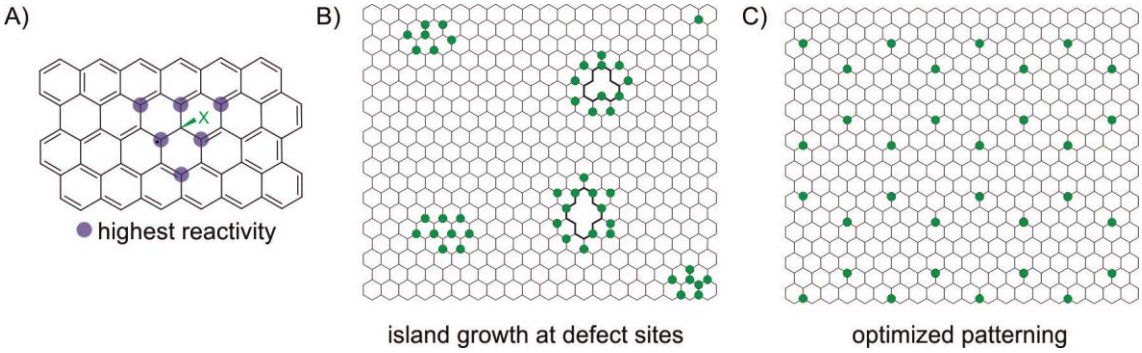

Figure 6: A) Visualization of symmetry-breaking by radical addition to graphene. The carbon atoms with the highest electron densities (highlighted in blue) are located around the first addition site (green). B) Island growth of functionalized areas due to preferred addition around defect sites. C) Optimized patterning maximizing the number of sp^2-substructures by disrupting the conjugated π-system (functionalization: 10.3 %).

The emerging confinement effects hint at the possibilities of graphene modification by controlling the spatial arrangement of functional groups with atomic precision. Gao *et al.* have shown using density functional theory (DFT) calculations that the bandgap of hydrogenated graphene can be tuned by controlling the number of nonmagnetic sp^2-substructures defined by the addition patterns between 0 and 5.4 eV (**Figure 6C**).[65] While the theory behind the spatial arrangement-dependent modification of graphene properties is well understood it remains challenging experimentally to achieve the needed regiochemical control on the atomic scale and new approaches are highly desired.[56] Established approaches include limiting the reaction to the desired area by photolithography, the periodic variation of the graphene reactivity by substrate interactions, or by using regioselective reagents. Similar to the widely used photolithography approach on the microscopic scale, sacrificial supramolecular assemblies can be used to confine the reaction to defined areas on the graphene that are not covered.[66] Tahara *et al.* used self-assembled monolayers of *n*-alkanes to achieve patterning of graphene with aryl groups in lines with a periodicity between 5 and 7 nm.[67] The reactivity of graphene can be modulated by the underlying substrate, e.g. by Moiré superlattice formation with single crystal metal substrates or defined substrates allowing selective functionalization defined by the superlattice.[68] Zhou *et al.* used spherical silicon dioxide nanoparticles as the substrate to define superlattices that can be tuned by using nanospheres of various size.[69] Superlattices allow to tune the size and shape of the pattern by varying the angle between graphene and the substrate. Order can also emerge by controlling the spatial arrangement of the reagent prior to the reaction. For this, the reagent must be sterically demanding to overcome the preferred addition in the most reactive positions. Yu *et al.* demonstrated a spatially selective photocycloaddition reaction by using a maleimide derivative that formed a defined supramolecular network on top of the graphene plane.[70] These approaches allow spatially

controlled addition to graphene, however they require highly controlled reaction conditions that limit their large-scale applicability. Furthermore, the lack of spectroscopic signals of the formed substructures impedes their characterization.

2.3 *Trans*-Polyacetylene

Polyacetylene is a polymeric chain of sp^2-carbon atoms, where every carbon atom is bonded to two neighboring carbons and one hydrogen atom. It is not an allotrope of carbon due to its bonds to hydrogen, but it can be classified as a carbon-rich compound that is a quasi-one-dimensional chain of sp^2-carbon atoms. It was studied extensively as a simple model system for many phenomena of solid-state physics in the one-dimensional system and the transition from molecular to band structures.[71] Two isomeric structures exist in which all double bonds are oriented either in *cis*- or *trans*-orientation (**Figure 7A** and **B**), and the *cis*-isomer can be thermally converted to the more stable *trans*-isomer.[72] The electronic properties of these chains depend on the carbon-carbon bond lengths. Peierls distortion results in a two-atom unit cell with reduced symmetry that lowers the symmetry and therefore breaks the degeneracy of orbitals by electron-phonon coupling.[73]

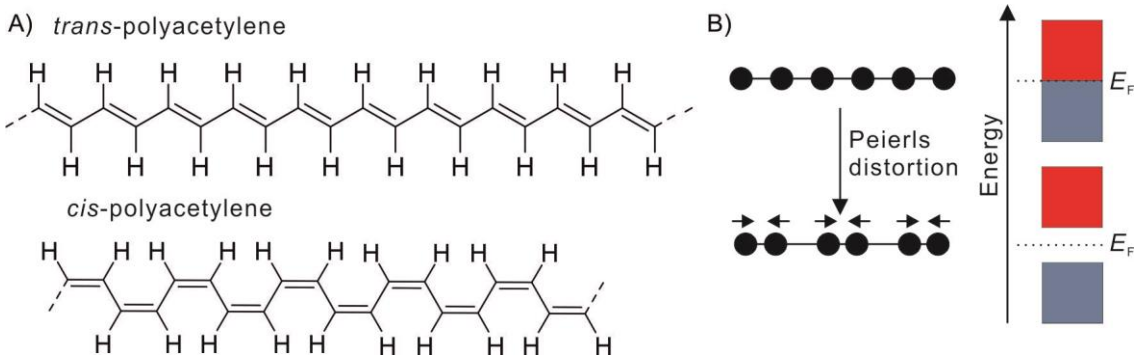

Figure 7: A) Chemical structure of *trans*- and *cis*-polyacetylene. The chains can be regarded as a single row taken from a graphene zigzag and armchair edge respectively. Importantly, every carbon atom is connected to a hydrogen atom. B) Schematic illustration of the Peierls distortion. Electron-phonon coupling causes doubling of the unit cell and bandgap formation in one-dimensional metals.

This stabilizes the HOMO while the LUMO is destabilized forming a bandgap (**Figure 7B**). The size of the bandgap depends on the chain length due to the varying conjugation lengths. *Trans*-oligoene molecules with defined chain lengths have been synthesized to study the influence of conjugation length on the electronic properties of conjugated chains and confirmed the chain length-dependent bandgap through characterization of their properties using Raman spectroscopy (see section 4.1.1).[74] Above 12 double bonds the molecules were too insoluble for analysis similar to nanographenes discussed earlier. Interest in *trans*-polyacetylene polymers increased steeply after the discovery that iodine-doped *trans*-polyacetylene became metallic, with conductivity increased by seven orders of magnitude.[75] For their discovery and for contributions to the development of conductive polymers, Alan J. Heeger, Alan G. MacDiarmid and Hideki Shirakawa were awarded the Nobel Prize in chemistry in 2000. At high doping levels Peierls distortion is suppressed and *trans*-polyacetylene becomes a zero-bandgap metal. However, there is still a debate whether the strong increase of the conductivity is really

caused by a semiconductor-to-metal transition in bulk *trans*-polyacetylene.[76] It likely consists of a mixture of chains with finite lengths and strong doping could increase their conductivity by facilitating electron transfer between those chains as evidenced by the strong increase of conductivity in polymers with non-conjugated carbon chains.[77] Wang *et al.* studied individual *trans*-polyacetylene chains synthesized on a copper(110) surface at atomic resolution.[78] They visualized the bond alternation and confirmed the induced bandgap (2.4 eV) for electronically decoupled *trans*-polyacetylene. They also observed the semiconductor-to-metal transition through strong n-doping of the copper surface.

The characteristic Raman signals of *trans*-polyacetylene (see section 4.1.1) have also been observed in nanocrystalline diamonds indicating their presence as sp^2-substructures within grain boundaries of the sp^3-carbon material.[79]

2.4 Iodine and Graphene

Iodine is the largest of the non-radioactive halogens and its properties are therefore dominated by its large size and number of electrons as well as its low electronegativity compared to the other halogens. It has 53 electrons with $[Kr]5s^25p^5$ configuration meaning that only one electron is needed to fulfil the octet rule. The electrostatic potential of dihalogen molecules is anisotropic, so that electron density accumulates in a belt around the axis of the molecule and an area of low electron density forms on the opposite side of the σ-bond, the so called σ-hole (**Figure 8A**). The large electron number makes the σ-hole most pronounced in iodine (F < Cl < Br < I).[80] It therefore acts as an amphiphile and interacts with nucleophiles in a 180° angle along the bond axis where a large partial positive charge (δ^+, blue) is located, while the partial negative charge (δ^-, red) perpendicular to the covalent bond allows interaction with electrophiles in a 90° angle to the iodine-iodine bond axis (**Figure 8A**).

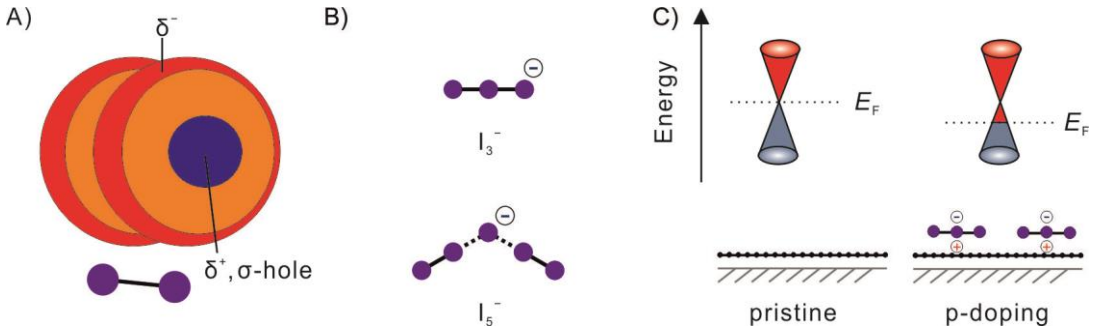

Figure 8: A) Schematic illustration of the electrostatic potential around the iodine molecule with low electron density opposite the σ-bond (blue) and high electron density around the axis of the molecule (red). B) I_3^- and I_5^- as examples of polyiodides that form by the interaction of an iodide with σ-holes of the iodine. C) Charge-transfer complex formation with graphene by electron transfer from graphene to iodine causes polyiodide formation and p-doping of graphene. **Figure 8A** was redrawn based on the reference.[80]

Iodine forms polyiodides of which the triiodide I_3^- is the prototypical example (**Figure 8B**), that is formed by reaction of iodine with an iodide nucleophile. Larger polyiodides form by addition of more I_2 molecules and their exact shape and bond angles depends on the counter cation (**Figure 8B**).[81] The formation of polyiodides is a Lewis acid-base reaction, in which the Lewis

base iodide or polyiodide donates electron density from their HOMO into the LUMO of the Lewis acid iodine.[80]

Due to its electronegativity iodine can p-dope carbon allotropes and carbon-rich materials. As described in the previous chapter, the addition of iodine to *trans*-polyacetylene polymer films increased the conductivity of the material by seven orders of magnitude and caused a semiconductor-to-metal transition.[75] Iodine forms charge-transfer complexes with graphene, where one electron is transferred from graphene to iodine forming polyiodides (**Figure 8C**). This non-covalent functionalization causes the removal of charge carriers leading to an increase of the hole conductivity and thus p-doping.[82] The formation of polyiodide networks on graphene however have mostly been studied theoretically leaving their properties, such as the extent of polyiodide network on top of graphene experimentally unexplored.

The photochemistry of the halogens is characterized by the homolytic cleavage of the halogen-halogen bond and halogen radical formation.[83] Similarly, polyiodides are photochemically cleaved by visible light yielding iodine radicals (**Equation 1**).[84]

$$\mathbf{I_3^-} \xrightarrow{h\nu} [\mathbf{I_3^-}]^* \rightarrow \mathbf{I_2^{-\cdot}} + \mathbf{I^\cdot} \qquad (\mathbf{1})$$

Due to its large electron density, iodine can stabilize the unpaired electron relatively well compared to bromine, chlorine, or fluorine making it the least reactive.[83] A large interest in the photochemistry of polyiodides has grown since their use in dye-sensitized solar cells in which iodide oxidation is used to convert solar energy into chemical energy in the form of covalent iodine-iodine bonds.[85]

Many reaction schemes using halogen radical addition reactions are used to covalently functionalize graphene.[86] Especially the highly reactive chlorine radicals have been studied extensively, showing reversible covalent modification reactions and strong p-doping.[87] A discrepancy between the degree of functionalization as observed by X-ray photoelectron spectroscopy (see section 4.4) and by Raman spectroscopy (see section 4.1.2) was observed for chlorination and azidation reactions[88] while additional reversible Raman signals were observed that were assigned to zone folding and symmetry lowering due to the strong p-doping effect.[89] These phenomena indicate the incomplete understanding of the addition reactions of halogens to graphene. The reaction of graphene and iodine has been studied significantly less, and mostly defective graphene was used that made the analysis of the reaction products more difficult.[90] Thus none of the above-mentioned phenomena were observed in iodinated graphene. Li *et al.* electrochemically generated chlorine, bromine and iodine radicals and found no reaction of iodine with high-quality graphene and observed the formation of elemental iodine instead.[91] To overcome the low reactivity of iodine the photochemical reaction of polyiodide-doped graphene was used in this work to generate iodine radicals directly at the graphene surface that resulted in new Raman signals with large intensities that allowed to study the phenomena observed in chlorinated graphene in unprecedented detail.[92]

3 Preparation of Graphene

Several routes to synthesize graphene have been developed that yield graphene with varying sizes and qualities.[93] Bottom-up syntheses such as the synthesis of nanographenes and GNRs from aromatic precursor molecules yield molecules or polymers with defined structures but they are limited by the diminishing solubility of large aromatic molecules.[22] Chemical vapor deposition where graphene is assembled atom by atom on a catalytically active metal surface on the other hand is extremely successful in the synthesis of large-area graphene sheets.[94]
Top-down approaches generally use graphite as the starting material and yield graphene monolayers either by applying mechanical forces to overcome the interaction between the graphene sheets or by functionalization followed by exfoliation in a suitable solvent.[95] Graphite is readily available in large quantities and the quality of the graphene can be adjusted by the choice of the starting material and the method used.[96] While mechanical exfoliation generally yields graphene with high quality the wet-chemical synthesis route yields graphene with more structural defects but in large quantities. In the following the methods that were used in this thesis are described.

3.1 Mechanical Exfoliation

The first method that was applied to fabricate monolayer graphene was tape-assisted micromechanical exfoliation commonly referred to as “scotch-tape method”.[29] The relatively weak van der Waals forces between the graphene sheets in the graphite are overcome by applying mechanical shear force parallel ($F_{\parallel}$) and normal force perpendicular ($F_{\perp}$) to the graphene plane via the tape separating intact monolayer flakes from the bulk material (**Figure 9A**). The forces must be controlled carefully to avoid breaking of the bulk crystal and to ensure that graphene adheres strongly to the substrate so that the interlayer interactions within the bulk crystal can be overcome.[97]

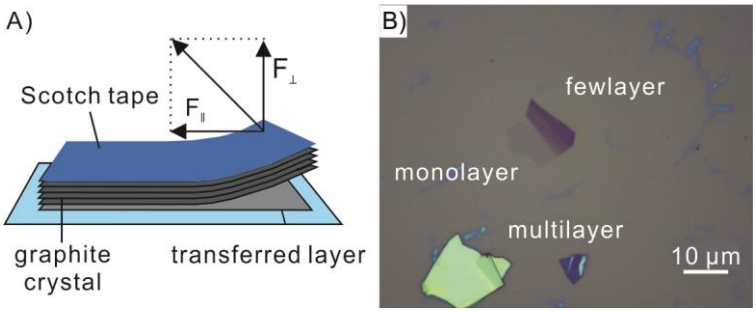

Figure 9: A) Schematic illustration of the tape-exfoliation process. A tape (blue) is attached onto the bulk graphite crystal that is pressed onto a suitable substrate and a single graphene layer is transferred by exerting normal ($F_{\perp}$) and shear forces ($F_{\parallel}$) onto the graphene layers to overcome the van der Waals interactions between the graphene layers. B) Optical microscopy image of tape-exfoliated graphene flakes at 100x magnification. Mono-, few- and multilayer graphene was transferred. **Figure 9A** was redrawn based on the reference.[98]

Single layers of 2D materials can be obtained by attaching adhesive tape to the bulk graphite crystal and subsequent removal of the tape.[98] The thin crystals removed from the bulk are repeatedly treated the same way until thin flakes remain that can be transferred from the tape onto arbitrary surfaces. Optical microscopy can then be used to identify monolayers, especially on Si wafers coated with a SiO_2 layer that strongly enhances the contrast (**Figure 9B**).[99]

High quality graphite with low defect densities and large crystalline domains are necessary to yield graphene with a high quality and to avoid fragmentation of the bulk crystal upon applying mechanical stress. Advanced methods have been developed to facilitate the separation of single layer crystals, for example gold-assisted exfoliation where millimeter-sized monolayers of 2D materials are exfoliated either by pressing of the bulk crystal onto a freshly prepared gold surface and subsequent removal of the tape[100] or direct evaporation of thin metal films on the bulk crystal.[101] Generally, mechanical exfoliation can be applied to all van der Waals crystals making the method very versatile for research, especially on heterostructures of 2D materials.[102] However, the yield of this method remains low and the method is time consuming limiting its applications to the preparation of high-quality and large area samples for academic research.

3.2 Wet-Chemical Synthesis of Graphene from Oxo-Graphene

Another top-down approach is the chemical conversion of graphite into graphite oxide in which the graphene layers are functionalized with oxygen-containing (oxo) groups that can be delaminated to monolayer graphene oxide and subsequently graphene by reduction of the oxo-groups.[103] The oxidation of graphite using strong oxidizers to functionalize graphene allows to quantitatively convert graphene to few-layered graphene derivatives (**Figure 10A**).[104]

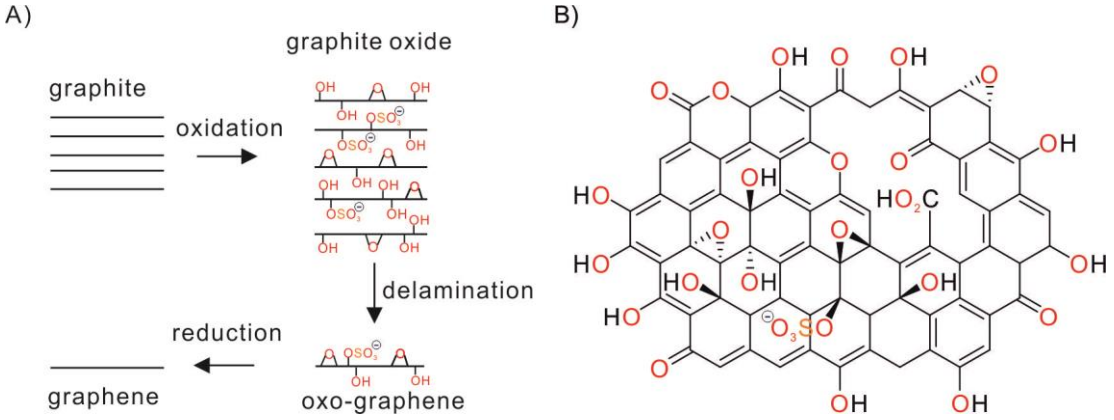

Figure 10: Illustration of the wet-chemical synthesis of graphene. A) Schematic illustration of the graphene oxide synthesis. Graphite is oxidized in a strong concentrated acid (e.g. sulfuric acid) by addition of a strong oxidizer (e.g. permanganate) forming graphite oxide after workup that contains oxo-groups on both sides of the graphene plane and a strongly increased interlayer spacing. Increased interlayer spacing and solubility from functional groups facilitate delamination to graphene oxide and subsequent reduction of functional groups yields graphene. B) Proposed structure of oxo-G with oxygen-containing functional groups on both sides of the carbon lattice.

The synthesis is a two-step process that starts with the formation of an acceptor-type graphite intercalation compound (GIC), where an electron is transferred from graphite to the strong oxidizer and subsequently H_2SO_4/HSO_4^- can intercalate into the galleries of the graphite

crystal.[105] This process was first described by Schafhaeutl in 1840.[106] Rüdorff and Hofmann found an idealized stoichiometric formula of $(C_{24}^{+}HSO_4^{-} \times 2\ H_2SO_4)_n$ and that the degree of oxidation cannot be increased further by addition of more oxidizer.[107] The interlayer distance between the graphene sheets is extended from 335 pm to 798 pm. In the second step the oxidizer and sulfuric acid functionalize the GIC. The oxidation of graphite via such a GIC was first described by Brodie by heating graphite in a mixture of concentrated nitric acid and potassium chlorate for several days.[108] Many syntheses have been developed since then that all have in common that graphite dispersions in a strong acid such as sulfuric acid or nitric acid react with an oxidizer such as permanganate, persulfate, nitrate or chlorate.[109] Most methods used today are based on the method introduced by Hummers and Offeman using permanganate as the oxidizer in concentrated sulfuric acid.[110] Aqueous workup of such reaction mixtures then yields graphite oxide, where oxygen containing functional groups are attached to the edges and in-plane carbon atoms of the graphene sheets and the interlayer distance is strongly increased up to 1160 pm in aqueous solutions due to the swelling caused by the intercalation of the solvent.[111] The increased dispersibility in suitable solvents and the reduced van der Waals forces between the layers facilitate the delamination to graphene oxide.[112] Graphene oxide typically contains many defects due to overoxidation that leads to lattice defect formation by oxidation of carbon atoms to CO/CO_2. The gaseous reaction products escape from the reaction mixture leaving an irreversibly damaged graphene lattice.[50a] To improve the quality of the final product it is imperative to reduce the amount of overoxidation that results in carbon loss and hole formation. Therefore, keeping the temperature below 10 °C was found to be necessary throughout the complete synthesis to yield graphene oxide with an intact carbon lattice that was subsequently termed oxo-functionalized graphene (oxo-G) to emphasize the intact carbon lattice.[113] Generally, all methods can yield high quality graphene if the reaction conditions are controlled.[114] Oxo-G is a non-stoichiometric compound and the exact composition strongly depends on the synthetic method used but is mainly composed of epoxide, hydroxy and organosulfate groups and the degree of functionalization is typically around 50 % (**Figure 10B**).[109] Carbonyl, carboxylates and lactol groups terminate the edges and holes. The delaminated monolayers are separated from few- and multilayers by centrifugation according to their hydrodynamic radius. Centrifugation allows to separate graphene oxide sheets according to their dimensions.[115] Reduction of the oxo-groups finally yields graphene films and can be performed either directly in solution using surfactants to stabilize the graphene or as thin films on a substrate. Thermal reduction is a convenient method to remove oxo-goups but yields relatively low-quality graphene due to the introduction of defects. A disproportionation process leads to the extension of large holes by oxidation to CO/CO_2 and the reduction of in-plane carbon atoms yielding intact graphene domains next to large holes.[50b, 116] Chemical reduction offers the advantage to remove functional groups without thermally induced overoxidation reactions. Reduction of substrate-supported oxo-G with hot vapors of hydroiodic acid and trifluoroacetic acid was found to quantitatively reduce oxo-groups without the introduction of additional lattice defects.[117]

3.3 Chemical Vapor Deposition

While the previously described methods fabricated graphene monolayers from bulk graphite starting material, chemical vapor deposition (CVD) builds monolayer graphene on metal substrates atom by atom in a bottom-up process. This approach can be applied to a wide array of other 2D materials such as hexagonal boron nitride (hBN), transition metal dichalcogenides and metal oxides and thus is a general scheme for 2D material synthesis.[94] Due to the scalability of the process and the high quality of graphene it is also a good candidate for large-scale production.[118] The size of the monolayer films is only limited by the area of the metal substrate used and therefore allows the large-scale production of monolayer graphene.[118]

Graphene growth has been reported on many metals and alloys, but copper foils have been used extensively due to their commercial availability and convenient graphene growth conditions.[119] The process was first described by Li *et al.* using the decomposition of methane gas on copper surfaces at high temperatures slightly below the melting point of copper (~1000 °C) at a low pressure and the reaction mechanism is displayed in **Figure 11**.[120] Due to the low solubility of carbon in copper the process follows a surface self-limiting mechanism yielding monolayer graphene.[121]

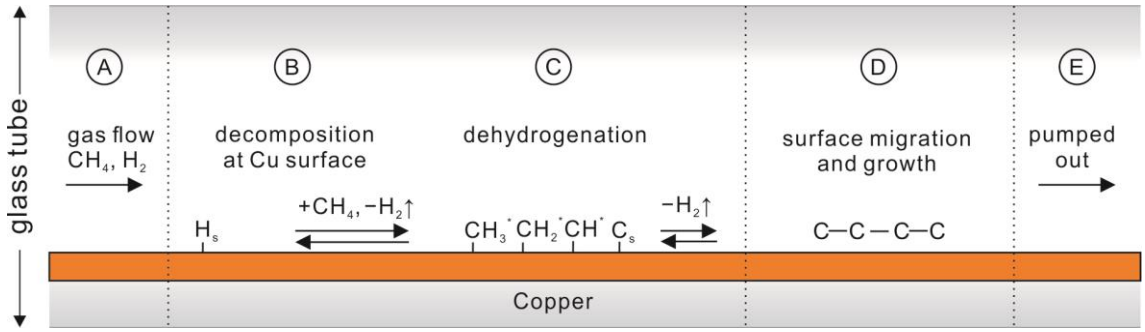

Figure 11: Schematic depiction of the graphene growth mechanism on copper foil. Methane decomposes and carbon radicals adsorb on the copper surface. The carbon radicals migrate on the surface to active sites and graphene grows. Hydrogen adsorbed onto the copper surface facilitates methane decomposition and controls the growth and morphology of graphene.

The carbon-containing precursor gas (typically methane) is mixed with hydrogen gas and flowed over the catalytically active metal surface at high temperatures and low pressure (**Figure 11A**) causing the decomposition of the reactant and the adsorption of reactive methane radicals at the metal surface.[122] Hydrogen plays multiple important roles during the growth process: Hydrogen decomposes more easily at the copper surface compared to methane by forming adsorbed hydrogen (H_s) that facilitates the subsequent decomposition of methane (**Figure 11B**). The methane radicals are further dehydrogenated leaving carbon atoms chemisorbed at the metal surface (**Figure 11C**). The adsorbed carbon atoms and methane radicals can migrate and begin to grow into larger carbon clusters, which turn into defective graphene before reorganizing into defect-free graphene at sufficiently high temperatures (**Figure 11D**).[123] Hydrogen reacts with carbon side products and oxidative contaminants so that they can be pumped out (**Figure 11E**). The hydrogen ratio thus controls the morphology and size of the graphene domains since it etches away adsorbed carbon species. By using a large hydrogen/methane ratio the growth of bilayers can be favored.[124] The growth process strongly depends on the

process temperature either favoring kinetic growth of carbon clusters at lower temperatures or thermodynamically favored high-quality graphene. Prior to the growth phase, the copper foil must be annealed in a hydrogen atmosphere to remove any copper oxides from the surface and to cover the surface with reactive adsorbed hydrogen species (H_s).[125] Additional pre-treatment with etchant can also be used to remove oxide layers and to achieve smooth and monocrystalline domains. Jin *et al.* reported a contact-free annealing method that converts commercially available polycrystalline copper foil into monocrystalline foil that allows to grow single crystalline graphene films.[126] While the main focus of research is on the large-scale synthesis of defect-free graphene this insight allows to tune the properties of the graphene further and use CVD graphene with defined defect densities for studies on defect-related phenomena.[92b] Furthermore, the process allows to tune the graphene properties by adding additional gaseous precursors to the reaction mixture, such as ammonia for nitrogen-doped graphene[127] or bromine.[128]

Many techniques have been developed to transfer graphene grown on copper onto arbitrary substrates. Among the most widely used are wet-transfers, where typically, a protective layer of a polymer such as polymethyl methacrylate (PMMA) is applied onto graphene that increases its mechanical stability and then the graphene is transferred onto a water surface by etching away the copper[129] or electrochemically by evolution of hydrogen gas between substrate and graphene.[130] After deposition onto a suitable substrate the PMMA can be removed yielding pristine graphene.[131]

4 Characterization Methods

4.1 Raman Spectroscopy

The inelastic scattering of light was first observed experimentally by Chandrasekhara Venkata Raman in 1928[132], who was awarded the Nobel Prize in physics in 1930 for this discovery that is named *Raman scattering* after him. Today, Raman spectroscopy is a central tool for the study of carbon-rich compounds due to the plethora of information that can be gained from it.[133] **Figure 12A** shows the fundamental principle where a photon hits a sample (molecule or crystal) and most of photons are scattered elastically (same energy before and after scattering, Rayleigh scattering) but a small number of photons will be inelastically scattered and their energy is reduced (Stokes) or increased (Anti-Stokes) by the energy of molecular or lattice vibration vibrational excitations.

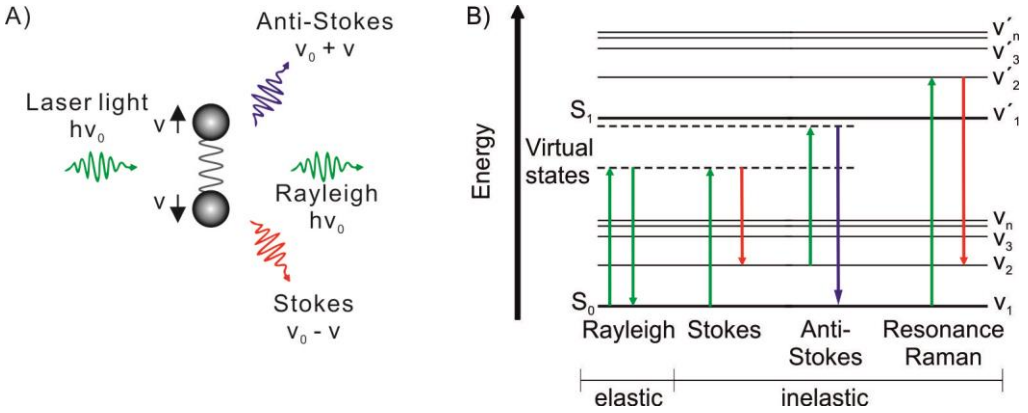

Figure 12: A) Schematic illustration of the Raman effect. Light is scattered at a molecule and a small portion of energy is exchanged causing the emission of light with a higher (Anti-Stokes) or lower (Stokes) energy than the incident laser light. B) Jablonski diagram illustrating the scattering processes.

The change of the photon energy is relatively small (~ meV) compared to the incident photon energy (eV) and therefore excitation with defined energies and a precise detection are necessary. The energy is typically reported as "Raman shift" in wavenumbers (cm^{-1}), which is the energy difference between the incident laser light (defined as zero Raman shift) and the detected Raman light. In general, Raman scattering is not a resonant phenomenon (**Figure 12B**) and therefore the scattering happens by the transition of an electron from the electronic ground state (S_0) to a virtual state. If the electron is excited to a real electronic state (S_1) the Raman cross section is greatly enhanced but is also in competition with fluorescence (**Figure 12B**).[134]

Inelastic scattering is induced by a change of the polarizability (α) that describes the induced dipole moment $p_{induced}$ by an external electric field $E_{external}$. It describes the extent to which the external field drives the electron density of the molecule out of its equilibrium compared to the state without the presence of an external electrical field (**Equation 2**). The size of the polarizability is influenced by vibrations of the molecule/solid.

$$\boldsymbol{p}_{\mathbf{induced}} = \boldsymbol{\alpha}\, \boldsymbol{E}_{\mathbf{external}} \quad (2)$$

The selection rule for the Raman process is that the polarizability must change as the molecule vibrates and thus not all vibrations are Raman-active depending on their symmetry and there is the rule of mutual exclusion stating that any Raman-active vibration is not IR-active and *vice versa*.[135] Therefore, Raman spectroscopy is uniquely suited to probe allotropes that have no dipole moments due to lack of dipole moments in the ensemble.

4.1.1 Raman Spectroscopy of *Trans*-Polyacetylene

One-dimensional systems are often studied due to their simple structure as a model system to understand spectroscopic features in systems with more dimensions. Similarly, the Raman spectroscopy of *trans*-polyacetylene has enabled a deeper understanding of conjugated carbon systems[136] and can also guide our understanding of 2D systems such as graphene.[137]
Trans-Polyacetylene has a C_{2h} symmetry and thus it has two Raman- ($4a_g$, b_g) and two IR-active (a_u, $2b_u$) vibrational states that can be probed and due to the chain length-dependent bandgap these Raman-active modes are strongly enhanced by the resonance Raman effect.[138] The Raman spectra of *tert*-butyl-capped *trans*-oligoene molecules (**Figure 13A**) with defined numbers of double bonds show three modes (v_1, v_2, v_3) that demonstrate the decreasing Raman shift, especially of the v_3-mode, with increasing number of double bonds (**Figure 13B**).

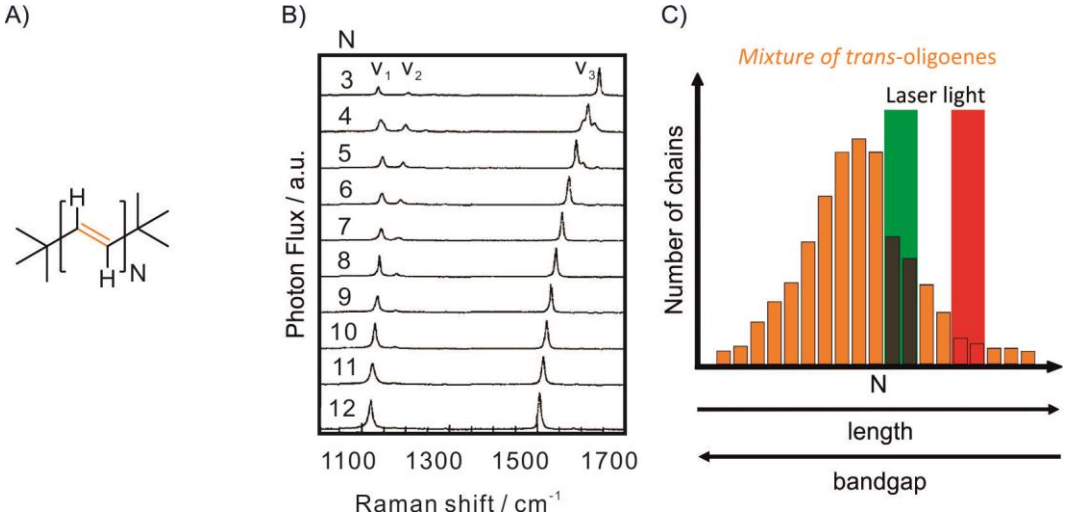

Figure 13: A) Molecular structure of the molecules synthesized by Schaffer *et al.* with a defined number of double bonds (N, orange) and *tert*-butyl end groups. B) Raman spectra of *trans*-oligoene molecules with N = 3-12. C) Schematic illustration of probing a mixture of *trans*-oligoenes with finite length according to their length-dependent bandgap. Depending on the wavelength of the laser light used a small subset of the mixture is probed. **Figure 13B** was reproduced from the reference[139] with permission from the Journal of Chemical Physics, Copyright 2024, license number 5774131174839. **Figure 13C** was redrawn based on the reference.[92a]

Due to the length-dependent bandgap of *trans*-oligoenes with well-defined lengths can be clearly distinguished by the position of their Raman signals.[139] The changing properties should converge for the infinitely long polymer *trans*-polyacetylene and Raman spectroscopy can thus be used to probe these properties. However, since the system is quasi-one-dimensional any

defect such as a sp^3-defect will effectively terminate the conjugation since there is no "way around" the defect.[140] *Trans*-polyacetylene can thus be modelled as a material with an unknown distribution of *trans*-oligoene chains that are separated by defects. Due to the resonance Raman conditions a small subset of chains can be probed with a given laser wavelength which must match the bandgap (**Figure 13C**).[141] Schen *et al.* studied *trans*-polyacetylene samples with defined molecular weights and found a distribution of chain lengths in the polymer material using resonant Raman spectroscopy.[142] Theoretical calculations on the DFT level are also in good agreement with the observed properties.[143] Due to this property, Raman spectroscopy can be used to analyze finite elements in bulk *trans*-polyacetylene by probing samples at various wavelengths and monitoring the shift of the Raman modes as well as their intensities.

4.1.2 Raman Spectroscopy of Graphene

Raman spectroscopy can be used to study many properties of graphene such as the number of graphene layers in few-layer graphene, number of defects, doping, covalent functionalization, or mechanical strain.[144] Since graphene has no bandgap any excitation within a broad range of wavelengths will lead to absorption of photons and therefore a resonance Raman effect.[145]
The Raman-active modes of graphene can be rationalized by considering the symmetry and electronic structure of graphene. It has a D_{6h} symmetry with two atoms in its unit cell and is therefore composed of two sublattices with a hexagonal lattice structure (**Figure 2C**). In the reciprocal space the hexagonal lattice can be constructed from the two momentum vectors k_x and k_y that form the first Brillouin zone (**Figure 14A**). At the corners of the Brillouin zone are the K and K' points called the Dirac points where the valence and conduction band intersect. The fundamental selection rule states that the phonon wave vector $q_{phonon} \approx 0$, so that momentum is conserved upon energy transfer.[146]

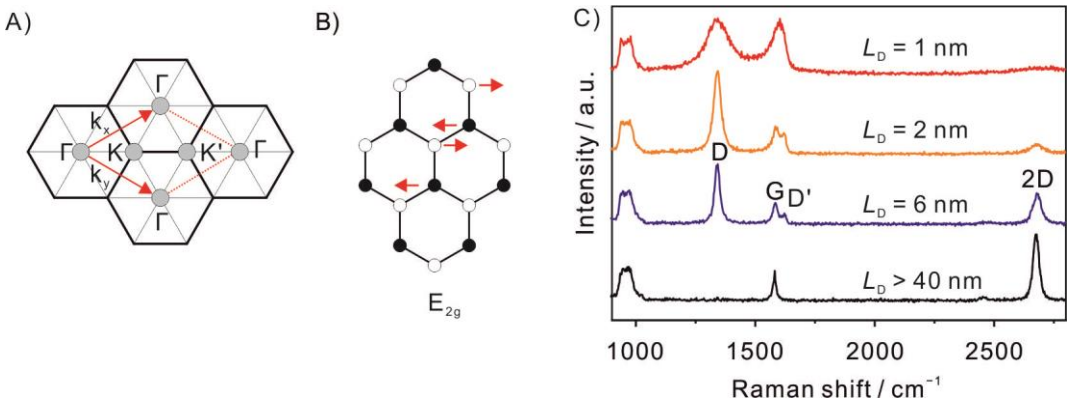

Figure 14: A) Illustration of the first Brillouin zone of graphene in the reciprocal space. B) Schematic illustration of the Raman-active E_{2g} phonon responsible for the G-mode. C) Evolution of Raman spectra from pristine graphene (black) to defective graphene (red) with their corresponding average defect distances.

The double degenerated E_{2g} phonon fulfils the criterium for first-order Raman scattering, is termed the G-mode (**Figure 14B**) and appears at around 1580 cm^{-1}. The Raman spectrum of pristine graphene (**Figure 14C**, black spectrum) shows a second mode at around 2650 cm^{-1} (at 532 nm excitation wavelength), that is due to second order Raman scattering, where two

phonons with opposite momentum are excited at the same time and is called the 2D mode. While the D is derived from the word “defect” the 2D-mode is also present in the absence of defects due to the double resonant process.[147] The D-mode requires an in-plane transversal optical phonon and a defect for its activation and can thus be used to analyze defects in graphene. The D-mode emerges at around 1340 cm^{-1} (at 532 nm excitation wavelength) when defects such as vacancies or sp^3-defects are introduced since the ring breathing phonon (**Figure 15A**) is a second order process. The D'-mode at around 1620 cm^{-1} originates from a double resonant process by an intravalley process between K and K'. Comparison between the D- and D'-mode intensities can be used to distinguish between sp^3- and vacancy defects.[148] Importantly, while the defect-induced graphene modes are observed upon introduction of arbitrary functional groups, no new Raman signals originating from the new groups are observed. Therefore, statistical Raman spectroscopy allows to compare material properties across 2D samples to extract statistical values and is not constrained to a certain kind of defects.[149] In combination with a microscopy setup, samples can be mapped and spatially resolved spectroscopic information can be obtained, making it especially suited for the investigation of 2D materials.[45] However, not all defects in graphene are Raman-active. Zigzag edges, doping and strain in the graphene lattice for example do not contribute to the Raman D-mode.[144] Due to symmetry reasons zigzag edges cannot transfer momentum and thus do not satisfy the conditions for momentum conservation. Consequently, they do not contribute to D-mode formation.[150]

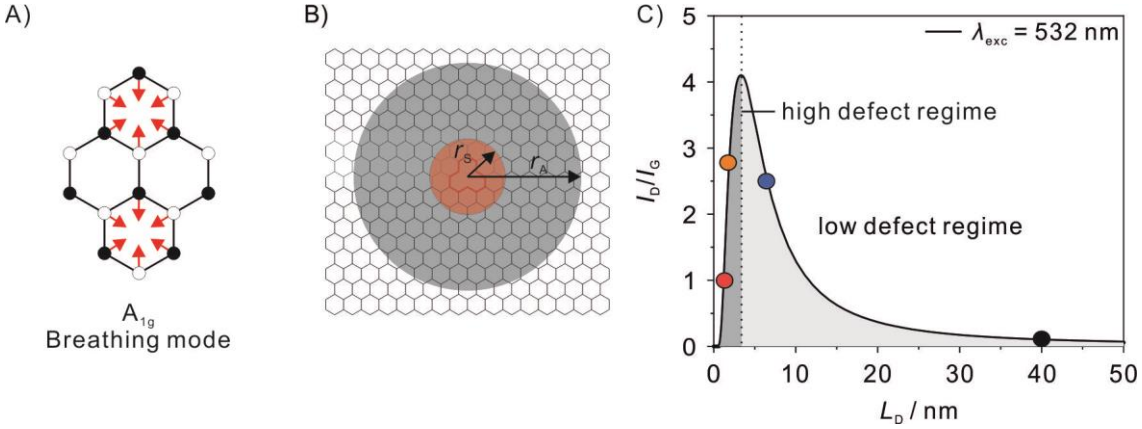

Figure 15: A) Ring breathing phonon (A_{1g}) causing the D-mode. B) Definition of structurally disordered area (r_S) and activated area (r_A) around a defect site. C) Plot of I_D/I_G versus the defect distance L_D as calculated by **Equation 3**. The colored dots are the corresponding values of the spectra shown in **Figure 14C**.

To quantify defects in graphene a thorough understanding of graphene structure and the respective changes of the Raman spectrum are necessary. Tuinstra and Koenig empirically found that the I_D/I_G ratio is inversely proportional to the average crystallite size of the graphite (L_α), as described by **Equation 3**.[151] Here, $C(\lambda)$ is a wavelength-dependent parameter that describes the maximum I_D/I_G ratio that can be obtained.

$$\frac{I_D}{I_G} = \frac{C(\lambda)}{L_\alpha} \quad (3)$$

This equation however is only valid at low defect densities and is therefore of little use to describe a wide range of graphene materials. A more general description of the Raman spectra of graphene with defects was found empirically by Lucchese and Cançado (**Equation 4**):[152] They used Ar^+ sputtering to introduce defined defect densities into graphene and follow the change of the Raman spectra with respect to the average distance between defects (L_D). Here, the I_D/I_G ratio is described again by a factor C_A that is wavelength-dependent and represents the maximum of the I_D/I_G ratio in graphene. Two circular areas around a point-defect are defined that are given by the "structurally-disordered" area disrupted by the defect (r_S) and the activated area (r_A) around it in which a phonon formed can diffuse to the defect and induce a D-mode (**Figure 15B**). The values of radii that characterize the circular areas r_A and r_S were determined to be 3 and 1 nm respectively (corresponding to ~958 and ~120 carbon atoms respectively).

$$\frac{I_D}{I_G} = C_A \frac{\left(r_A^2 - r_S^2\right)}{\left(r_A^2 - 2r_S^2\right)} \left[e^{-\frac{\pi r_S^2}{L_D^2}} - e^{-\frac{\pi\left(r_A^2 - r_S^2\right)}{L_D^2}} \right] \quad (4)$$

As more defects are introduced first r_A starts to overlap and cover more areas of the pristine graphene. Adding more defects decreases *the* activated area by overlapping of structurally-disordered domains that do not cause a D-mode due to their lack of intact lattice domains. The resulting curve rises with the introduction of defects and reaches a maximum at a defect distance around 3 nm and decreases steeply at smaller defect distances (**Figure 15C**). Below L_D values of 1 nm the I_D/I_G ratio does not decrease anymore and is therefore not a good parameter to measure defect densities above 1 %.

At defect densities above 1 % **Equation 4** is not a good tool to follow changes in graphene anymore. Instead, Vecera *et al.* proposed the integrated area of the D- or G-mode.[153] The area of these modes increases due photoluminescence (PL) induced by the confinement of sp^2 domains (**Figure 6B**) and the PL-intensity increases exponentially. Using reference samples with known degree of functionalization the samples can be measured across the full range of defect densities.

4.2 Atomic Force Microscopy

Raster probe microscopy techniques are widely used because of their high spatial resolution, which is independent of the diffraction limit. It was developed by Gerd Binnig and Heinrich Rohrer in 1981 and they were awarded the Nobel Prize in physics in 1986 for their discovery (shared with Ernst Ruska).[154] Atomic force microscopy (AFM) was developed from STM and first reported by Binnig, Quate and Gerber in 1986.[155] Since no electromagnetic radiation is involved in the process, the spatial resolution is not limited by the diffraction limit, and sub-atomic resolution can be achieved if well-defined one atom thick tips are used.[156] An additional key advantage of AFM is that contrary to STM the sample does not need to be conductive and thus arbitrary samples can be imaged.[157]

In a typical AFM setup, a sharp tip is mounted on a cantilever and is brought in close contact with the sample surface. An area is scanned in x and y direction by moving the sample

underneath the tip using the scanner stage (**Figure 16A**). A signal is detected by the changes of the deflection of a laser beam on the back of the cantilever due to the tip-surface interaction and resulting forces (**Figure 16A**). Three main driving modes are used that differ in the way how the tip interacts with the sample.[158] In contact mode the tip is brought into physical contact with the sample, and it follows the topography of the sample upon scanning. In the constant force mode, the force that the tip in contact with the sample exerts is held constant by regulating the height of the cantilever and the change of the voltage used is detected. With this method the sample and the cantilever can be easily damaged but it can also be used to clean surfaces by wiping adsorbents off the sample surface.[159] The sample can also be scanned in a constant height mode, where the height is held constant and changing force exerted by changing topography is measured. Sufficiently smooth surfaces are necessary to prevent the tip from crashing into a surface structure larger than the constant height that the tip is set to.

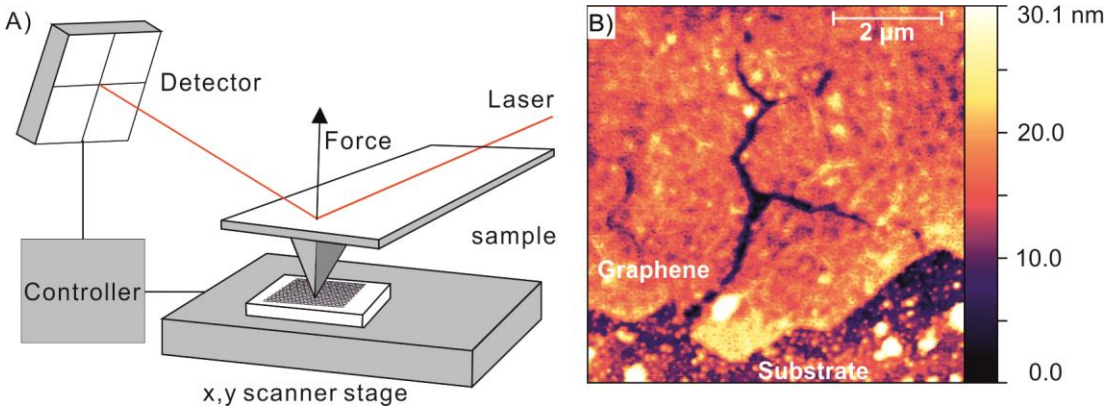

Figure 16: A) Schematic illustration of the AFM setup. A tip attached to a cantilever is used to scan the topography of the sample. Changes induced by forces acting on the cantilever are measured by the deflection of a laser beam on the back side of the cantilever. B) Topography image of iodinated CVD graphene on SiO_2/Si substrate. **Figure 16A** was redrawn based on the reference.[160]

In the non-contact mode, the cantilever oscillates at a frequency close to its resonance frequency while close to the sample surface and upon scanning the surface, long-range forces such as electrostatic forces change the oscillation frequency. The distance of the oscillating tip is then regulated so that the initial oscillation frequency is kept and the changes necessary are detected. The third driving mode, the intermittent mode, is used to combine both techniques discussed before. While the cantilever is oscillating, the distance is held between contact and non-contact mode so that the oscillation frequency is influenced by forces such as van der Waals forces, electrostatic forces, and dipole-dipole interactions.[160] AFM can thus provide detailed topographic information on samples, such as layer numbers of 2D materials by measuring the step heights at the edge of a material, adsorbed species and visualization of heterostructures (**Figure 16B**).[161] In addition, it can deliver additional information such as mechanical, electrochemical and optical properties of the sample.[160]

4.3 Kelvin Probe Force Microscopy

Kelvin probe force microscopy (KPFM) is a non-contact AFM method that measures the contact potential difference (CPD) between the measuring tip of the AFM experiment and the sample

while simultaneously measuring the topography of the sample. It was first reported by Nonnenmacher *et al.* in 1991[162] and is named after Lord Kelvin who first described the concept of contact potential differences in 1898.[163] A CPD occurs when two dissimilar semiconducting materials are brought into contact causing an equilibration of their Fermi energies by transfer of electrons from the material with the lower work function to the material with a higher work function. The work function (Φ) is the minimum energy required to remove an electron from its electronic ground state to the vacuum level (E_{vac}) and is an intrinsic property of a material (**Figure 17A**). The tip and the sample will generally have a different Φ and their level will therefore equilibrate by electron transfer from the material with a lower Φ to the other material. This buildup of opposite charges creates the CPD and can be measured by a potential difference V_{CPD}.

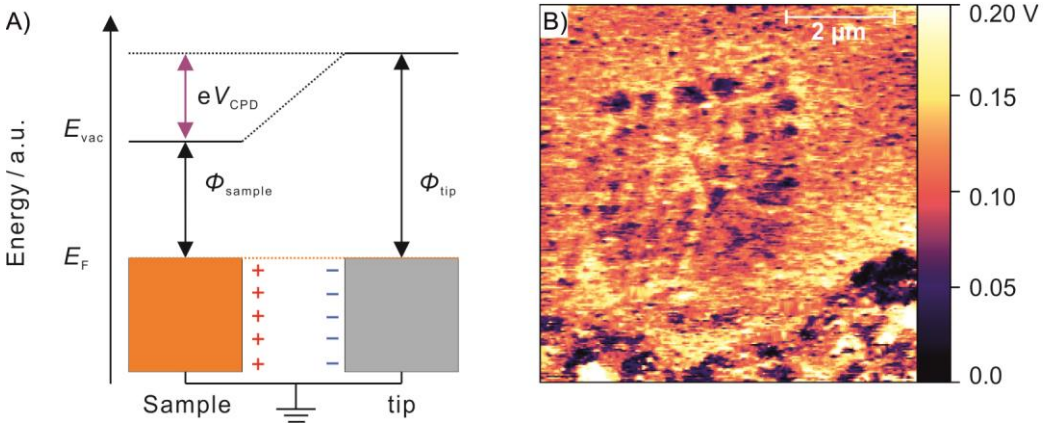

Figure 17: A) Illustration of the KPFM working principle. The tip and sample are brought into electrical contact causing equilibration of E_F and consequently charge buildup that can be measured by applying a potential. B) KPFM image of the sample shown in **Figure 16B**. The pattern visible due to the reaction of graphene with iodine is not visible in the topography image.

By applying an external field the charge can be nullified and detected. If the work function of the tip (Φ_{tip}) is known the unknown work function of the sample (Φ_{sample}) can be calculated using **Equation 5** where e is the elementary charge and V_{CPD} is the potential that is measured between the two materials.[164]

$$\boldsymbol{\Phi_{sample} = \Phi_{tip} - eV_{CPD}} \qquad \textbf{(5)}$$

Importantly, the sample must be electrically connected to the setup to ensure that $E_{F,\,sample} = E_{F,\,tip}$ otherwise the measured voltage is not identical to the work function difference. Thus, in addition to the topography image of the AFM measurement by using a conductive tip with a known work function, the local work function at every point can be extracted (**Figure 17B**). The change of the work function within a material can be used to extract a Fermi energy shift, that is caused by the changing material properties such as functionalization or doping.[55, 165] For graphene KPFM can be used to visualize addition patterns,[166] Moiré superlattices[167] and interlayer modulations in van der Waals heterostructures.[168] It is therefore a powerful tool to map material properties with high spatial resolution not limited by the diffraction limit.

4.4 X-ray Photoelectron Spectroscopy

X-ray photoelectron spectroscopy (XPS) can be used to assess the elemental composition as well as the bonding and oxidation states of the elements in a material.[169] The technique is based on the photoelectric effect, that was discovered by Heinrich Hertz in 1887[170] and its quantum mechanical origin was accurately explained by Albert Einstein in 1905, for which he was awarded the Nobel Prize in Physics in 1921.[171] Electrons are emitted from a material by irradiation with X-rays and the electrons emitted in this process are commonly called photoelectrons. XPS measurements must be carried out under ultra-high vacuum conditions since X-rays are attenuated by residual gas molecules and to avoid scattering of the photoelectrons with gas molecules (~70 nm mean free path at ambient pressure).[172] The small mean free path of the photoelectrons in the sample limits the escape depth to 1-10 nm and thus XPS is a surface-sensitive technique despite the penetration depth of X-rays in the µm range.[173] The ionization process is depicted in **Figure 18A** for a carbon atom, where a C 1s core electron is emitted upon irradiation with X-rays. After the expulsion of the core electron the system can relax by filling the core shell with an electron from the outer shell and the energy difference is emitted as light (X-ray fluorescence). Alternatively, the energy can be transferred onto a second electron with lower binding energy that leaves the system, a so-called Auger electron.[174] Auger emission is more likely for the lighter elements including carbon, while X-ray fluorescence is dominant for heavier elements.[175] Every core electron has a binding energy (E_B) that is defined as the minimum energy required to remove an electron from a sample (**Figure 18B**). To eject an electron the energy of the photon (hν) must be larger than E_B and the work function of the sample (Φ_{sample}) must be exceeded to remove the electron from the sample. The additional energy of the photon is converted to kinetic energy (E_{kin}) depending on the energy of the incident photon, according to **Equation 6**.

$$E_B = h\nu - E_{kin} - \Phi_{sample} \quad (6)$$

The emitted electrons can be analyzed by an electron analyzer that measures the effective kinetic energy ($E_{kin, eff}$) that is $E_{kin}+\Phi_{sample}$. Importantly, the sample must be electrically contacted with the analyzer so that E_F levels are similar and charging effects can be avoided.[176] By subtracting $\Phi_{analyzer}$, however there remains a discrepancy since typically $\Phi_{sample} \neq \Phi_{analyzer}$ (**Figure 18B**). XPS also yields information on the chemical state such as the oxidation state or bond order. A binding energy shift is observed when the electron distribution around an atom changes and can thus be detected as a change of E_{kin}. Two kinds of spectra are typically distinguished: Survey and elemental spectra with high resolution.

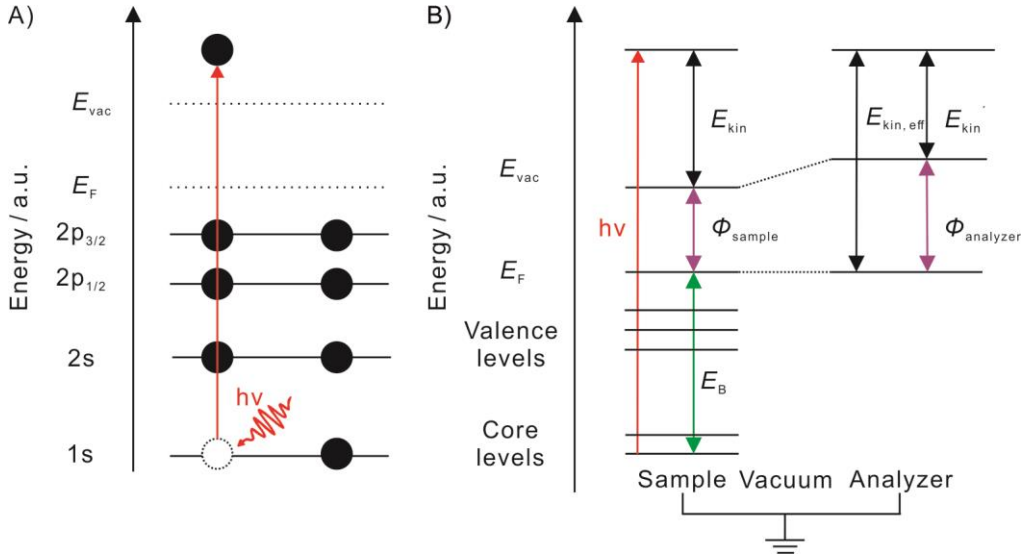

Figure 18: A) Schematic illustration of the photoelectron emission process. B) Energy level diagram illustrating the binding energy calculation from the measured kinetic energies. The sample and analyzer must be in electrical contact to ensure same Fermi energies and to avoid sample charging effects.

Survey spectra are collected by scanning across a large range of kinetic energies and can be used to identify the elements present in a sample. In addition, elemental information can also be quantified since the peak area is proportional to the quantity of each element present in the probed sample volume.[173] The relative intensity of the signals also depends on the X-ray cross section of each orbital that is expressed by relative sensitivity factors (RSF) to account for these variations and scale the observed intensities to derive atomic concentrations. The atomic fraction X of an element A in a mixture of elements j can thus be determined using **Equation 7**.[177]

$$\boldsymbol{X}(\mathbf{at\%}) = \frac{\frac{\boldsymbol{I}_\mathbf{A}}{\mathbf{RSF}_\mathbf{A}}}{\sum_j \frac{\boldsymbol{I}_\mathbf{j}}{\mathbf{RSF}_\mathbf{j}}} \qquad (7)$$

Scofield derived RSF values from theoretical calculations using a relativistic Hartree-Slater model to describe the atomic behavior.[178] Here, the RSF value of the C 1s orbital is defined as 1.0 whereas the RSF of the I $3d_{5/2}$ for example is 19.87 meaning that at similar atomic fractions the area of the C 1s peak is 19.87 times the size of the I $3d_{5/2}$ peak. To extract chemical information from elemental spectra high resolution spectra that only scan a small range are necessary. By deconvolution of the elemental peaks various components, for example from various hybridization states can be detected and quantified.[179] The background spectrum represents a significant portion of the elemental peak area and must be subtracted. It originates from various side effects such as photoelectrons generated by Bremsstrahlung, Compton scattering, satellite features and scattering of emitted photoelectron. Typically, this is achieved using a Shirley-background correction that empirically removes the background.[180]

4.5 Graphene-based Field-Effect Transistors

Field-effect transistors (FETs) are central in modern technology to achieve energy-efficient and fast switching of electronic signals.[181] They are therefore omnipresent in current electronic devices and since their first development the quest was to decrease the device dimensions since power consumption and switching speed increase exponentially with it.[182] 2D materials offer advantages such as reduction of leakage currents due to the electron confinement in atomically thin channels compared to thin films of bulk materials that have dangling bonds at their surfaces.[183] Graphene is well suited for the fabrication of FETs due to the high charge carrier mobility up to $3 \cdot 10^6$ $cm^2V^{-1}s^{-1}$ achieved by hBN-encapsulated samples[33] surpassing silicon by about three orders of magnitude. Its high thermal conductivity could deliver superior heat dissipation, a bottle neck in the current silicon-based devices.[184] The lack of a bandgap however causes small on/off ratios and graphene-based FETs cannot be completely turned off at ambient temperatures.[185] The initial work on graphene by Novoselov *et al.* was motivated by atomically thin metal layers to demonstrate unprecedentedly high charge carrier densities.[29] The basic structure of a back-gated graphene FET is shown in **Figure 19A**. It is a three-terminal device made from a semiconducting channel (here graphene) that bridges a drain and a source electrode. The current flow between the drain and source electrode through the channel can be modulated via a gate voltage V_g that is applied to a highly conductive silicon substrate that is separated from the channel by an insulating (e.g. silicon dioxide) dielectric layer. It is applied perpendicular to the channel and changes graphene's Fermi level and thus the number of charge carriers such that either no current can flow (off-state) or the flow of current is enhanced (on-state).

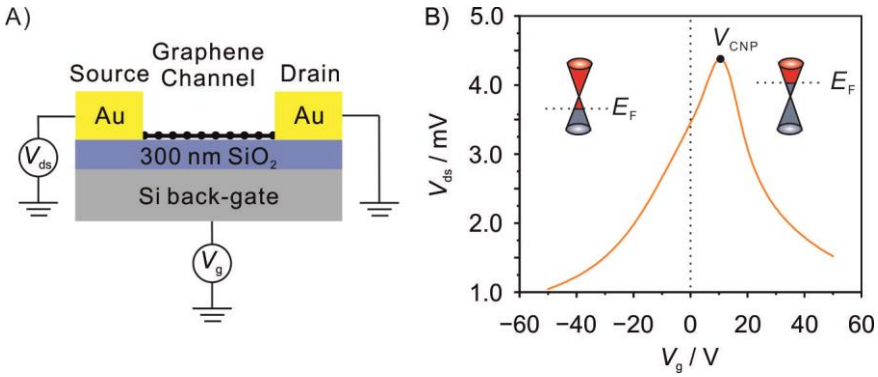

Figure 19: A) Schematic illustration of a graphene back-gate field-effect transistor device. A drain and source electrode are bridged by a semiconducting channel that is separated from a third gate electrode by an insulating dielectric layer. Application of a gate voltage changes the Fermi level of the semiconducting channel and thus the number of charge carriers. B) Plot of V_{ds} against V_g of pristine tape-exfoliated graphene showing p-doping as apparent from the V_{CNP} shift from zero to positive values.

The electronic properties of the graphene channel can be visualized by plotting V_{ds} against V_g (**Figure 19B**). Starting from negative V_g the V_{ds} increases until it reaches a maximum, the charge neutrality point V_{CNP} where the valence band is filled and the charge carrier density is thus zero, resulting in a minimum conductivity. In a perfect graphene sample V_{CNP} would be at 0 V, but doping by adsorbed molecules can change the doping level and thus shift the curve.

The charge carrier density n can be calculated from such a measurement using **Equation 8** where C_{tot} is the total areal capacitance and e is the elementary charge.

$$\boldsymbol{n = C_{tot}\frac{(V_g - V_{CNP})}{e}} \quad (8)$$

The total area gate capacitance describes the ability of the system to store electric charges and is given by **Equation 9**. It consists of the classical geometric areal capacitance C_{geo} and the quantum areal capacitance C_{quant}.[186] Geometric capacitance depends on the dielectric material and dimensions of the device (A_G). The dielectric constant of the silicon dioxide layer is ε_{SiO2} = 3.9 Fm^{-1}, ε_0 is the vacuum permittivity, and d_{SiO2} is the thickness of the silicon dioxide layer.

$$\boldsymbol{C_{tot} = C_{geo} + C_{quant} = A_G\left(\frac{\varepsilon_{SiO2}\varepsilon_0}{d_{SiO2}} + \left((2e^2)(\hbar v_F)^{-1}\sqrt{\frac{n}{\pi}}\right)\right)} \quad (9)$$

C_{quant} describes the effect of the density of states (DOS) near the Fermi energy E_F on the ability of the system to store electric charges. While a part of the applied voltage creates charge carriers in the graphene channel, another part changes E_F and therefore also the DOS reducing the number of charge carriers that is induced at the same voltage.[187] Here, e is the elementary charge, ħ is the reduced Planck's constant, v_F is the Fermi velocity near the K/K' point (~10^6 m s^{-1}). Near the Dirac point the DOS is small and therefore C_{quant} plays a significant role while for large V_g values the DOS becomes high as E_F is lowered or increased.[188] The transport curve of graphene shown in **Figure 19B** is p-doped by the SiO_2 substrate, adsorbed moisture as well as impurities trapped between graphene and the substrate and V_{CNP} is therefore shifted to a larger V_g (~15 V).[189] This sensitivity of graphene-based FETs towards adsorbed molecules allows sensing of gases that adsorb to the large surface area of graphene.[190] The gate voltage is limited by the breakdown of SiO_2 dielectric at field strengths of < 0.3 V/nm.[191] To overcome this limitation, ionic gating can be used to create electric fields over an order of magnitude stronger than dielectrics can withstand.[192] The commercialization of graphene-based transistors will also depend on their compatibility with established methods of fabrication for silicon-based electronics. Recently, graphene grown on silicon carbide was demonstrated to have a bandgap of 0.6 eV due to covalent bonding with the substrate in a defined pattern. It retains a high charge carrier mobility of up to 5500 cm^{2}V^{-1}s^{-1} which is ten times higher than the mobility of silicon.[193]

5 Synopsis of Results

5.1 Evidence for *Trans*-Oligoene Chain Formation in Graphene Induced by Iodine

F. Grote, B.I. Weintrub, M. Kreßler, Q. Cao, C.E. Halbig, P. Kusch, K.I. Bolotin, S. Eigler; Evidence for *Trans*-Oligoene Chain Formation in Graphene Induced by Iodine *Small* **2024**, e2311987.	6.1

The covalent addition of atoms or molecules to graphene is crucial to tailor its properties to introduce e.g. a bandgap or new functionalities. Raman spectroscopy is the central technique to follow such reactions since the formation of the characteristic D-mode at ~1340 cm^{-1} allows quantitative analysis of addition reactions. Halogenation reactions are among the best studied addition reactions. In contrast to the lighter halogens, the reaction of high-quality graphene with iodine was not reported, which was explained by the low reactivity of iodine.

In this work, derivatization of high-quality graphene with iodine was achieved for the first time by photochemical reaction of polyiodide-doped graphene. Surprisingly, additional Raman modes were observed at around 1130 and 1500 cm^{-1} with unprecedented intensity exceeding the characteristic Raman signals of graphene, while no D-mode formation was observed. The Raman modes resembled the characteristic signals of *trans*-polyacetylene (1125 and 1514 cm^{-1}) in which carbon atoms are linked by alternating single and double bonds indicating the formation of substructures within the graphene lattice upon reaction with iodine.

To rationalize the observed reactivity and to investigate the properties of this novel material the iodination of high-quality graphene was studied in detail. Impurities from the fabrication process or side reactions e.g. with the substrate (silicon dioxide, hexagonal boron nitride, gold) were experimentally excluded, leaving the reaction of iodine with graphene as the only source of the observed Raman signals. Resonance Raman measurements with different laser excitation wavelengths (532, 633, 638 nm) demonstrated the dispersive behavior of the new Raman modes as expected for *trans*-oligoene chains with a length-dependent bandgap. In addition, the complete conversion of graphene in some areas, as indicated by the disappearance of the characteristic graphene Raman signals around 1580 and 2650 cm^{-1}, proved the strong interaction of iodine with the graphene lattice. At higher laser energies (405 nm) defunctionalization occurred, leading to a change in Raman signal intensities at lower excitation energies. The reaction is thermally reversible at 400 °C as expected for sp^3-defects demonstrating that the Raman signals must originate from a thermodynamically stable structure.

The strong change of graphene properties was further demonstrated by transport measurements (in collaboration with Prof. Kirill I. Bolotin, FU Berlin). The iodinated graphene showed strong p-doping (5.8×10^{12} holes cm^{-2}, corresponding to a ΔE_F = 173 meV compared to the pristine graphene) of the iodination reaction, which exceeded the non-covalent doping by polyiodides (3.2×10^{12} holes cm^{-2}). Iodinated graphene showed superior stability under high-

vacuum conditions. The strong p-doping effect was also confirmed by KPFM measurements (in collaboration with Dr. Patryk Kusch, FU Berlin), which showed a difference in work function between pristine and functionalized regions, confirming the value extracted from transport measurements (ΔE_F = 141.5 meV). XPS measurements of iodinated graphene revealed a low carbon-iodine ratio of about one iodine per 300 carbon atoms that was close to the detection limit of the instrument.

Based on these observations and previous observations of hydrogen radical addition to graphene by STM, a reaction mechanism was proposed. The large size of the iodine radical was identified as the critical factor for the regioselective addition by blocking the most reactive positions (1,2 and *cis*-1,4) of the π-radical guiding the second addition. Thus, *trans*-oligoene substructures form within the graphene lattice due to the isolation of double bonds between sp^3-defects located along the delocalization path. An unknown distribution of *trans*-oligoene substructures forms that explains the dispersion of the Raman signals.

This work presents a first demonstration of the unique reactivity of iodine and graphene and provides evidence for regioselective addition of iodine in the complete absence of defects or patterns guiding the reactivity. The reaction mechanism presented will serve as a starting point for further research and may also provide an explanation for anomalies observed for chlorination and azidation reactions in earlier studies. It demonstrates the importance of addend size and shape in achieving regioselective addition reactions to graphene and may therefore open up new avenues for regioselective addition reactions and patterning at the atomic scale.

5.2 Influence of Lattice Defects on *Trans*-Oligoene Substructure Formation in Graphene

F. Grote and S. Eigler; Influence of Lattice Defects on *Trans*-Oligoene Substructure Formation in Graphene *Chem. Eur. J.* **2024**, e2024010331.	6.2

The initial research on the photochemical reaction of graphene with iodine revealed the fundamental mechanism of *trans*-oligoene substructure formation but did not consider the influence of lattice defects. Previous reports of iodination reactions of highly-defective graphene however did not report similar Raman signals at around 1130 and 1500 cm^{-1} indicating a hinderance of substructure formation. This was surprising since defects increase the reactivity of graphene by activating adjacent double bonds. Therefore, the aim of this work was to elucidate the influence of lattice defects on the *trans*-oligoene substructure formation induced by iodine.

Using graphene with defined defect densities, it was shown that the characteristic *trans*-oligoene signals at around 1130 and 1500 cm^{-1} can be induced in the presence of lattice defects albeit at lower intensities. Statistical Raman spectroscopy of the graphene D-mode in the most Raman-sensitive defect regime (defect distances around 2-3 nm) verified that no Raman-active defects are introduced in the photochemical reaction. Since the substructure formation did not induce a D-mode, the iodination reaction could be monitored as a function of

the defect density by analyzing the two independent subsets of Raman signals. Statistical analysis revealed a strong negative dependence of the substructure formation on the presence of lattice defects since the intensity of the *trans*-oligoene modes decreases strongly as more lattice defects are introduced into the graphene. At an average defect spacing of ~1 nm no substructure formation was observed in agreement with previous reports, giving a lower limit for the size of the substructures probed at 532 nm. This explains lack of substructure formation upon iodination of highly-defective graphene in earlier studies. Based on the Raman shift of the *trans*-oligoene signals at around 1130 and 1500 cm^{-1} and the laser energy an average length of about eleven double bonds seems likely for the *trans*-oligoene substructures, derived by comparison with model molecules.

These results were explained using the previously proposed reaction mechanism. In contrast to the previously reported radical addition reactions where defects increase the reactivity of graphene by activating double bonds, the iodination reaction depends on the availability of intact graphene domains for substructure formation and is therefore negatively affected by lattice defects. As the average distance between defects decreases fewer substructures form and their average lengths becomes shorter.

The study extends the research from defect-free graphene to arbitrary graphene derivatives and highlights the novelty of the observed reactivity compared to other radical addition reactions. It demonstrates for the first time the use of statistical Raman spectroscopy in combination with defined defect densities to probe substructure properties due to their independent set of Raman signals.

6 Publications – Major Contributions

6.1 Evidence for *Trans*-Oligoene Chain Formation in Graphene Induced by Iodine

Authors	F. Grote, B.I. Weintrub, M. Kreßler, Q. Cao, C.E. Halbig, P. Kusch, K.I. Bolotin, S. Eigler
Journal	*Small* **2024**, e2311987.
DOI	10.1002/smll.202311987
Links	https://doi.org/10.1002/smll.202311987
Detailed scientific contribution	The concept of this manuscript was elaborated by F. Grote and S. Eigler. Samples were prepared and functionalized by F. Grote. Raman characterization was done by F. Grote. B.I. Weintrub fabricated transistor devices and performed transport measurements. M. Kreßler did KPFM measurements. Q. Cao fabricated heterostructures with hBN. C.E. Halbig performed XPS measurements. P. Kusch, K.I. Bolotin and S. Eigler supervised the experimental work. The manuscript was written by F. Grote with assistance from B.I. Weintrub and S. Eigler.
Estimated own contribution	~80%

NANO · MICRO small
www.small-journal.com

Evidence for *Trans*-Oligoene Chain Formation in Graphene Induced by Iodine

*Fabian Grote, Benjamin I. Weintrub, Mira Kreßler, Qing Cao, Christian E. Halbig, Patryk Kusch, Kirill I. Bolotin, and Siegfried Eigler**

Functionalization of pristine graphene by hydrogen and fluorine is well studied, resulting in graphane and fluorographene structures. In contrast, functionalization of pristine graphene with iodine has not been reported. Here, the functionalization of graphene with iodine using photochemical activation is presented, which is thermally reversible at 400 °C. Additional dispersive dominant Raman modes that are probed by resonance Raman spectroscopy are observed. Additionally, iodinated graphene is probed by Kelvin probe force microscopy and by transport measurements showing p-doping surpassing non-covalent iodine doping by charge transfer-complex formation. The emergent Raman modes combined with strong p-doping indicate that iodine functionalization is distinct from simple iodine doping. A reaction mechanism based on these findings is proposed, identifying the large size of iodine atoms as the probable cause governing regiochemically controlled addition due to steric hinderance of reactive sites. The modification of the electronic structure is explained by the confinement of 1D *trans*-oligoene chains between sp^3-defects. These results demonstrate the uniqueness of iodine reactivity toward graphene and the modification of the electronic structure of iodinated graphene, highlighting its dependence on the spatial arrangement of substituents.

1. Introduction

Pristine graphene is highly inert and requires harsh reaction conditions to form additional out-of-plane chemical bonds for developing advanced post-functionalization strategies.[1] Efficient methods have been developed to achieve the controlled functionalization of pristine graphene,[2] such as strong n-doping by alkali metals enabling the reaction with electrophiles, for example, diazonium ions or alkylhalides.[3] Another approach relies on cycloaddition reactions, for example with azido compounds.[4] Radical addition reactions have been widely used in graphene functionalization with hydrogen, oxygen,[5] halogens, alkyl, nitrenes, and phenyl groups.[2,6] However, they often require activated graphene, for example by defects. Therefore, reduced graphene oxide is often used as a defect-activated graphene starting material. In earlier studies, we demonstrated that organic and hydroxyl radicals preferentially react close to defect sites and thus, defects guide the regiochemical addition of addends.[7] Among the functionalization reactions of pristine graphene hydrogenation and fluorination have been widely studied. The syntheses of those materials typically require either preactivation by n-doping,[8] or high temperatures and highly reactive reactants such as fluorine or xenon difluoride making reaction control challenging.[9]

In contrast to the extensive reports of halogenation reactions including chlorine and bromine,[10] there is, to the best of our knowledge, no example of iodination of high-quality graphene. Previous studies have reported the iodination of graphene but using reduced graphene oxide as starting material, where the reactivity is dominated by defects.[11] Li et al. investigated the electrochemical iodination of graphene and found no reaction of iodine radicals with graphene but reported deposition of molecular iodine instead. This was explained by the lower reactivity of iodine radicals compared to other halogen radicals.[12] In addition to the bare halogenation reaction of graphene, the substantial van der Waals radius of iodine radicals (198 pm[13]) should result in distinctive regiochemical control of addition patterns on graphene[14], besides the most stable 1,2-addition.[15] However, thus far, only a few Raman studies have hinted at the existence of such reactivity, with minor Raman bands being reported for arylated graphene[16] and a few more accounts of similar modes can be found, which were assigned to *trans*-polyacetylene chain formation.[17] Similar signals in chlorinated graphene have been assigned to doping-activated Raman modes, making the

F. Grote, Q. Cao, C. E. Halbig, S. Eigler
Institut für Chemie und Biochemie
Freie Universität Berlin
Altensteinstraße 23a, 14195 Berlin, Germany
E-mail: siegfried.eigler@fu-berlin.de
B. I. Weintrub, M. Kreßler, P. Kusch, K. I. Bolotin
Institut für Physik
Freie Universität Berlin
Arnimallee 14, 14195 Berlin, Germany

The ORCID identification number(s) for the author(s) of this article can be found under https://doi.org/10.1002/smll.202311987

DOI: 10.1002/smll.202311987

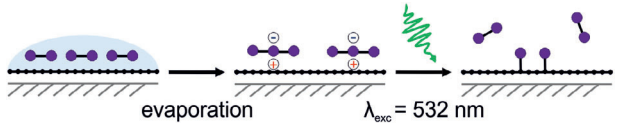

Figure 1. Schematic illustration of the iodination process. A solution of iodine in methanol is deposited on graphene supported on SiO_2/Si substrate. Upon evaporation of methanol, polyiodides I_3^- and I_5^- form by charge-transfer complex formation. Irradiation of this complex with λ_{exc} = 532 nm forms iodine radicals (Equation 1) that react with the graphene and excess iodine evaporates.

origin of these signals disputed.[18] Scanning tunneling microscopy (STM) experiments of hydrogen radicals on graphene allowed direct observation of effects of addition patterns on graphene properties.[19] Additionally, DFT calculations suggest considerable influence of the addition patterns on electronic and magnetic properties (e.g., bandgap opening).[20] To date, a lack of insight into possible reaction mechanisms prohibits the rational design of regular addition patterns on 2D materials.

Here, we present a novel approach to photochemically iodinate defect-free graphene after doping with polyiodides (**Figure 1**). We observe new dispersive Raman signals with unprecedented intensity and a strong p-doping effect measured by transport measurements, X-ray photoelectron spectroscopy (XPS), and Kelvin probe force microscopy (KPFM), that exceeds iodine doping. A reaction mechanism is proposed to explain the observed properties, in which steric hinderance of reactive sites due to the large iodine atom size forms well-defined addition patterns of *trans*-oligoene chains between sp^3-defects.

2. Results and Discussion

In this study, we used single-layer graphene obtained either by tape exfoliation or by chemical vapor deposition (CVD). With those approaches we ensure high quality of graphene to exclude dominant effects of pre-existing defects or residues from the fabrication process on the iodination reaction (Figure 1). To mitigate the influence of the substrate, we deposited monolayers of graphene on SiO_2, Au, and h-BN, respectively (Figure S1, Supporting Information). The graphene structures were thermally annealed (T = 200 °C, $p = 1 \times 10^{-3}$ mbar, 2 h) to ensure stable adhesion of graphene to the substrate and to remove volatile impurities. Before inducing the iodination reaction, the density of defects was quantified by Raman spectroscopy.

First, we deposited iodine onto graphene from a methanol solution (20 mM$_M$), leading to p-doping of graphene and polyiodide formation.[11a,21] After evaporation of methanol at room temperature, the doped graphene was iteratively irradiated using the laser of the Raman microscope (λ_{exc} = 532 nm, 3.03 mW, 30 accumulations). The Raman spectrum (**Figure 2**, purple spectrum) of iodinated graphene features two new dominant Raman modes at 1115 and 1498 cm^{-1}, while no new signals are observed on the substrate. This excludes reactions with the substrate or adsorbates as the cause of these signals. The observed signals were persistent after evaporation of iodine in a vacuum (T = rt, $p = 1 \times 10^{-3}$ mbar, 16 h) and washing with water or alcohols that should remove any non-covalently bound iodine. To gain further insights into the proceeding reaction, we elucidated the reaction mechanism, focusing our attention on the iodine species.

Polyiodides I_3^- and I_5^-, detected by Raman spectroscopy at 107 and 162 cm^{-1} (Figure S2, Supporting Information) are observed exclusively on graphene while no polyiodide signals are detected on the substrate. The doping effect is apparent by the shift of the G-peak by up to 15 cm^{-1} (Figure S2, Supporting Information) and partial 2D-peak suppression.[22] When iodine-doped graphene is irradiated with λ_{exc} = 532 nm, iodine radicals I$^\bullet$ and $I_2^{-\bullet}$ are generated through the photodissociation of I_3^- and I_5^- anions, as shown by Gardner et al. (Equation 1).[23]

$$I_3^- \xrightarrow{h\nu} [I_3^-]^* \rightarrow I_2^{-\cdot} + I^\cdot \quad (1)$$

The $I_2^{-\bullet}$ radical can further dissociate into an I$^\bullet$ radical and iodine anion.[13] While the photoredox chemistry of polyhalides is widely studied in metal halide complexes, examples on the photochemistry of halides at the surface of 2D materials are rare.[18a,24] The nascent radicals near the graphene surface subsequently react with sp^2-carbon atoms to form carbon-iodine bonds. Throughout this manuscript we will refer to the product of this reaction as "iodinated graphene" without distinction between tape-exfoliated and CVD graphene since we did not find a difference for the reactivity of the starting materials. Although only triiodide and pentaiodide are directly observed in the Raman spectra, higher polyiodides could form a network on the graphene surface.[25] To the best of our knowledge this is the first time that a photochemical reaction of a polyhalide and graphene is described. In contrast to the common evolution of Raman spectra of functionalized graphene,[26] the G/2D-ratio increases from 0.52 to 0.92 indicating increased disorder in the graphene lattice (Figure 2), however, no D-peak at ≈1340 cm^{-1} is observed.

Signals with smaller intensity evolve (ν_2, $2\nu_1$, and $\nu_1+\nu_3$, Figure 2), of which a detailed description can be found in the SI (Figure S3A, Supporting Information). The lack of a D-peak

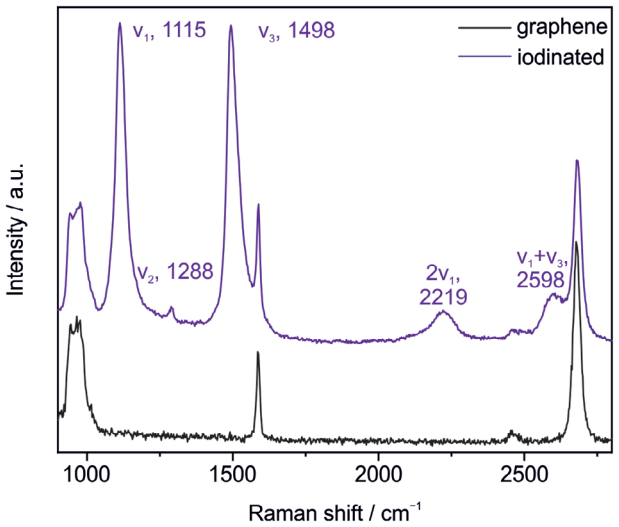

Figure 2. Raman spectrum (λ_{exc} = 532 nm) of tape-exfoliated graphene on SiO_2/Si before (black) and after iodination (purple). Two strong new modes (ν_1, ν_3) and three smaller modes (ν_2, $2\nu_1$, and $\nu_1+\nu_3$) are observed in the same range.

either indicates absence of functionalization or formation of Raman silent defects, as reported, for example, for zigzag edges, charged impurities, and intercalants.[27]. Raman probing iodinated samples with λ_{exc} = 638 nm (1.94 eV) shows dispersion of the new Raman modes and a strong change in the intensity relative to the graphene signals (**Figure 3A**). At higher excitation energies (λ_{exc} = 405 nm, 3.06 eV) no Raman modes were observed, while the signal intensities measured at longer wavelengths were shifted after irradiation due to defunctionalization (Figure S5A, Supporting Information). Surprisingly, in some areas of the sample, using the same reaction conditions, the G- and 2D-peaks typical for graphene completely vanish, indicating the formation of a new material (Figure 3B). A strong increase of the photoluminescence background is observed and formation of two strong new signals at 1121 and 1504 cm^{-1} that show a striking similarity to *trans*-polyacetylene (Table S1, Supporting Information). *Trans*-polyacetylene has two strong modes at 1125 and 1512 cm^{-1} (upon irradiation with λ_{exc} = 532 nm[28]) and a similar pattern of signals and overtones.[29] It also shows resonance Raman effects due to the chainlength-dependent bandgap and a large Raman cross section leads to high intensities of the Raman modes (Figure S4A, Supporting Information).[30] The Raman results therefore suggest a structure like *trans*-polyacetylene polymer (Figure S3B, Supporting Information). Those localized conjugated double bonds may result from a regioselective addition reaction of large and sterically demanding iodine atoms to graphene. To distinguish the structures in iodinated graphene from *trans*-polyacetylene, where each carbon atom is bonded to a hydrogen atom, we refer to the chains we propose in iodinated graphene as *trans*-oligoene chains. These 1D carbon chains are bonded to carbon atoms within the graphene structure, have varying finite lengths and are spread randomly across the iodinated graphene area with an unknown distribution. While we expect different Raman signal positions between *trans*-polyacetylene and graphene-embedded *trans*-oligoenes, we expect to observe similar trends depending on the chain length due to bandgap opening.[31]

The reversibility of iodination reactions is of special interest for patterning applications, for example, for writing, reading, and erasing information.[18b] Thus, we investigated the thermal defunctionalization of iodinated graphene, which we find to occur between 150 and 400 °C. Interestingly, a thermal iodination of graphene occurs without irradiation, as identified by the appearance of similar but less intense Raman modes at 150 °C under ambient conditions (Figure S6, Supporting Information). After extended times of vacuum annealing at 200 °C, an increase of the new modes is observed that remain stable up to 300 °C. This may be due to iodine intercalated between graphene and the SiO_2 substrate that is unable to evaporate, and thus, the iodine can react with graphene.[21b] Heating of iodinated graphene to 400 °C removes the new modes and a broad D-peak at 1349 cm^{-1} (FWHM = 171 cm^{-1}) forms. Additionally, the base of the G-peak broadens, while the top remains sharp (Figure 3C). The broad D-peak is reminiscent of disordered carbon[32] and may originate from amorphous carbon on the graphene surface formed by graphitization of organic adsorbates from the environment.[33] Defunctionalization was also observed when high laser intensities were used, probably due to local heating or assisted photochemical bond dissociation, shifting the distribution of *trans*-

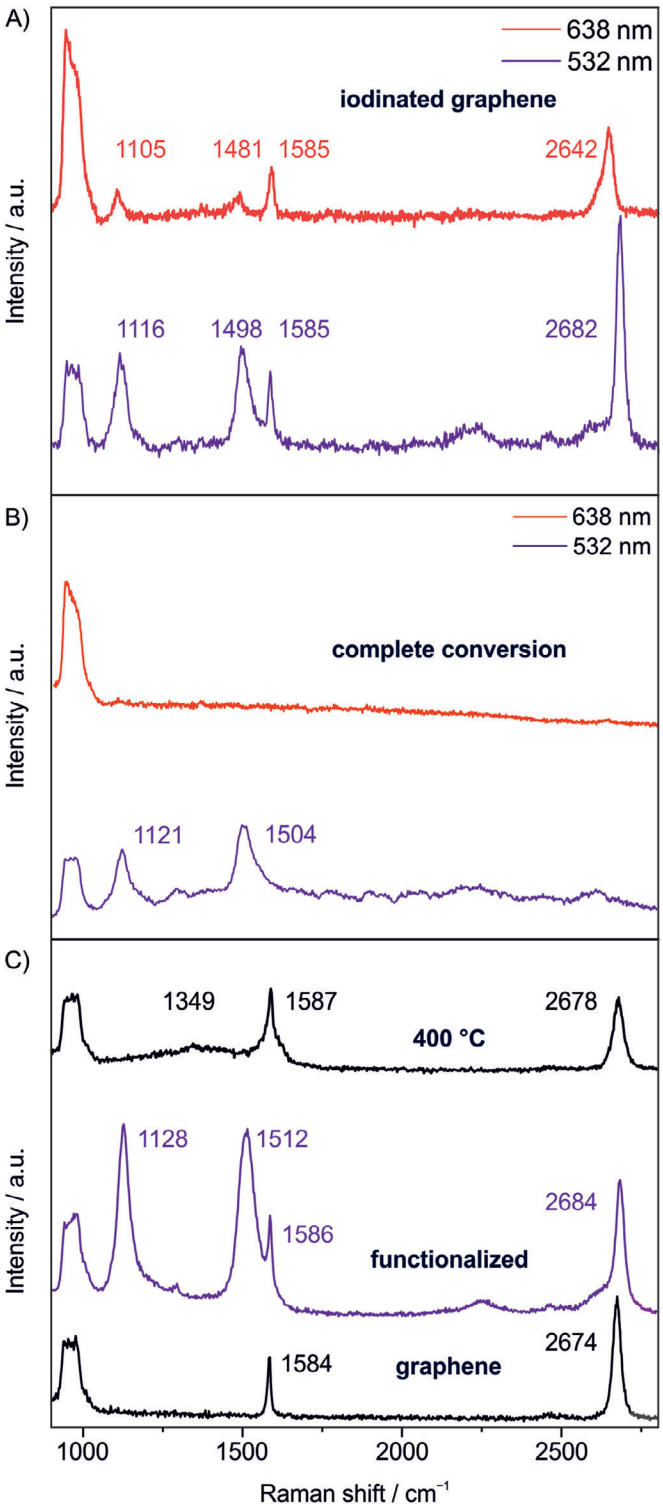

Figure 3. A) Raman spectra of tape-exfoliated graphene on hBN/SiO_2/Si after iodination measured at 532 nm (purple) and 638 nm (red), showing signal dispersion and a strong decrease of intensity relative to the graphene signals. B) Example spectra of vanished graphene Raman modes. No Raman signals are observed at 638 nm indicating the complete conversion of graphene. C) Raman spectra of pristine tape-exfoliated graphene, iodinated graphene, and graphene annealed at 400 °C. The graphene rests on a SiO_2/Si substrate.

oligoene chains (Figure S5B, Supporting Information). The high thermal stability indicates a thermodynamically stable structure.

With XPS the halogen content was determined and covalent bond formation of halogens to graphene was confirmed.[34] We functionalized CVD graphene on a large area (Figure S7A, Supporting Information) and thoroughly washed it (water, isopropanol, acetone) to remove all residues on the material before measurements. The survey spectrum (Figure S7B, Supporting Information) shows the characteristic I $3d_{5/2}$ and I $3d_{3/2}$ peaks at 619.5 and 630.5 eV respectively, but with very low signal intensities (Figure S7C, Supporting Information). The deconvolution of the C 1s signal shows no significant change of the carbon composition (Figure S7D, Supporting Information), as expected due to the small amount of iodine present. With respect to the intensity of the C 1s peak at ≈284.4 eV, we estimated the atomic ratio of iodine to carbon to be ≈1–300. Thus, deconvolution of the high-resolution C 1s and I 3d core spectra cannot provide further meaningful information due to the small signal-to-noise ratio in the present spectra. Hence C 1s core spectra of graphene before and after functionalization are practically similar (Figure S7D–F, Supporting Information).

Similar Raman signals emerge when graphene is irradiated under similar conditions with bromine instead of iodine (Figure S8D, Supporting Information). The larger difference of electronegativity between carbon and bromine should cause a stronger separation of XPS signals. We thermally brominated CVD graphene (Figure S9A, Supporting Information) to ensure homogenous functionalization across a large sample. The survey spectrum shows the characteristic Br 3d peak at 70 eV albeit with a low intensity (Figure S9B,C, Supporting Information) but the broadness of the bromine high resolution Br 3d core spectrum indicates the presence of C—Br bonds.[35] Deconvolution of the C 1s signal showed no significant change of the carbon composition, as expected from the low intensity of the bromine signals (Figure S9D, Supporting Information).

The introduction of semiconductive *trans*-oligoene chains and difference in electronegativity between carbon and iodine should cause p-doping of the iodinated graphene. To test this, we performed electrical transport measurements on graphene transistors before and after iodination. In contrast to Raman spectroscopy where we can only observe a small portion of the *trans*-oligoene chain distribution the entire system is probed in transport measurements. The carrier density of graphene for the transport measurements can be calculated using Equation 2, where n = carrier density, C = total areal capacitance, V_g = gate voltage, V_{CNP} = charge neutrality point, and e = elementary charge.

$$n = C\frac{(V_g - V_{CNP})}{e} \quad (2)$$

We find that pristine graphene has a carrier density of 0.9 × 10^{12} holes cm^{-2} (V_{CNP} = 11.5 V), probably due to the SiO_2 substrate as well as water and impurities trapped between graphene and the substrate.[36] Graphene exposed to gaseous iodine is also p-doped due to charge-transfer complex formation.[37] Measurements of iodine-doped graphene prepared by our process under ambient conditions showed decreasing doping levels during the measurement (≈30 min) due to its considerable vapor pressure and did not exceed 3.2 × 10^{12} holes cm^{-2} (V_{CNP} = 43 V), consistent with literature values (Figure S10C, Supporting Information). To minimize iodine doping effects in our device, we stored the samples under high vacuum conditions (≈10^{-5} mbar) for several hours to evaporate any leftover iodine from the functionalization process. Iodination strongly increased the hole density to 5.8 × 10^{12} holes cm^{-2} (V_{CNP} = 77 V, **Figure 4A**), corresponding to a Fermi energy difference of ΔE_F = 173 meV, exceeding doping levels from charge-transfer into polyiodide molecules. A significant hysteresis is observed for iodinated graphene that is distinct from the pristine or iodine-doped graphene. This may be explained by capacitive charging of trap states that are formed by the *trans*-oligoene chains.[38] In contrast to iodine-doped graphene, the carrier density was stable under vacuum conditions and over several gate voltage sweeps, since the covalently attached iodine is not removed in low pressure conditions (Figure S10D, Supporting Information). It is interesting to note that iodine functionalization induces a free carrier concentration in graphene close to the limit of conventional SiO_2 gating. Other halogenated graphene devices showed strong p-doping as well, however in these examples no V_{CNP} of the functionalized graphene were reported, due to the limited measurement window.[24,39] Calculating carrier densities is limited, since it relies on accurately extracting V_{CNP} from the transport curves, which is in some cases beyond the range of V_g values which could be applied without destroying the sample.

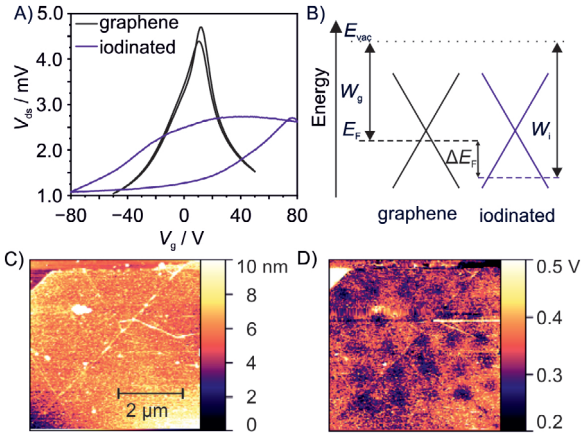

Figure 4. A) Drain-source voltage versus gate voltage of graphene field-effect transistor before (black) and after (purple) iodination. B) Energy level diagram of graphene and iodinated graphene. The Fermi energy (E_F) is significantly decreased upon iodination as evidenced by KPFM and transport data. C) Topography image of iodinated CVD graphene showing no signs of patterning. D) KPFM image of the same area. A 4 × 4 µm pattern was made by irradiation with λ_{exc} = 532 nm and 1 µm step size, visualized by black dots wihich indicate a lower work function relative to unfunctionalized areas.

Thus, we used KPFM as a complementary experimental method to measure local carrier density differences. The work function difference of pristine (W_g) and iodinated areas (W_i) directly corresponds to the difference of the Fermi level ($\Delta E_F = W_i - W_g$) of the two areas (Figure 4B). We measured KPFM on a graphene flake with both pristine and iodinated areas and compared the work functions between these areas to calculate a local work function difference. The topographic scan shows

no significant variation of sample height between pristine and iodinated areas (Figure 4C), but the overall height of the monolayer reveals the presence of adsorbates despite extensive washing (water, isopropanol, acetone) and evaporation in vacuum. If the material properties would result from adsorbates on the surface of graphene, differences in the intensity of the Raman and KPFM signals must be detectable between cleaned and uncleaned domains. To investigate this we measured Raman spectra and KPFM of the CVD graphene sample before (Figure 4C,D) and after (Figure S11D,E, Supporting Information) removal of adsorbates by mechanical cleaning with an AFM tip.[40] After cleaning of the graphene surface, the ν_1 and ν_3 mode remain unchanged in the cleaned areas while no change of Raman signal was observed for the piled adsorbates (Figure S11B,C, Supporting Information). Also, the work function patterns remain in the KPFM image (Figure S11E–I, Supporting Information), while the contrast between functionalized and unfunctionalized areas is improved due to the removal of adsorbates with a higher work function (Figure S11G,I, Supporting Information). No change of the Raman signals of brominated graphene (Figure S8C,D, Supporting Information) was observed after mechanical cleaning. The adsorbates therefore have no significant influence on the material properties and consequently, the new Raman modes must stem from the carbon lattice.

To extract a reliable work function difference, we prepared a tape-exfoliated graphene sample contacted with a gold electrode to ensure proper grounding (Figure S12A, Supporting Information). The sample was patterned, and the functionalization was followed by Raman spectroscopy (Figure S12B, Supporting Information). The average difference of the work function between pristine and iodinated areas measured by KPFM was 141.5 meV (Figure S12C–E and Table S2, Supporting Information). This is in good agreement with ΔE_F extracted from transport measurements (173 meV) considering that these two values are measured on different samples and by different techniques. The observed shift of E_F suggests that the carrier density changes by iodination exceed iodine doping and are stable against decay by iodine evaporation.

In an earlier report by Englert et al. small Raman modes at 1139 and 1512 cm^{-1} (λ_{exc} = 532 nm) were observed in the covalent functionalization of graphene with aryl radicals, similar to the ν_1 and ν_3 modes of iodinated graphene.[16] They assigned the observed modes to *trans*-oligoene chains formed within areas defined by sp^3-defects based on their similarity to Raman modes observed in nano-crystalline diamond samples.[30] Similar modes were observed upon photochlorination of graphene with chlorine gas; again with relatively low intensities.[18] They assigned the signals to effects of strong doping by chlorine addition leading to symmetry lowering and zone folding that activate new Raman modes by comparison to potassium-doped graphene (n-doped).[41] The modes observed in that system however are observed at 1134 and 1267 cm^{-1} while no signal ≈1500 cm^{-1} was observed that would account for the ν_3-modes. Instead, a Fano-shaped G-peak is observed and such a mode is also not predicted by calculations of the Raman modes of KC_8.[42] If the observed Raman modes would arise from a doping effect, then they should evolve without irradiation of the sample and should be sensitive toward removal of the dopant by washing or evaporation. Interestingly, in other reports of chlorination of graphene, these spectral features were not reported.[12,24,43] We find that the spectral modes of the polyiodides vanish, while two strong new modes appear (Figure 2), which we would not expect for a non-covalent polyiodide network. The Raman modes of iodinated graphene are also persistent under ambient and high vacuum conditions or washing with water and organic solvents in contrast to the polyiodide signals. The complete disappearance of graphene Raman signals in some areas and the dispersive nature of the Raman modes indicate the direct interaction with the carbon lattice. Their unprecedented intensity allowed us to observe the ν_2 mode and additional overtone modes that have not been reported for any functionalized graphene before and further indicate an origin from a *trans*-polyacetylene like structure. Their strong p-doping effect exceeds doping by non-covalently adsorbed polyiodides as shown by transport and KPFM measurements, and the weak doping effect of iodine makes doping-activated Raman modes appear unlikely.

We explain these experimental results by the formation of *trans*-oligoene chains formed with regiochemical control due to the large iodine size. Their formation depends on the reactivity of the iodine radical on the graphene sheet,[44] since the reaction of an iodine radical with graphene forms a π-radical that initially resides in a non-bonding orbital adjacent to the iodine addition site (**Figure 5**A). The delocalization of the π-radical was directly observed for hydrogenated graphene by STM causing a long-range modification of the local spin density of states and showing a threefold symmetry,[45] reaching as far as 6 nm or 20–25 lattice constants.[45] It corresponds to the delocalization of the π-radical on the B sublattice and can be interpreted as delocalization along the *trans*-oligoene paths shown in red in Figure 5B. The highest spin density, and therefore highest reactivity, is located on the three carbon atoms in 1,2-position adjacent to the addition site and at the 3 *cis*-1,4-positions (grey, Figure 5B) across six-membered rings[46] and the second hydrogen radical addition thus occurs at these positions, as observed experimentally.[15] The high reactivity of radicals may enable other addition patterns to form under kinetic control,[14] but here the low reactivity of iodine radicals is expected to lead to thermodynamic rather than kinetic reactivity. Equally important, addition in the 1,2-position is sterically blocked by iodine due to the large van der Waals radii of the iodine atoms (198 pm) and the resulting electrostatic repulsion.[13] The *cis*-1,4-addition motif (A, Figure 5C) leads to a separation of the iodine pair of 284 pm (assuming C—C bond distance of 142 pm), which is only slightly longer than the covalent bond length of diiodine (267 pm), making it also unlikely. By addition in the *trans*-1,4-position (B, Figure 5C) the defect distance is 376 pm, making a stable addition possible, explaining the observed regioselectivity. Since in our experiment the whole surface is covered with iodine, the second reaction step may be very fast and could potentially even extend beyond the irradiated area due to the delocalization of the π-radical on the graphene sheet. The confinement of localized double bonds between sp^3-defects induces bond length alternation through Peierls distortion, causing chain-length dependent local bandgap opening and hence resonance Raman effect.[47] A distribution of various chain lengths is formed that explains the varying intensities and dispersion of the Raman modes (Figures S4B and S5B, Supporting Information).

Up to three *trans*-oligoene chains may form from a single sp^3-defect, following the symmetry observed for the spin

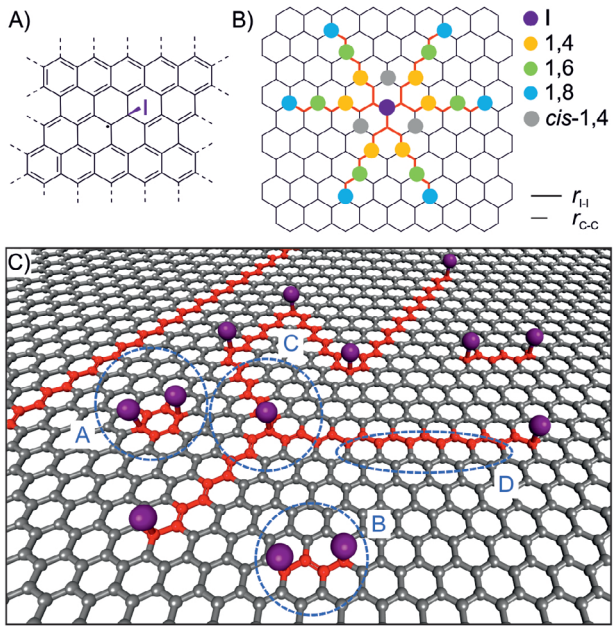

Figure 5. A) Addition of an iodine radical to graphene. The π-radical is located adjacent to the sp^3-defect and can be delocalized on the sublattice. B) Scheme showing potential sites for secondary iodine addition on graphene forming all-*trans*-oligoene chains. The 1,2-, and *cis*-1,4 positions are precluded due to iodine atom size and I-I bond length (bottom right). C) Schematic illustration of the proposed iodinated graphene structure, explaining the observed Raman signals and doping properties. *Trans*-oligoene chains (red) with varying lengths and localized double bonds are embedded in graphene domains (grey) with a delocalized π-system. A The *cis*-1,4-addition is unlikely given the small I-I distance, despite the high spin density in this position. B Addition along a *trans*-1,4-oligoene chain ensures sufficient distance between iodine atoms. C Up to three *trans*-oligoene chains can extend from a single sp^3-defect, connecting to adjacent sp^3-defects across the graphene sheet. D Perfect zigzag edges separate the chains from graphene domains along the length of the chains. The delocalized double bonds have been omitted for clarity.

density (C, Figure 5C). The absence of a D-peak in the Raman spectra can be attributed to the perfect zigzag edges to the neighboring graphene domains (D, Figure 5C), rendering them Raman silent.[27,48] The polydisperse nature of iodinated graphene makes it impossible to give a definite structure since the patterns formed will be randomly distributed across the illuminated area and only a small part of the distribution is probed at a given laser wavelength matching the bandgap of the chains. As more and more radicals are added to the graphene sheet more conjugated double bonds become confined between defects and the uninterrupted graphene domains become smaller. The distribution of *trans*-oligoene chains will shift due to the decreasing defect distance, making long chains less likely.

3. Conclusion

In summary, defect-free graphene was functionalized by a photochemical iodination reaction for the first time and strong new Raman modes were observed. Thermal reversibility of the reaction, dispersion of Raman modes and complete disappearance of graphene Raman modes in some areas indicate the interaction of iodine with the graphene lattice carbon atoms. KPFM and transport measurements demonstrate the strong p-doping effect of iodinated graphene, exceeding non-covalent iodine doping. Due to the size of iodine atoms the usually observed 1,2- and *cis*-1,4-position addition patterns are sterically hindered, leading to regioselective functionalization of graphene, and generating *trans*-oligoene substructures. Those *trans*-oligoene structures generate new Raman modes by the isolation of conjugated double bonds between sp^3-defects. The proposed structure and reaction mechanism will serve as a starting point for further experimental and theoretical inquiries toward the rational design of regioselective patterning of graphene. The iodination-based functionalization approach paths a way to patterning applications accompanied with a strong p-doping effect and the ability of readout due to the strong Raman modes.

Supporting Information

Supporting Information is available from the Wiley Online Library or from the author.

Acknowledgements

S.E. and F.G. gratefully acknowledge funding from the Deutsche Forschungsgemeinschaft (DFG, German Research Foundation, Project No. 392444269).

Open access funding enabled and organized by Projekt DEAL.

Conflict of Interest

The authors declare no conflict of interest.

Data Availability Statement

The data that support the findings of this study are available in the supplementary material of this article.

Keywords

addition patterns, graphene, iodination, Raman spectroscopy, *trans*-oligoene

Received: December 21, 2023
Revised: February 6, 2024
Published online:

[1] a) T. Wei, X. Liu, M. Kohring, S. Al-Fogra, M. Moritz, D. Hemmeter, U. Paap, C. Papp, H. P. Steinrück, J. Bachmann, H. B. Weber, F. Hauke, A. Hirsch, *Angew. Chem., Int. Ed.* **2022**, *61*, e202201169; b) M. Z. Hossain, M. B. A. Razak, H. Noritake, Y. Shiozawa, S. Yoshimoto, K. Mukai, T. Koitaya, J. Yoshinobu, S. Hosaka, *J. Phys. Chem. C* **2014**, *118*, 22096.

[2] C. Wetzl, A. Silvestri, M. Garrido, H. L. Hou, A. Criado, M. Prato, *Angew. Chem., Int. Ed.* **2023**, *62*, e202212857.

[3] G. Abellan, M. Schirowski, K. F. Edelthalhammer, M. Fickert, K. Werbach, H. Peterlik, F. Hauke, A. Hirsch, *J. Am. Chem. Soc.* **2017**, *139*, 5175.

[4] H. Qin, T. Hwang, C. Ahn, J. A. Kim, Y. Jin, Y. Cho, C. Shin, T. Kim, *J. Nanosci. Nanotechnol.* **2016**, *16*, 5034.
[5] M. Z. Hossain, J. E. Johns, K. H. Bevan, H. J. Karmel, Y. T. Liang, S. Yoshimoto, K. Mukai, T. Koitaya, J. Yoshinobu, M. Kawai, A. M. Lear, L. L. Kesmodel, S. L. Tait, M. C. Hersam, *Nat. Chem.* **2012**, *4*, 305.
[6] A. Criado, M. Melchionna, S. Marchesan, M. Prato, *Angew. Chem., Int. Ed.* **2015**, *54*, 10734.
[7] a) C. E. Halbig, R. Lasch, J. Krüll, A. S. Pirzer, Z. Wang, J. N. Kirchhof, K. I. Bolotin, M. R. Heinrich, S. Eigler, *Angew. Chem., Int. Ed.* **2019**, *58*, 3599; b) Y. Wang, F. Grote, Q. Cao, S. Eigler, *J. Phys. Chem. Lett.* **2021**, *12*, 10009.
[8] R. A. Schäfer, D. Dasler, U. Mundloch, F. Hauke, A. Hirsch, *J. Am. Chem. Soc.* **2016**, *138*, 1647.
[9] R. A. Borse, M. B. Kale, S. H. Sonawane, Y. Wang, *Adv. Funct. Mater.* **2022**, *32*, 2202570.
[10] F. Karlicky, K. Kumara Ramanatha Datta, M. Otyepka, R. Zboril, *ACS Nano* **2013**, *7*, 6434.
[11] a) P. Šimek, K. Klímová, D. Sedmidubský, O. Jankovský, M. Pumera, Z. Sofer, *Nanoscale* **2015**, *7*, 261; b) M. S. Mirshekarloo, M. C. D. Cooray, P. Jovanović, C. D. Easton, F. Wu, T. D. Gamot, M. J. Abedin, M. R. Yuce, M. Shaibani, M. Majumder, *Batter. Supercaps* **2021**, *4*, 1175; c) A. Wang, S. Bok, C. J. Mathai, K. Gangopadhyay, J. McFarland, M. R. Maschmann, S. Gangopadhyay, *Nano Futures* **2020**, *4*, 045002; d) X. Zhang, G. Lu, *Carbon* **2016**, *108*, 215.
[12] W. Li, Y. Li, K. Xu, *Nano Lett.* **2021**, *21*, 1150.
[13] L. Troian-Gautier, M. D. Turlington, S. A. M. Wehlin, A. B. Maurer, M. D. Brady, W. B. Swords, G. J. Meyer, *Chem. Rev.* **2019**, *119*, 4628.
[14] S. Niyogi, E. Bekyarova, J. Hong, S. Khizroev, C. Berger, W. de Heer, R. C. Haddon, *J. Phys. Chem. Lett.* **2011**, *2*, 2487.
[15] R. Balog, B. Jorgensen, J. Wells, E. Laegsgaard, P. Hofmann, F. Besenbacher, L. Hornekaer, *J. Am. Chem. Soc.* **2009**, *131*, 8744.
[16] J. M. Englert, C. Dotzer, G. Yang, M. Schmid, C. Papp, J. M. Gottfried, H. P. Steinrück, E. Spiecker, F. Hauke, A. Hirsch, *Nat. Chem.* **2011**, *3*, 279.
[17] a) V. Nagyte, D. J. Kelly, A. Felten, G. Picardi, Y. Shin, A. Alieva, R. E. Worsley, K. Parvez, S. Dehm, R. Krupke, S. J. Haigh, A. Oikonomou, A. J. Pollard, C. Casiraghi, *Nano Lett.* **2020**, *20*, 3411; b) Z. Wang, Q. Yao, C. Neumann, F. Börrnert, J. Renner, U. Kaiser, A. Turchanin, H. J. W. Zandvliet, S. Eigler, *Angew. Chem., Int. Ed.* **2020**, *59*, 13657.
[18] a) G. Copetti, E. H. Nunes, G. K. Rolim, G. V. Soares, S. A. Correa, D. E. Weibel, C. Radtke, *J. Phys. Chem. C* **2018**, *122*, 16333; b) Y. Rho, K. Lee, L. Wang, C. Ko, Y. Chen, P. Ci, J. Pei, A. Zettl, J. Wu, C. P. Grigoropoulos, *Nat. Electron.* **2022**, *5*, 505.
[19] H. González-Herrero, J. M. Gómez-Rodríguez, P. Mallet, M. Moaied, J. J. Palacios, C. Salgado, M. M. Ugeda, J. Y. Veuillen, F. Yndurain, I. Brihuega, *Science* **2016**, *352*, 437.
[20] a) I. A. Popov, Y. Li, Z. Chen, A. I. Boldyrev, *Phys. Chem. Chem. Phys.* **2013**, *15*, 6842; b) F. Marsusi, N. D. Drummond, M. J. Verstraete, *Carbon* **2019**, *144*, 615; c) P. A. Denis, *ChemPhysChem* **2013**, *14*, 3271.
[21] a) Z. Yao, H. Nie, Z. Yang, X. Zhou, Z. Liu, S. Huang, *Chem. Commun.* **2012**, *48*, 1027; b) N. Jung, A. C. Crowther, N. Kim, P. Kim, L. Brus, *ACS Nano* **2010**, *4*, 7005.
[22] N. Jung, N. Kim, S. Jockusch, N. J. Turro, P. Kim, L. Brus, *Nano Lett.* **2009**, *9*, 4133.
[23] J. M. Gardner, M. Abrahamsson, B. H. Farnum, G. J. Meyer, *J. Am. Chem. Soc.* **2009**, *131*, 16206.
[24] B. Li, L. Zhou, D. Wu, H. Peng, K. Yan, Y. Zhou, Z. Liu, *ACS Nano* **2011**, *5*, 5957.
[25] P. H. Svensson, L. Kloo, *Chem. Rev.* **2003**, *103*, 1649.
[26] J. M. Englert, P. Vecera, K. C. Knirsch, R. A. Schäfer, F. Hauke, A. Hirsch, *ACS Nano* **2013**, *7*, 5472.
[27] A. C. Ferrari, D. M. Basko, *Nat. Nanotechnol.* **2013**, *8*, 235.
[28] M. Tasumi, H. Yoshida, M. Fujiwara, H. Hamaguchi, H. Shirakawa, *Synth. Met.* **1987**, *17*, 319.
[29] V. Rives-Arnau, N. Sheppard, *J. Chem. Soc., Faraday Trans.* **1980**, *76*, 394.
[30] A. C. Ferrari, J. Robertson, *Phys. Rev. B* **2001**, *63*, 075414.
[31] a) H. E. Schaffer, R. R. Chance, R. J. Silbey, K. Knoll, R. R. Schrock, *J. Chem. Phys.* **1991**, *94*, 4161; b) K. Furuya, A. Sakamoto, M. Tasumi, *J. Phys. Chem. A* **2023**, *127*, 5344.
[32] A. C. Ferrari, J. Robertson, *Phys. Rev. B* **2000**, *61*, 14095.
[33] J. Hong, M. K. Park, E. J. Lee, D. Lee, D. S. Hwang, S. Ryu, *Sci. Rep.* **2013**, *3*, 2700.
[34] X. Tang, T. Fan, C. Wang, H. Zhang, *Small* **2021**, *17*, e2005640.
[35] O. Jankovsky, P. Simek, K. Klimova, D. Sedmidubsky, S. Matejkova, M. Pumera, Z. Sofer, *Nanoscale* **2014**, *6*, 6065.
[36] Z. Wang, Q. Yao, Y. Hu, C. Li, M. Hussmann, B. Weintrub, J. N. Kirchhof, K. Bolotin, T. Taniguchi, K. Watanabe, S. Eigler, *RSC Adv.* **2019**, *9*, 38011.
[37] S. W. Chu, S. J. Baek, D. C. Kim, S. Seo, J. S. Kim, Y. W. Park, *Synth. Met.* **2012**, *162*, 1689.
[38] a) H. Wang, Y. Wu, C. Cong, J. Shang, T. Yu, *ACS Nano* **2010**, *4*, 7221; b) T. S. Sreeprasad, V. Berry, *Small* **2013**, *9*, 341.
[39] a) X. Zhang, A. Hsu, H. Wang, Y. Song, J. Kong, M. S. Dresselhaus, T. Palacios, *ACS Nano* **2013**, *7*, 7262; b) L. Zhou, L. Zhou, M. Yang, D. Wu, L. Liao, K. Yan, Q. Xie, Z. Liu, H. Peng, Z. Liu, *Small* **2013**, *9*, 1388.
[40] A. M. Goossens, V. E. Calado, A. Barreiro, K. Watanabe, T. Taniguchi, L. M. K. Vandersypen, *Appl. Phys. Lett.* **2012**, *100*, 073110 .
[41] N. Jung, B. Kim, A. C. Crowther, N. Kim, C. Nuckolls, L. Brus, *ACS Nano* **2011**, *5*, 5708.
[42] C. Horie, M. Maeda, Y. Kuramoto, *Physica B+C* **1980**, *99*, 430.
[43] a) L. Bao, B. Zhao, B. Yang, M. Halik, F. Hauke, A. Hirsch, *Adv. Mater.* **2021**, *33*, 2101653; b) T. Wei, M. Kohring, H. B. Weber, F. Hauke, A. Hirsch, *Nat. Commun.* **2021**, *12*, 552; c) M. Yang, L. Zhou, J. Wang, Z. Liu, Z. Liu, *J. Phys. Chem. C* **2011**, *116*, 844.
[44] D. E. Jiang, B. G. Sumpter, S. Dai, *J. Phys. Chem. B* **2006**, *110*, 23628.
[45] P. Ruffieux, O. Groning, P. Schwaller, L. Schlapbach, P. Groning, *Phys. Rev. Lett.* **2000**, *84*, 4910.
[46] O. V. Yazyev, L. Helm, *Phys. Rev. B* **2007**, *75*, 125408.
[47] C. Castiglioni, M. Tommasini, G. Zerbi, *Philos. Trans. R. Soc. A* **2004**, *362*, 2425.
[48] C. Casiraghi, A. Hartschuh, H. Qian, S. Piscanec, C. Georgi, A. Fasoli, K. S. Novoselov, D. M. Basko, A. C. Ferrari, *Nano Lett.* **2009**, *9*, 1433.

NANO · MICRO
small

Supporting Information

for *Small*, DOI 10.1002/smll.202311987

Evidence for *Trans*-Oligoene Chain Formation in Graphene Induced by Iodine

*Fabian Grote, Benjamin I. Weintrub, Mira Kreßler, Qing Cao, Christian E. Halbig, Patryk Kusch, Kirill I. Bolotin and Siegfried Eigler**

Supporting Information

69451 Weinheim, Germany

Evidence for *trans*-Oligoene Chain Formation in Graphene Induced by Iodine

Fabian Grote,[a] Benjamin I. Weintrub,[b] Mira Kreßler,[c] Qing Cao,[a] Christian E. Halbig,[a] Patryk Kusch,[c] Kirill I. Bolotin[b] and Siegfried Eigler*[a]

[a] M.Sc. F. Grote, M.Sc. Q. Cao, Dr. C.E. Halbig, Prof. Dr. S. Eigler
Institut für Chemie und Biochemie
Freie Universität Berlin
Altensteinstraße 23a, D-14195 Berlin, Germany
E-mail: siegfried.eigler@fu-berlin.de
[b] M.A. B.I. Weintrub, Prof. Dr. K.I. Bolotin
Institut für Physik
Freie Universität Berlin
Arnimallee 14, D-14195 Berlin, Germany
[c] B.Sc. M. Kreßler, Dr. P. Kusch
Institut für Physik
Freie Universität Berlin
Arnimallee 14, D-14195 Berlin, Germany

Abstract: Functionalization of pristine graphene by hydrogen and fluorine is well studied, resulting in graphane and fluorographene structures. In contrast, functionalization of pristine graphene with iodine has not been reported. Here, the functionalization of graphene with iodine using photochemical activation is presented, which is thermally reversible at 400 °C. Additional dispersive dominant Raman modes that are probed by resonance Raman spectroscopy are observed. Additionally, iodinated graphene is probed by Kelvin probe force microscopy and by transport measurements showing p-doping surpassing non-covalent iodine doping by charge transfer-complex formation. The emergent Raman modes combined with strong p-doping indicate that iodine functionalization is distinct from simple iodine doping. A reaction mechanism based on these findings is proposed, identifying the large size of iodine atoms as the probable cause governing regiochemically controlled addition due to steric hinderance of reactive sites. The modification of the electronic structure is explained by the confinement of 1D *trans*-oligoene chains between sp^3-defects. These results demonstrate the uniqueness of iodine reactivity toward graphene and the modification of the electronic structure of iodinated graphene, highlighting its dependence on the spatial arrangement of substituents.

DOI: 10.1002/smll.202311987

Experimental Procedures

Materials and chemicals: Methanol used for sample preparation was distilled in a solvent circulation apparatus to remove any impurities before use. Iodine was purchased from TCI and was used as-received. For tape-exfoliation of graphene Kish graphite (Grade 200) from Graphene Supermarket was used. Si wafers with a 300 nm thick SiO_2 layer were purchased from Fraunhofer Institut für Integrierte Systeme und Bauelementetechnologie IISB in Erlangen.

Raman spectroscopy: Raman spectra were measured on a Horiba Jobin Yvon XploRA™ PLUS spectrometer equipped with a confocal microscope and an automated XYZ table at 532 nm (2.33 eV) combined with a 100x objective (NA = 0.9). The Raman shift was calibrated to the Si peak before measurement. Experiments using 638 nm (1.94 eV) laser light were performed on a Horiba Jobin Yvon XploRA™ spectrometer equipped with a 532 nm and 638 nm laser source and 100x objective (NA = 0.9). Experiments using 633 nm (1.96 eV) and 405 nm (3.06 eV) laser light were performed on a Horiba Jobin Yvon LabRAM Evolution spectrometer equipped with a 405 nm, 532 nm, and 633 nm laser source and 100x objective (NA = 0.9).

SUPPORTING INFORMATION

Atomic Force Microscopy (AFM) and Kelvin Probe Force Microscopy (KPFM): KPFM experiments were conducted under ambient conditions using the neaSNOM that is a scattering type scanning near-field optical microscope with a KPFM extension (neaSPEC). We used Pt-Ir coated Si tips (ACCESS-EFM probes, AppNano, k = 2.7 N m^{-1}). The setup operates in non-contact mode. AM-KPFM was used, which is sensitive to electrostatic forces and the surface potential measured. The work function of the samples (Φ_{sample}) is defined by the following formula, $\Phi_{sample} = q\ V_{CPD} + \Phi_{tip}$, where V_{CPD} is the contact potential difference measured by the KPFM, Φ_{tip} is the work function of the tip, and q is the elementary charge. The potential profile is measured by oscillating the tip at 100 kHz and with a tapping amplitude of 30 nm while maintaining a minimum distance of 1 nm between the tip and the sample surface.

Removal of adsorbates: Removal of non-covalently bound adsorbates from the surface of functionalized graphene was achieved by mechanical cleaning using a JPK Nanowizard AFM instrument in contact mode. We used ContAl-G tips (k = 0.2 N m^{-1}) with 4 nN force as setpoint for imaging. To remove adsorbed species, the setpoint was increased up to 60 nN and the sample area was repeatedly scanned until no further change was observed. To avoid damaging graphene, the scans were carried out parallel to graphene edges.

Transport measurements: Transport measurements were performed at low pressure (~10^{-5} mbar) and room temperature inside a Lakeshore TTPX probe station. Both a gate voltage ($|V_g| \leq 80$ V) and drain-source current (I_{ds} = 1 µA) were supplied by individual Keithley 2450 source measure units. The leakage current was negligible for all measurements. The carrier density of graphene at V_g = 0 V is calculated using the gate voltage corresponding to the charge neutrality point in the transport curves. The system is modeled by considering the areal capacitance of the system: $C_{tot} = en/(V_g - V_{CNP})$, where e is the fundamental charge, n is the carrier density, V_g is the gate voltage, V_{CNP} is the charge-neutrality point voltage, and $C_{tot} = (1/C_{geo} + 1/C_{quant})^{-1}$ is the series connection of geometric and quantum areal capacitances. The geometric and quantum areal capacitances are given respectively as $C_{geo} = \varepsilon_0\varepsilon_r/d$ and $C_{quant} = (2e^2)(\hbar v_F)^{-1}(n/\pi)^{1/2}$, where ε_0 is the vacuum permittivity, ε_r = 3.9 is the dielectric constant of SiO_2, d = 300 nm is the thickness of the SiO_2, $\hbar$ is the reduced Planck's constant, and $v_F \approx 10^6$ m/s is the Fermi velocity of graphene near the K/K' point. Fermi level shifts were calculated using areal density of states of graphene using the following formula: $DoS \equiv dn/dE = 2(\hbar v_F)^{-1}(n/\pi)^{1/2}$.

Gold electrodes for transport and KPFM measurements were patterned by electron beam lithography using a Raith Pioneer II or by optical lithography using a Heidelberg Instruments µMLA for direct maskless writing. A thermal evaporator was used to evaporate 3 nm Cr and ~70 nm Au.

X-ray Photoelectron Spectroscopy (XPS): XPS spectra of graphene samples were recorded on SiO_2/Si substrates using a SPECS EnviroESCA (Al Kα,1486.7 eV) under high-vacuum conditions (< 5 x 10^{-5} mbar). Survey spectra (50-700 eV) were measured using an analyzer pass energy of 100 eV, while high resolution spectra (e.g. C 1s, I 3d and Br 3d) were recorded using 15 eV pass energy in a suitable binding energy range.

All XPS spectra were processed with the UNIFIT software. A Shirley background was subtracted from the high resolution spectra and pseudo-Vogt peak shape model (Gaussian:Lorentzian; 50:50) was used to fit the individual components. An asymmetric pseudo-Vogt line shape (0.14) was used to fit the sp² carbon component (C=C) in the C 1s high-resolution spectrum, according to the literature.[1] The XPS spectra were referenced to the C 1s signal at 284.4 eV.

Preparation of CVD graphene: Graphene was prepared by chemical vapor deposition on copper foil using the envelope method. After annealing of the copper envelope for 1 h (1035 °C, 10 sccm H_2, 5 sccm Ar) a flow of methane (5 sccm) was added to the mixture for 10 min growth time. Then, the sample was rapidly cooled down to rt. Arbitrary pieces of graphene were transferred onto substrates by a wet-transfer method.

Preparation of monolayer tape-exfoliated graphene: High quality samples of graphene were prepared by tape exfoliation using the Scotch tape method and directly transferred onto SiO_2/Si substrates. After transfer, the sample was mildly annealed in vacuum (T = 150 °C, p = 1 x 10^{-3} mbar, t = 2 h) to remove water and residuals stemming from the transfer process.

Preparation of h-BN/G heterostructure: Few-layer h-BN was mechanically exfoliated from bulk h-BN via PDMS and transferred onto a SiO_2/Si wafer. Monolayer graphene was mechanically exfoliated from HOPG via PDMS and transferred onto few-layer h-BN flake. According to the transfer method reported previously, the transfer process was carried out under a microscope equipped with a self-built transfer stage.[2] The thicknesses of the exfoliated h-BN and graphene were determined by optical contrast and Raman spectroscopy. After every transfer step, the sample was mildly annealed in vacuum (T = 150 °C, p = 1 x 10^{-3} mbar, t = 2 h) to remove water and residuals stemming from the transfer process.

Preparation of iodine-doped graphene: Graphene deposited on SiO_2(300 nm)/Si wafers (0.5 x 0.5 cm) was covered with 10 µL of a 20 mM solution of I_2 in methanol. Methanol was evaporated under ambient conditions.

Functionalization experiments: Measurements of Raman spectra and the patterning experiments were performed at 3.03 mW laser power. Initial spectra were measured with an acquisition time of 0.1 s. The light dosage was controlled by the exposure time and the number of accumulations per patterning spot. Typically, between 10 and 30 accumulations of 0.1 s exposure times were used at each spot of the patterned area. Improved results were obtained this way compared to direct exposure for similar times.

For large-area functionalization used for XPS measurements 6.7 mW laser power combined with a 10x objective (NA = 0.25) was used. The sample was scanned in SWIFT mode (0.1 s exposure time, 80 µm step size) to ensure sufficient irradiation of a large sample area.

SUPPORTING INFORMATION

Results and Discussion

Supplementary Note 1: Functionalization on different substrates

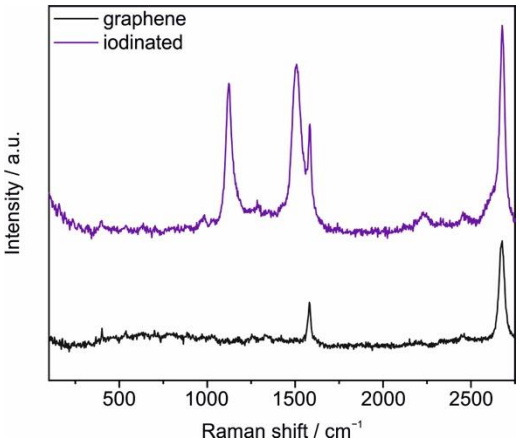

Figure S1. Raman spectra of graphene (black) and iodinated CVD graphene (purple) on a gold-coated (3 nm Cr/ 70 nm Au) SiO_2/Si substrate, demonstrating that the functionalization reaction does not depend on the substrate.

Figure S1 shows Raman spectra of CVD graphene and iodinated graphene on Au substrate with similar characteristics as on SiO_2/Si (e.g. **Figure 2**) and on h-BN on SiO_2/Si (**Figure 3**). In all cases no new signals were observed upon irradiation of the substrate excluding the possibility of iodine-substrate or iodine-adsorbate reactions as the cause of the new Raman modes. Due to the etching effect of iodine on gold small amounts of iodine solution (typically 5 µL were used), however repeated deposition of iodine solution led to the visible degradation of the gold substrate.

Supplementary Note 2: Polyiodide-doped graphene

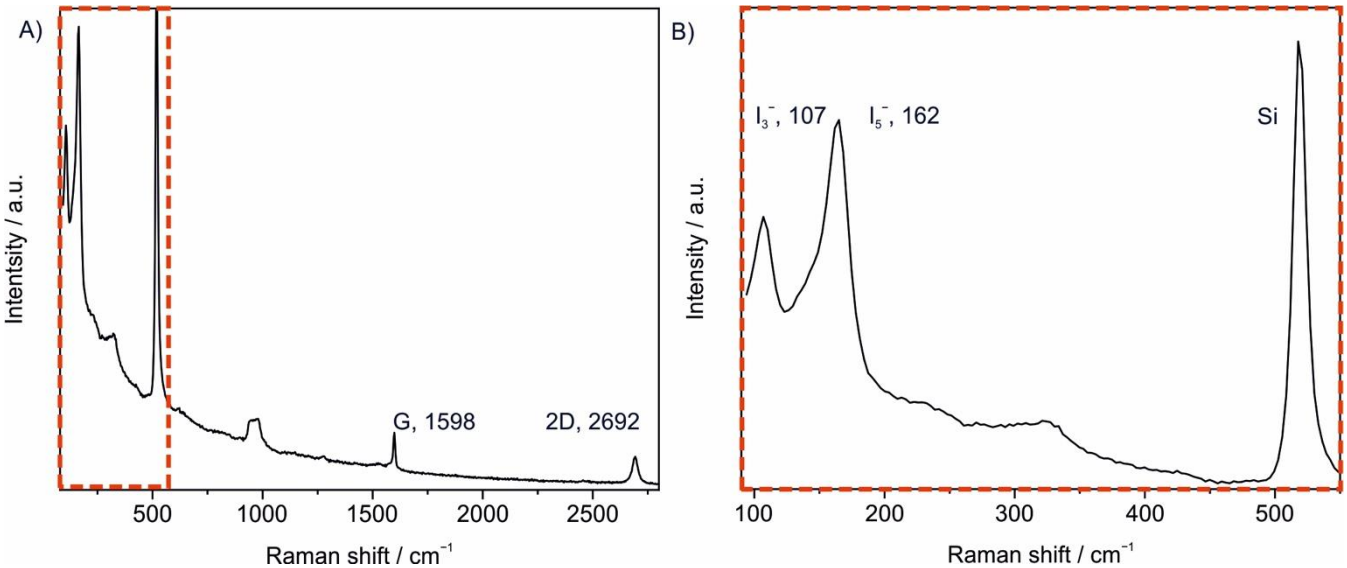

Figure S2. A) Raman spectrum of iodine-doped tape-exfoliated graphene with strong polyiodide signals. B) Zoom of the polyiodide signals. Two distinct peaks are observed corresponding to I_3^- and I_5^- respectively.

Figure S2A shows the spectrum of iodine-doped tape-exfoliated graphene. Polyiodide signals are observed at 107 cm^{-1} and 162 cm^{-1} (**Figure S2B**) consistent with literature values.[3] The G-peak shifts up to 1598 cm^{-1} and a decrease of the G/2D ratio becomes larger than 1 (FWHM(2D) = 27 cm^{-1}). The 2D-peak intensity is partially restored in iodinated graphene and the G-peak shifts back to lower Raman shifts (**Figure S3**). After extended irradiation the polyiodide signals disappear, indicating the evaporation of the adsorbed iodine species.

SUPPORTING INFORMATION

Supplementary Note 3: Discussion of Raman modes and overtones

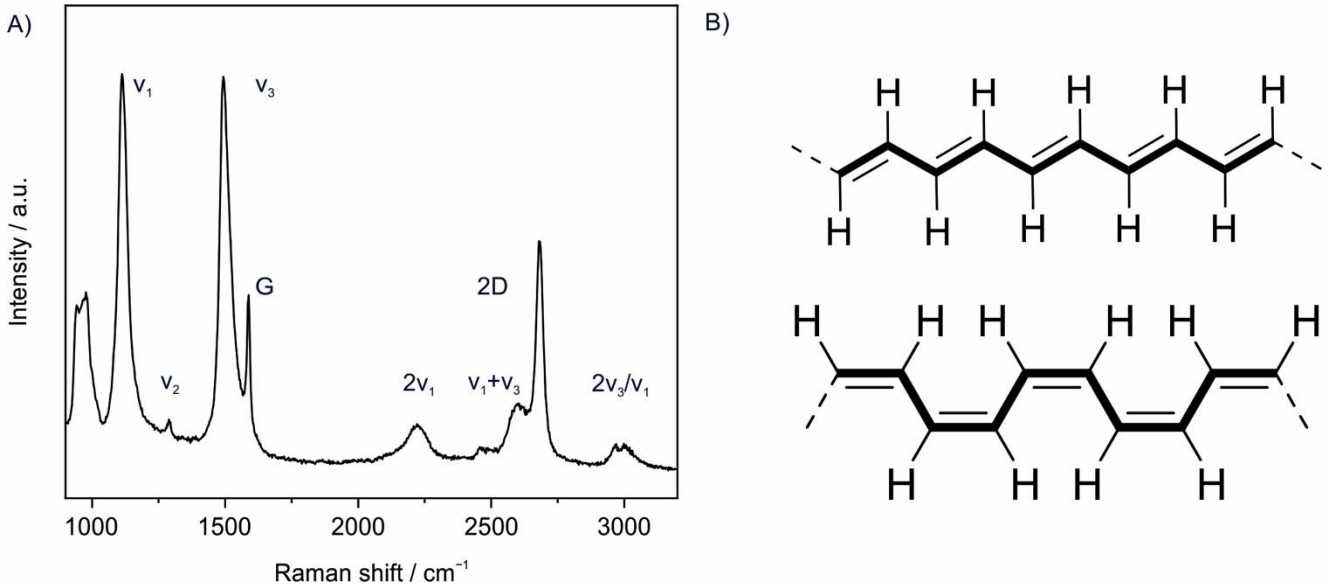

Figure S3. A) Full Raman spectrum of iodinated tape-exfoliated graphene. Three new modes (v_1- v_3) and four overtones are observed. The Raman shifts are given in **Table S1**. B) Chemical structures of thermodynamically more stable *trans*- and less stable *cis*-polyacetylene polymer.

Figure S3a shows the full Raman spectrum of iodinated tape-exfoliated graphene. Two strong new peaks evolve after irradiation at 532 nm at 1115 cm^{-1} (v_1) and 1498 cm^{-1} (v_3), that are stronger than the G- and 2D-peak. A relatively small mode is observed at 1289 cm^{-1} termed v_2. Four overtones are observed: The second harmonic $2v_1$ at 2219 cm^{-1}, the combination mode v_1+v_3 at 2598 cm^{-1} and two broad signals are observed at 2964 cm^{-1} and 3004 cm^{-1} that were assigned to a Fermi resonance between the mode $2v_3/v_1$ in *trans*-polyacetylene.[4] The small v_2 mode was described for *trans*-polyacetylene and appears in varying intensities depending on the chain length.[5] Experimental data of t-butyl group-capped *trans*-oligoenes[6] and DFT calculations[7] show trends in the peak positions of resonant Raman spectra; with increasing chain length, the v_1 and v_3 peaks shifts to smaller Raman shifts and a small v_2 signal is primarily observed at shorter chain lengths. The similarity of these signals and their positions compared to known *trans*-polyacetylene spectra give further evidence for structural similarity of the iodinated graphene (**Table S1**).

Table S1. Characteristic Raman modes of graphene, iodinated graphene and *trans*-polyacetylene (taken from ref.[4]) showing strong similarity to between the observed new modes and *trans*-polyacetylene.

Sample	v_1 / cm^{-1}	v_2 / cm^{-1}	v_3 / cm^{-1}	G / cm^{-1}	$2v_1$ / cm^{-1}	v_1+v_3 / cm^{-1}	2D / cm^{-1}	$2v_3/v_1$[b] / cm^{-1}	
Graphene	-	-	-	1587	-	-	2680	-	-
Iodinated grpahene	1115	1288	1498	1587	2219	2598	2682	2964	3004
trans-polyacetylene[a]	1108	1255	1486	-	2187	2577	-	2954	2994

[a] Measured at 520.8 nm, taken from ref.[4] [b] Fermi resonance

Figure S4A illustrates the difference between Raman and resonance Raman. While virtual states are excited in Raman scattering leading to a relatively low scattering probability (typically in the range of 10^{-6} to 10^{-8}) real states are excited in resonance Raman scattering strongly increasing scattering probability and phonon formation due to the greater perturbation efficiency (typically in the range of 10^{-4} to 10^{-2}). Since graphene has metallic character, excitation with light in a broad range resonantly excites graphene.[8] *Trans*-polyacetylene polymer in contrast is a semiconductor due to the Peierls distortion of the 1D-conjugated double bonds with a chain length-dependent bandgap, varying between 3.1 eV for a *tbu*-capped trans-polyene[6] with 6 double bonds to 1.7 eV measured in the polymer.[5] As mentioned in the main text, while exact energy values may differ in our system where the *trans*-oligoene chains are bonded to carbon atoms of the surrounding graphene instead of hydrogen atoms, similar trends can be expected.

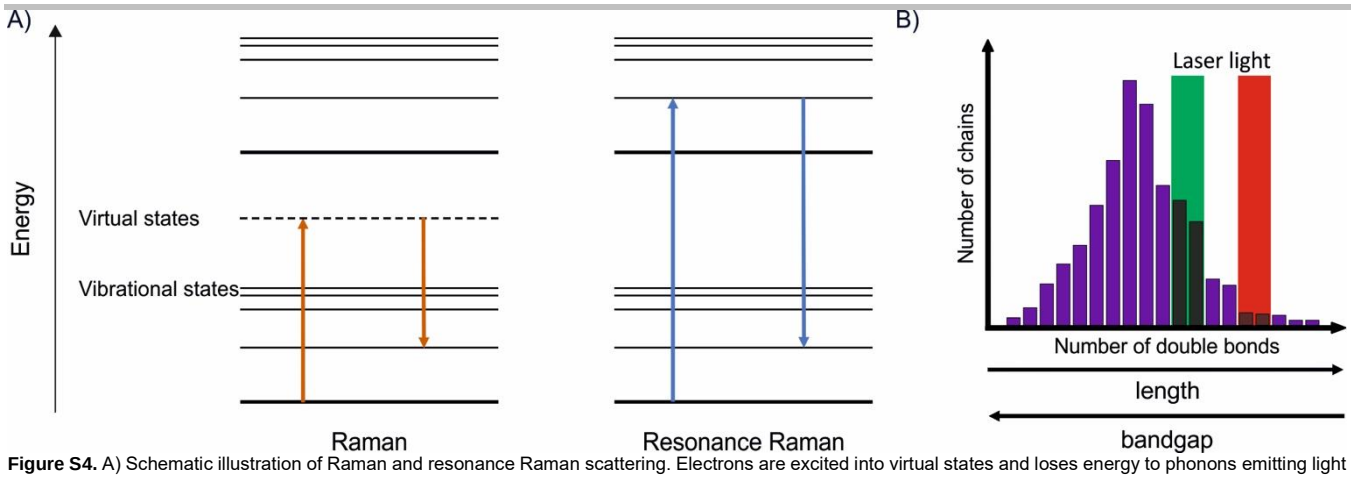

Figure S4. A) Schematic illustration of Raman and resonance Raman scattering. Electrons are excited into virtual states and loses energy to phonons emitting light with lower energy. If an electron is excited into a real excited state, the process is similar, but the signal intensity is strongly increased. B) Schematic illustration showing the influence of resonance Raman excitation on the unknown distribution of *trans*-oligoene chains of the functionalized system. Only a small portion of those exhibits a bandgap close to the probed excitation energy and is therefore probed.

The spectral modes arise from resonant Raman scattering, that is observed when the sample is excited near its electronic resonance energy, leading to a strong increase of the Raman signal. Since the *trans*-oligoene chains in iodinated graphene are of a finite length and can be categorized by their discrete length (given by the number of double bonds) we can visualize the system as an unknown distribution from which the contribution to the Raman signals will originate from *trans*-oligoene chains with a bandgap that is close to the laser energy (**Figure S4B**). By varying the excitation energy, the resonance energy and thereby the chain length that is excited, changes. By decreasing the excitation energy longer *trans*-oligoene chains are resonantly excited, but still only a portion of the complete distribution is observed.[9] Therefore, it is not possible to characterize the complete distribution by measurement at a single wavelength. The resulting Raman modes are a sum of the resonantly excited trans-oligoene chains at the given laser wavelength, explaining the varying peak intensities and positions observed for various samples and after either heat treatment or irradiation with 405 nm laser light (**Figure S5A**).

Supplementary Note 4: Defunctionalization after irradiation at 405 nm and evidence for shift of unknown *trans*-oligoene chain distribution

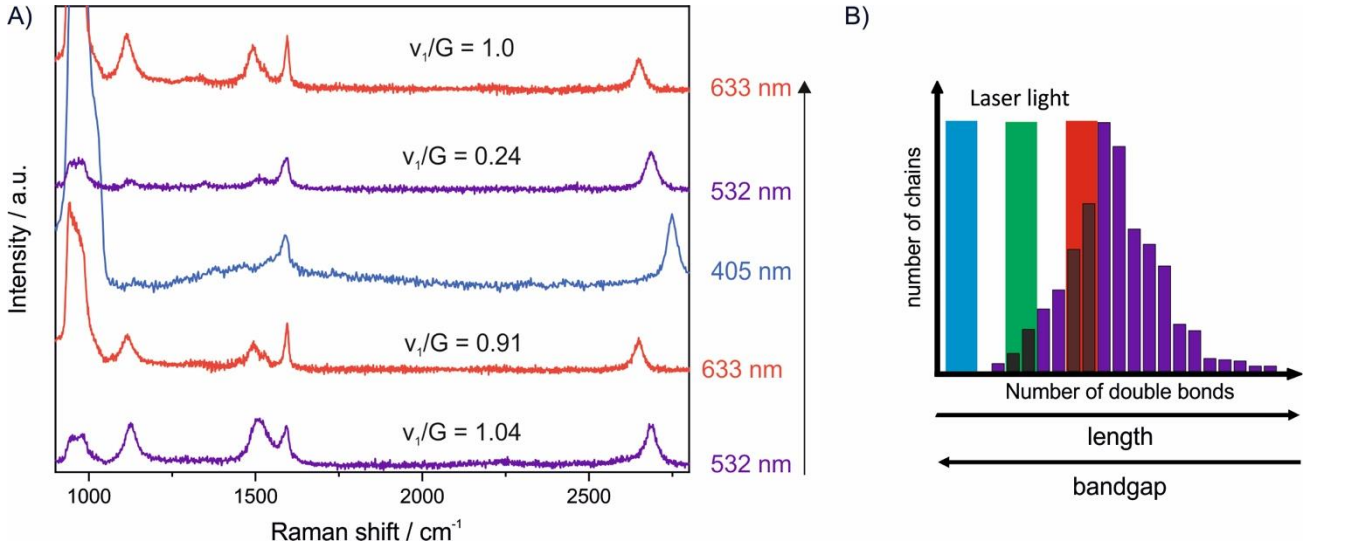

Figure S5. A) Raman spectrum of iodinated tape-exfoliated graphene (purple) and the same spot measured at 633 nm (red), before and after irradiation with 405 nm laser light (blue, 5 s irradiation time). No *trans*-oligoene signals are observed at 405 nm but the intensity of *trans*-oligoene signals at 532 nm is significantly decreased after irradiation. Signals at 633 nm increase, indicating a shift of distribution by high energy laser light. B) Schematic illustration of the shifted distribution after irradiation at 405 nm. Irradiation causes defunctionalisation shifting the distribution to longer chain lengths.

Figure S5A shows a series of Raman spectra of tape-exfoliated graphene taken before and after excitation with 405 nm (3.06 eV) laser light. Before irradiation the v_1 and v_3 modes at 532 nm ($v_1/G = 1.04$) are larger relative to the G-peak compared to the modes at 633 nm ($v_1/G = 0.91$). At 405 nm only graphene signals are observed, indicating no *trans*-oligoene chains with a matching bandgap. After irradiation with 405 nm the signal intensities at 532 nm decrease ($v_1/G = 0.24$) and increase at 633 nm ($v_1/G = 1.0$), consistent with a change of chain distribution due to partial removal of sp^3-defects leading to longer *trans*-oligoene chains with smaller bandgaps between the remaining defects, as shown schematically in **Figure S5B**. While the hypothetical chain distribution shown only shifts to longer

chain lengths in comparison to **Figure S4B**, in a real system the partial removal functionalization will also decrease the total number of chains.

Supplementary Note 5: Thermal iodination of graphene

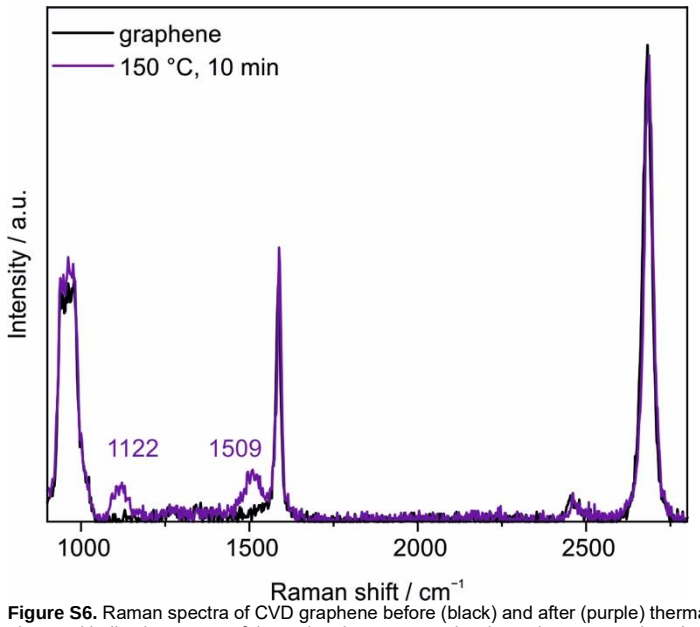

Figure S6. Raman spectra of CVD graphene before (black) and after (purple) thermal iodination in ambient conditions (150 °C, 10 min). Small ν_1 and ν_3 modes are observed indicating successful reaction, however at a low intensity compared to photochemical reaction.

Figure S6 shows Raman spectra of iodine-doped CVD graphene before and after thermal treatment (150 °C, 10 min). Iodine in methanol solution was deposited on graphene on SiO_2/Si wafer. After complete evaporation of the solution the sample was placed on a hot plate at ambient conditions. Despite the considerable vapor pressure of iodine new Raman signals were found while no D-peak was introduced in the process and the G- and 2D-peak remain almost unchanged. Due to the weak iodine-iodine bond homolytic dissociation can already occur at relatively low energies. While this approach only yields small *trans*-oligoene modes compared to the photochemical functionalization it may be interesting for wafer-scale functionalization of large graphene films.

SUPPORTING INFORMATION

Supplementary Note 6: XPS characterization of iodinated graphene

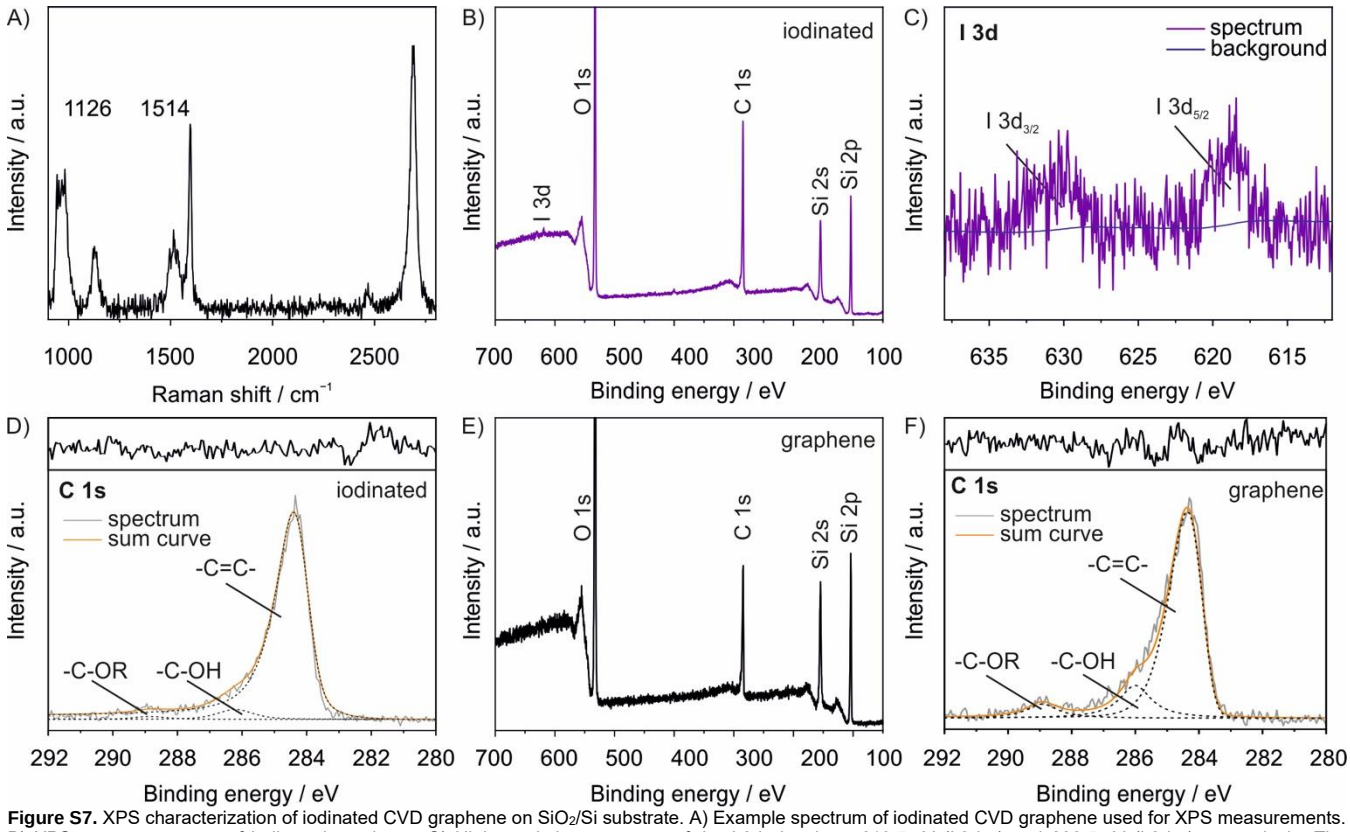

Figure S7. XPS characterization of iodinated CVD graphene on SiO_2/Si substrate. A) Example spectrum of iodinated CVD graphene used for XPS measurements. B) XPS survey spectrum of iodinated graphene. C) High-resolution spectrum of the I 3d signals at 619.5 eV (I $3d_{5/2}$) and 630.5 eV (I $3d_{3/2}$) respectively. The characteristic signals can be clearly distinguished from the noise. D) High-resolution C 1s spectrum of iodinated graphene. The inset shows the residual of the fits. E) Survey spectrum of pristine CVD graphene. F) High-resolution C 1s spectrum of pristine CVD graphene. The inset shows the residual of the fits.

Figure S7A shows a representative Raman spectrum of CVD graphene after functionalization with iodine. Since the tape-exfoliated graphene layers are too small for XPS measurements (spot size ~300 µm), large-area CVD graphene was functionalized photochemically on a large scale using modified conditions (10x, 6.7 mW, SWIFT mode, 0.1 s, 20 µm step size). Prior to the measurements the samples were thoroughly cleaned by complete evaporation of the reaction mixture followed by washing with water, isopropanol and acetone.

The survey XPS spectrum of iodinated graphene (**Figure S7B**) shows two small signals at 619.5 eV (I $3d_{5/2}$) and at 630.5 eV (I $3d_{3/2}$) for iodine.[3] The intensity of these signals is at the resolution limit (**Figure S9C**) but can be clearly distinguished from the noise of the background.

The deconvolution of the C 1s peak (**Figure S9D**) does not show a new component for C-I bonds due to the low concentration if Iodine bound to the graphene and the low difference in electronegativity, responsible for a weak chemical shift. For carbon-iodine bonds a signal at 286.3 eV or less would be expected – the same position as carbon-oxygen single bonds.[3]

Supplementary Note 7: *Trans*-Oligoene chain formation induced by bromine and characterization by Raman and XPS

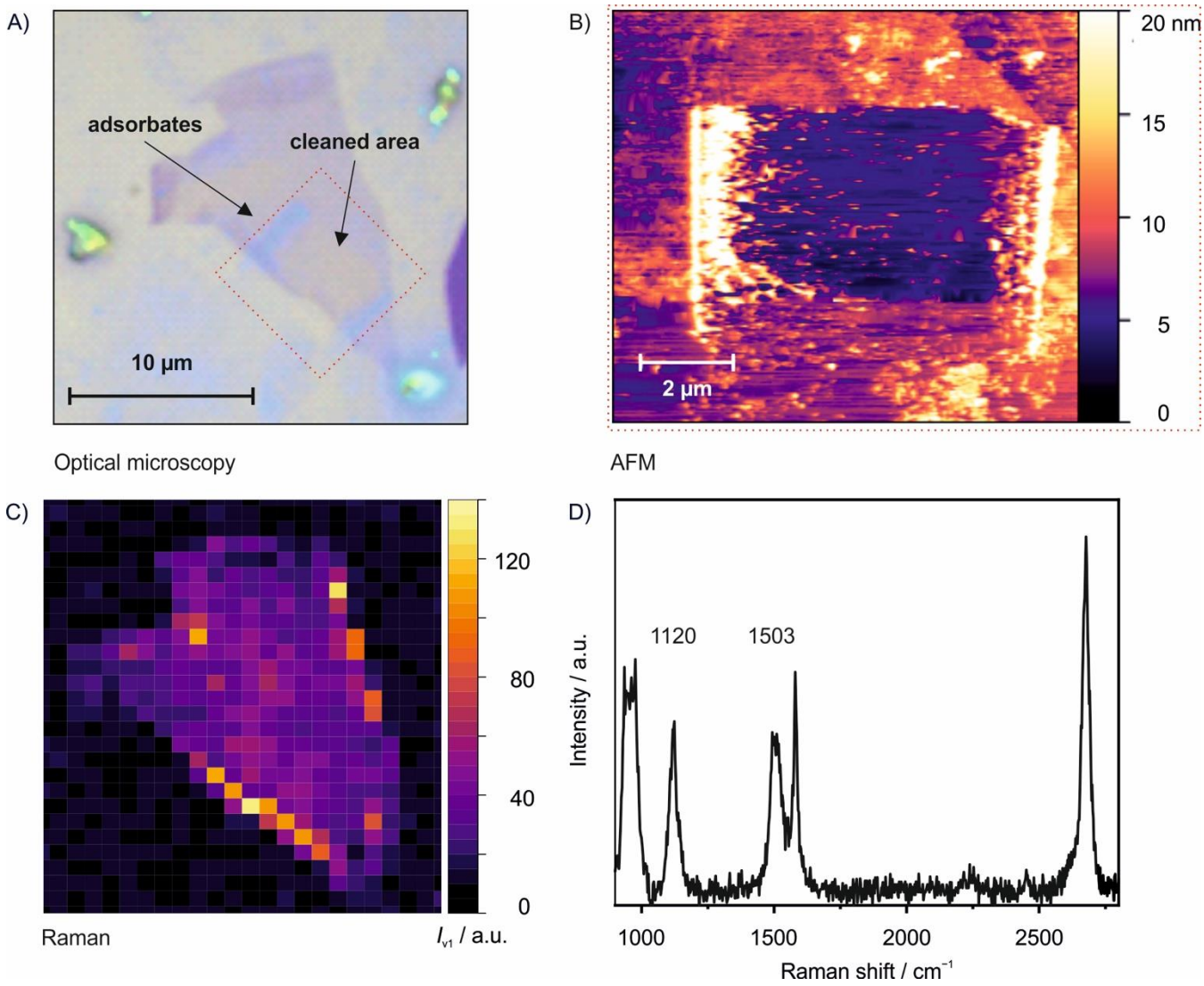

Figure S8. Photochemical bromination of tape-exfoliated graphene. A) Optical microscopy image showing graphene flake after mechanical cleaning of 7x7 µm area. The cleaned area is bordered by the piled adsorbates moved to the sides. B) AFM image of the area marked by the red square in A showing the mechanically cleaned area. C) Raman map showing the intensity of the v_1 peak. No difference is observed in the cleaned and uncleaned areas. The piled adsorbates do not give a measurable Raman signal. Each pixel has an area of 0.7x0.7 µm. A preferred reactivity of bromine at the edges of the graphene flake can be observed. D) Raman spectrum of the strongest signal observed in the cleaned area at the edge of the graphene flake.

Figure S8A shows a microscopy image of tape-exfoliated graphene after photochemical functionalization with bromine and subsequent mechanical cleaning of a 7x7 µm area with an AFM tip (**Figure S8B**). The sample was brought in contact with bromine vapor for 30 s followed by laser irradiation (3.03 mW, 0.1 s, 10 accumulations). The v_1 and v_3 mode emerge, similar to iodinated graphene (**Figure S8D)** however at lower intensities. To the best of our knowledge this is the first report of such Raman signals in brominated graphene. Notably, a strong difference between the edges and the plane is observed, as apparent from the Raman map (**Figure S8C**) that could be due to the increased reactivity of graphene at the edges.

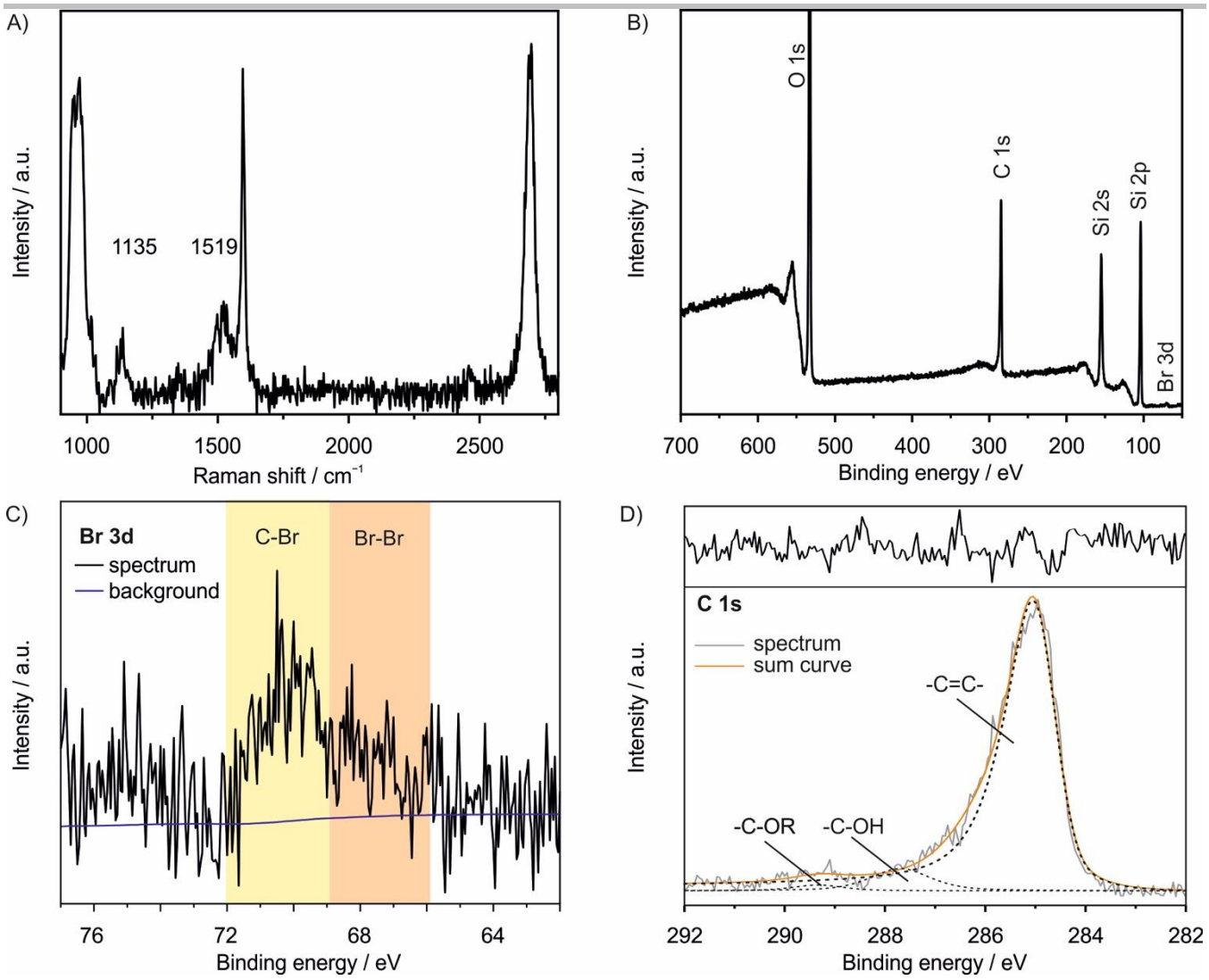

Figure S9. XPS characterization of thermally brominated CVD graphene on SiO_2/Si substrate. A) Raman spectrum of CVD graphene after thermal bromination (150 °C, 10 min). B) Survey spectrum of brominated graphene revealing a small Br 3d signal around 70 eV binding energy. C) High-resolution spectrum of the Br 3d signal showing a broad signal around 70 eV. The shaded area in brown indicates the location of adsorbed Br-Br species, while the yellow shaded area indicates the expected location of covalent C-Br signal.[10] D) High-resolution spectrum of the C 1s signal. No significant change compared to the pristine graphene (**Figure S7F**) can be observed. The inset shows the residual of the fits.

Figure S9A shows a Raman spectrum of CVD graphene after thermal functionalization with bromine (150 °C, 10 min) used for XPS measurements. The v_1 and v_3 signals indicate the successful functionalization of the sample. The XPS survey spectrum of thermally brominated graphene (**Figure S9B**) shows a small signal around 70 eV from Br 3d electrons that is persistent after thorough washing and extended times under the high-vacuum conditions inside the XPS instrument, while other characteristic bromine signals with lower relative sensitivity factors, e.g. Br 3p at ~185 eV cannot be observed.[10] The intensity of the signal is at the limit of detectability, but high-resolution measurement of the Br 3d signal reveals two distinguishable components (**Figure S9C**) that have been assigned to Br-Br adsorbed to graphene (68.5 eV) and carbon-bromine (70.2 eV).[10]
The deconvolution of the C 1s peak (**Figure S9D**) does not show a measurable alteration of the material compared to the starting material (**Figure S7F**). For carbon-bromine bonds a signal at 286.5 eV together with C-O signals would be expected.[10]
A reliable quantification of the signal areas cannot be made due to the low signal intensity, but the bromine content must be below 1 %.

SUPPORTING INFORMATION

Supplementary Note 8: Transport measurements of pristine and iodinated graphene

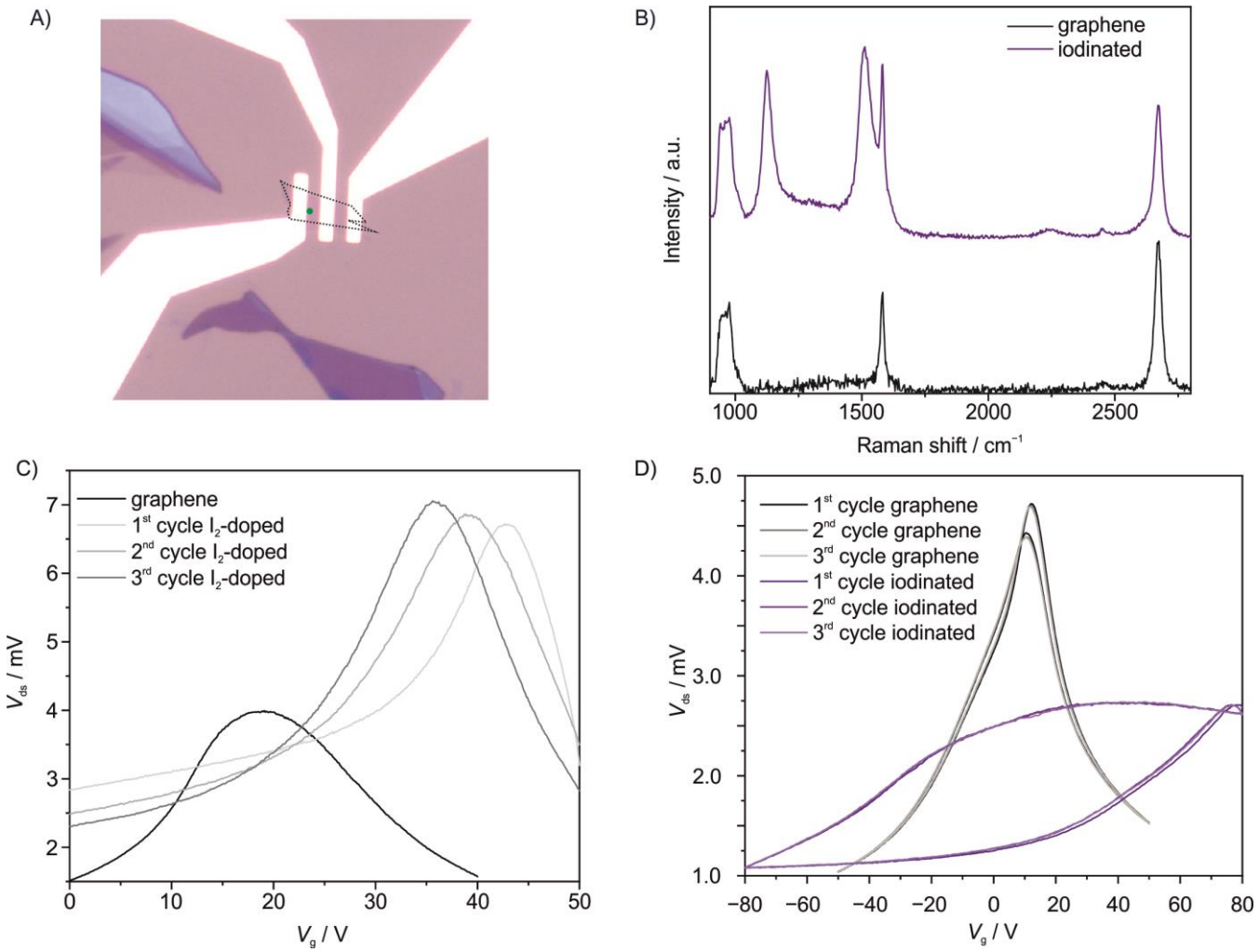

Figure S10. A) Optical image (100x) of the transistor with the tape-exfoliated flake area outlined. The green dot shows where Raman measurements were performed. B) Raman spectra from the flake before (black) and after (purple) iodination C) Drain-source voltage vs. gate voltage of pristine graphene (black) and polyiodide-doped graphene (colour gradient). Iodine causes hole doping in graphene by charge-transfer complex formation forming polyiodides. As we sweep the gate 3 times consecutively (~30 min total), the iodine evaporates over time, causing the initial doping of the graphene to tend toward its pristine value. D) Reproduction of **Figure 4A** from the main text showing all forward and backward sweeps of the data taken showing reproducibility of the data over time.

Figure S10A shows a microscopy image of the transistor device where the tape-exfoliated graphene flake area is outlined by the dotted lines. The green dot marks where the spectra in **Figure S10B** were taken before and after iodination. After fabrication and measurement of the pristine device iodine in methanol solution was deposited on the wafer (10 µL, 20 mM) and after complete evaporation of the solvent the sample was irradiated several times to ensure complete functionalization of the device area. V_{CNP} of graphene doped with iodine did not exceed 50 V and significant decrease of doping was already observed within the measurement time of around 30 min at ambient conditions (**Figure S10C**). Three cycles were measured of graphene before and after iodination to verify the reproducibility of the observed curves. **Figure S10D** shows all three cycles of the measurements shown in **Figure 4A** highlighting the reproducibility of the observed features.

Supplementary Note 9: Mechanical cleaning of patterned CVD graphene

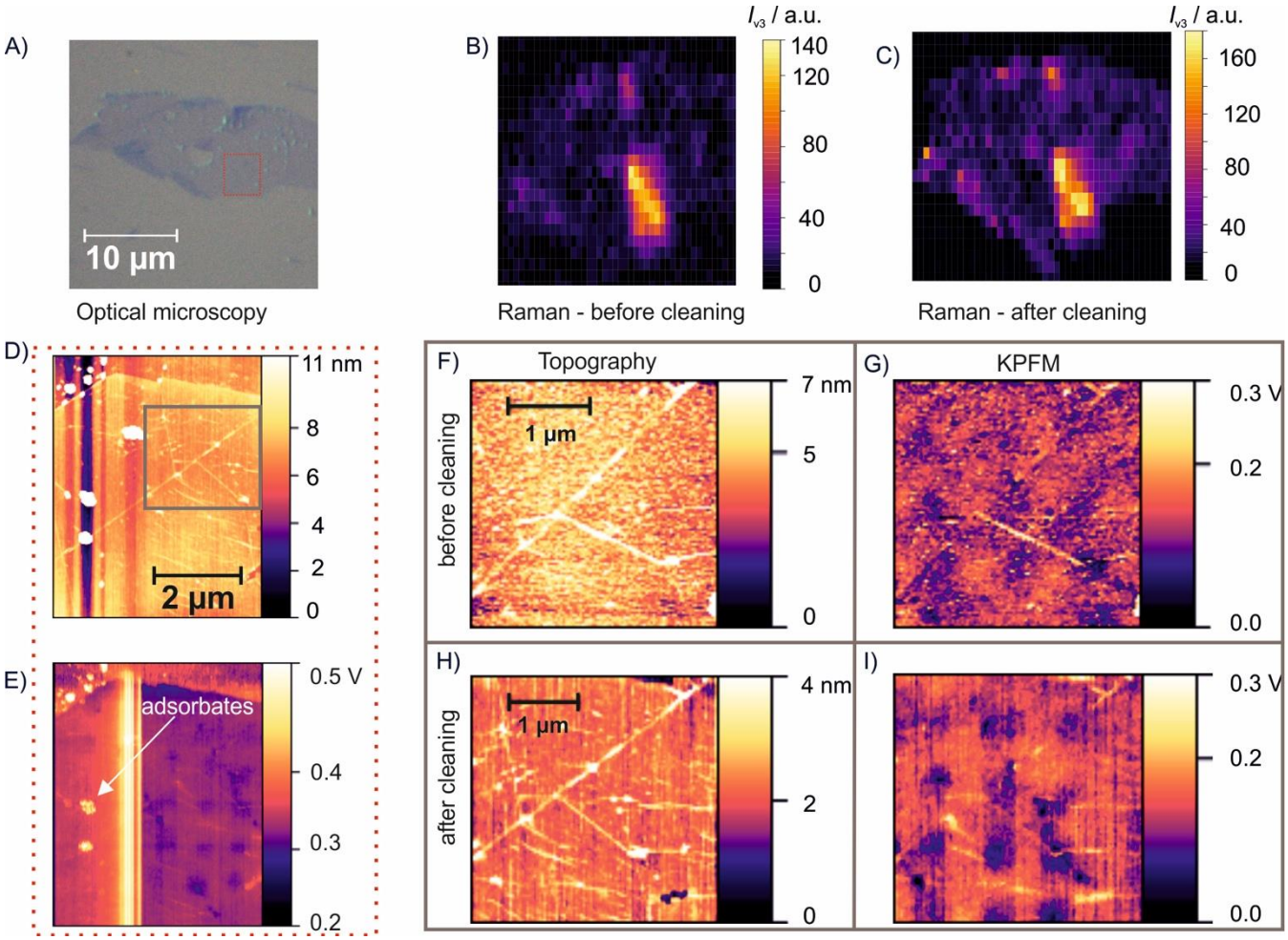

Figure S11. Mechanical cleaning of iodinated CVD graphene. A) Microscopy image showing graphene flake. The cleaned area is marked in red. B) Raman map of patterned area showing the v_3 mode before and C) after mechanical cleaning. The range was chosen so that a small portion of the G peak is included so that the outline of the graphene flake is visible and one pixel has a dimension of 0.7 x 0.7 µm . D) AFM image of mechanically cleaned area. The inset shows the area shown in F-I. E) KPFM image of the patterned area after mechanical cleaning. The highlighted adsorbates show a larger work function compared to graphene, contrary to the patterned areas. F) AFM image before mechanical cleaning. G) KPFM image before mechanical cleaning. H) AFM image after mechanical cleaning showing increased contrast due to removal of adsorbates. I) KPFM image after mechanical cleaning showing increased contrast between graphene and patterned areas due to removal

Figure S11A shows a microscopy image of the CVD graphene sample shown in **Figure 4C and D**. The Raman maps of the v_3 mode show no change of the signal intensity or location after mechanical cleaning (**Figure S11B and C**). The patterned area topography image (**Figure S11D and H**) reveals new features such as folds of the graphene sheet but no patterns that are visible in the KPFM image (**Figure S11E**). No change of the KPFM signal position can be observed in the patterned regions. The removed adsorbates show a large work function contrary to the patterns observed (**Figure S11E**). The contrast between the functionalized pattern and the surrounding graphene is increased by the removal of the adsorbates (**Figure S11G and I**).

SUPPORTING INFORMATION

Supplementary Note 10: KPFM measurements of contacted sample to ensure grounding for reliable data extraction

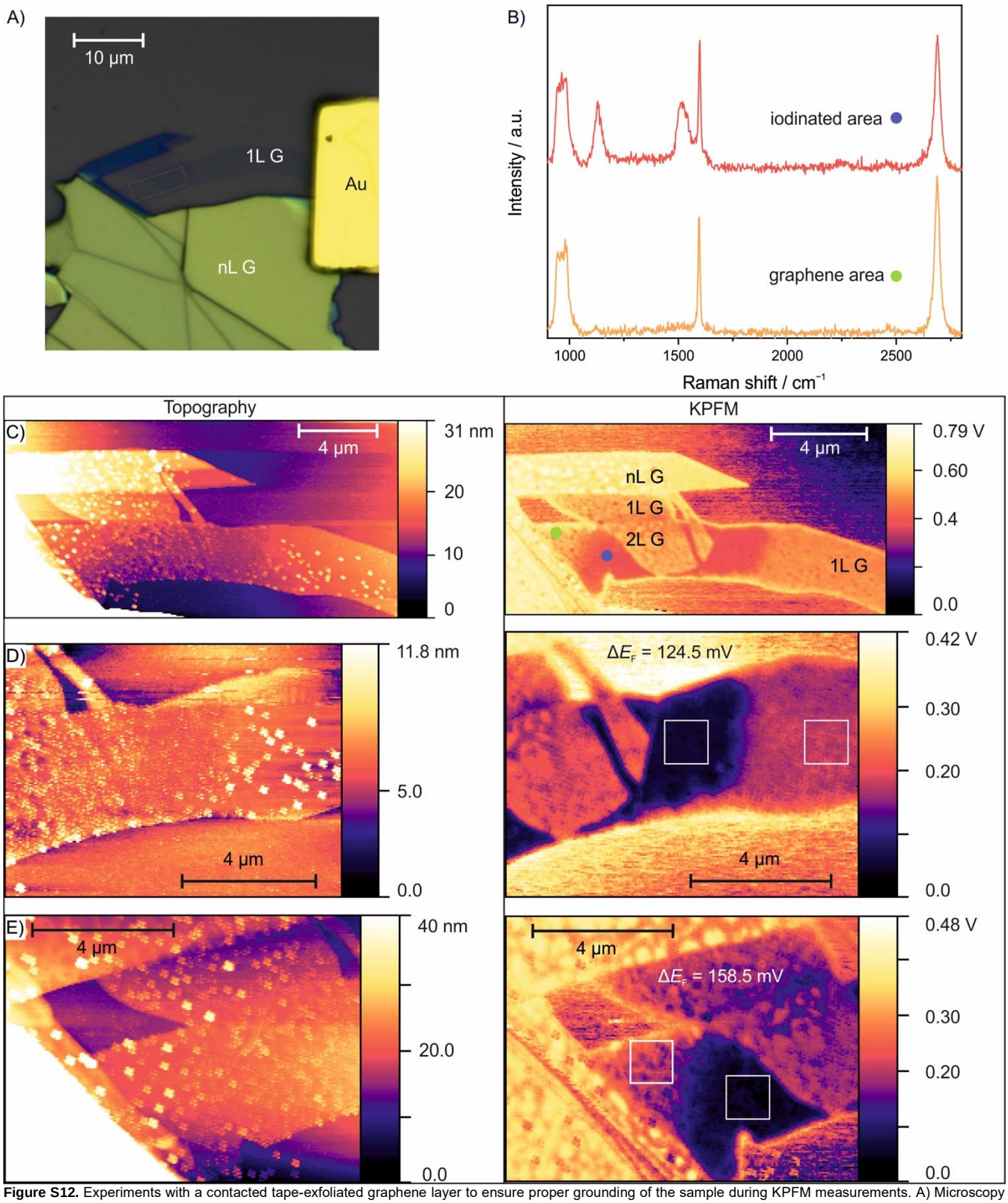

Figure S12. Experiments with a contacted tape-exfoliated graphene layer to ensure proper grounding of the sample during KPFM measurements. A) Microscopy image (100x) showing the monolayer graphene strip contacted by a gold electrode. The marked area corresponds to the irradiated area. B) Raman spectra of the areas indicated by the coloured dots (green and blue) in the KPFM image of **Figure S7C**. C) Overview image of the iodinated area. C) Overview topography (left) and KPFM (right) image of the iodinated area. D) Zoom on the iodinated area right of the bilayer. The white boxes mark areas from which ΔE_F was calculated given in black. E) Zoom on the iodinated area left of the bilayer. The white boxes mark areas from which ΔE_F was calculated given in white.

To quantify the work function measured by KPFM proper grounding of the sample must be ensured. Therefore, a tape-exfoliated graphene flake was contacted with a gold electrode to ensure electrical grounding (**Figure S12A**). An area of 8x3 µm was repeatedly

irradiated (step size = 0.5 µm, λ_{exc} = 532 nm, 0.1 s, 30 accumulations, 8 times, 3.03 mW, **Figure S12B**) and remaining iodine was evaporated (T = rt, p = 1 x 10^{-3} mbar, t = 2 h). The sample was contacted by applying conductive silver paint to the gold electrode. The measurements were performed under ambient conditions. Regular, flower-like structures can be observed on the surface of graphene that may be iodine/polyiodide crystals that have not completely evaporated. These structures show a reduction of the work function, however smaller compared to the iodinated areas, which is in line with the transport measurements showing stronger p-doping for the iodinated graphene compared to iodine-doped graphene (**Figure S2**). The height of the flake compared to the substrate is 4 nm indicating the coverage of graphene with adsorbates, e.g. remaining iodine. Less structures are observed in the iodinated areas, maybe due to the increased evaporation by laser irradiation, giving a contrast in the topography image. Nevertheless, the measured work function is lower in irradiated areas consistent with the increased doping level of iodinated graphene compared to iodine-doped graphene in transport measurements.

Table S2. Extracted contact potential difference values from contacted KPFM measurement each from a 25x25 pixel square.

Sample	iodinated / mV	pristine / mV	ΔE_F / mV
Right of bilayer (**Figure S8D**)	50.56 ±4.62	175.1 ±6.45	124.5
Left of bilayer (**Figure S8E**)	46.56 ±8.35	205.1 ±24.4	158.5
Average	48.56 ±6.48	190.1 ±15.4	141.5

To extract the work function differences an average of 25x25 pixels in the pristine areas were compared to the same number of pixels in the iodinated area (white squares, **Figure S12D** and **E**) in two different areas of the sample and averaged, giving a value of 141.5 mV (**Table S2**).

References

[1] A. Kovtun, D. Jones, S. Dell'Elce, E. Treossi, A. Liscio, V. Palermo, *Carbon* **2019**, *143*, 268.
[2] M. Hussmann, B. Weintrub, P. Feicht, G. Germer, J. N. Kirchhof, K. I. Bolotin, S. Eigler, *Nanoscale Adv.* **2020**, *2*, 176.
[3] P. Šimek, K. Klímová, D. Sedmidubský, O. Jankovský, M. Pumera, Z. Sofer, *Nanoscale* **2015**, *7*, 261.
[4] V. Rives-Arnau, N. Sheppard, *J. Chem. Soc., Faraday Trans. 1* **1980**, *76*.
[5] E. Ehrenfreund, Z. Vardeny, O. Brafman, B. Horovitz, *Phys. Rev. B* **1987**, *36*, 1535.
[6] H. E. Schaffer, R. R. Chance, R. J. Silbey, K. Knoll, R. R. Schrock, *J. Chem. Phys.* **1991**, *94*, 4161.
[7] K. Furuya, A. Sakamoto, M. Tasumi, *J. Phys. Chem. A* **2023**, *127*, 5344.
[8] P. Klar, E. Lidorikis, A. Eckmann, I. A. Verzhbitskiy, A. C. Ferrari, C. Casiraghi, *Phys. Rev. B* **2013**, *87*.
[9] H. Kuzmany, *Macromol. Symp.* **1990**, *37*, 81.
[10] O. Jankovsky, P. Simek, K. Klimova, D. Sedmidubsky, S. Matejkova, M. Pumera, Z. Sofer, *Nanoscale* **2014**, *6*, 6065.

Author Contributions

Fabian Grote: Conceptualization, data curation, investigation, visualization, writing – original draft. **Benjamin I. Weintrub:** Investigation, transport measurements, writing – review and editing. **Mira Kreßler:** Investigation, KPFM measurements. **Qing Cao:** Sample preparation. **Christian E. Halbig:** Investigation, XPS measurements. **Patryk Kusch:** Supervision, validation, funding acquisition. **Kiril I. Bolotin:** Supervision, validation, funding acquisition. **Siegfried Eigler:** Supervision, validation, funding acquisition, methodology, project administration, resources, writing – review and editing.

6.2 Influence of Lattice Defects on *Trans*-Oligoene Substructure Formation in Graphene

Authors	F. Grote, S. Eigler
Journal	*Chem. Eur. J.* **2024**, e2024010331.
DOI	10.1002/chem.202401031
Links	https://doi.org/10.1002/chem.202401031
Detailed scientific contribution	The concept of this manuscript was elaborated by F. Grote and S. Eigler. Sample fabrication and functionalization was done by F. Grote. Raman characterization and data analysis was done by F. Grote. S. Eigler supervised the experimental work. The manuscript was written by F. Grote with assistance from S. Eigler.
Estimated own contribution	~90%

Chemistry–A European Journal
Research Article
doi.org/10.1002/chem.202401031
Chemistry Europe
European Chemical Societies Publishing
www.chemeurj.org

Influence of Lattice Defects on *Trans*-Oligoene Substructure Formation in Graphene

Fabian Grote[a] and Siegfried Eigler*[a]

The photochemical reaction of iodine and graphene induces strong new Raman modes due to the formation of *trans*-oligoene substructures in graphene domains. This unique reactivity was demonstrated before on defect-free graphene, however leaving the influence of e.g. carbon vacancies, unexplored. Here, we investigate the photochemical reaction applied on graphene with varying average distances of lattice defects and statistically analyze the characteristic Raman modes which develop with the iodination reaction. We show that the iodination reaction does not lead to Raman-active defects and thus, the newly formed *trans*-oligoene substructures do not contribute to the D-mode of graphene. A statistical analysis reveals the correlation between the average distance of lattice defects and the intensity of the v_1-mode. For defective graphene with average defect distances below ~1 nm no new Raman modes evolve, which is the lower limit of the substructure size probed at 532 nm and explains why this observation was not possible before using common graphene oxide as graphene source.

Introduction

The regioselective functionalization of graphene modifies its electronic structure by periodic variations on the nanometer scale within the graphene lattice.[1] To date, examples of reactions generating defined substructures within the material are rare due to a lack of functionalization strategies with strong regioselectivity.[2] Moiré superlattices of graphene and its metal substrate have been used to guide the reactivity in periodical patterns.[3] Similar to the patterning on the microscopic scale, masks of supramolecular assemblies can be used to introduce periodic structures.[4]

In our recent report, the evolution of *trans*-oligoene substructures induced by a photochemical iodination reaction applied on defect-free graphene was observed.[5] However, previous reports using defective graphene, e.g. reduced graphene oxide did not display specific Raman modes, that would suggest a reaction with iodine.[6] Thus, the substructure formation seems to be strongly influenced and limited by the presence of lattice defects. Generally, lattice defects strongly influence the electronic properties and determine the Raman scattering properties of graphene.[7] Accordingly, vacancy defects can activate surrounding unsaturated carbon bonds and thus guide the reactivity of radical addition reactions, a process, which can be followed by Raman spectroscopy.[8] Consequently, the introduced functional groups majorly accumulate around defect sites, while large areas between them remain graphene-like. In addition, lattice defects act as scattering sites for phonons and therefore activate the D-peak in Raman spectra, which is used to quantify the distance of defects.[9] Statistical Raman spectroscopy can be used to assess the quality of graphene[10] and follow functionalization reactions with μm-scale spatial resolution.[11] A precise relation between the Raman modes and the distance of defects was developed by Lucchese and Cançado[9a] (Equation 1, Table S2) that empirically describes the relation of the ratio between the intensity of the D-mode (I_D) and the G-mode (I_G) and the average distance of defects in graphene.

$$\frac{I_D}{I_G} = C_A \frac{\left(r_A^2 - r_S^2\right)}{\left(r_A^2 - 2r_S^2\right)} \left[e^{-\frac{\pi r_S^2}{L_D^2}} - e^{-\frac{\pi\left(r_A^2 - r_S^2\right)}{L_D^2}} \right] \quad (1)$$

Here, L_D is the distance of defects in nm, C_A is an empirically derived parameter that depends on the laser energy used (2.33 eV, 532 nm in this work). The radius of the activated area (r_A) and the radius of the structurally disordered region (r_S) describe the contributions of these areas around the defects. This model was derived for graphene bombarded with Ar^+ ions and its applicability was also shown for other defective graphene materials proving its general applicability.[10b,12]

Since *trans*-oligoene modes can be generated in defect-free graphene, but are not yet reported in reduced graphene oxide, statistical correlations between the *trans*-oligoene Raman modes, see Figure 1, and the distance of lattice defects may provide structural information of the novel substructures. Thus, we studied the extend of *trans*-oligoene substructure formation induced by the iodination reaction of different graphene samples with L_D-values ranging from no detectable defects down to below 1 nm. We show that the characteristic Raman modes emerge in defective graphene under similar reaction conditions reported for defect-free graphene. We further show

[a] M.Sc. F. Grote, Prof. Dr. S. Eigler
Institut für Chemie und Biochemie
Freie Universität Berlin
Altensteinstraße 23a, 14195 Berlin, Germany
E-mail: siegfried.eigler@fu-berlin.de

Supporting information for this article is available on the WWW under https://doi.org/10.1002/chem.202401031

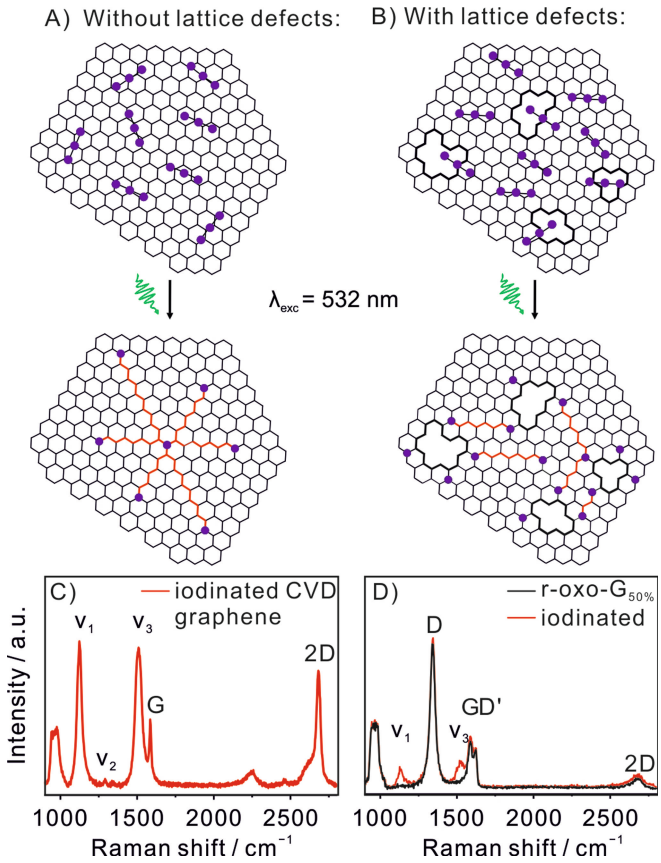

Figure 1. Schematic illustration of the functionalization process: Graphene is doped with polyiodides (purple) and is subsequently irradiated by laser light (λ_{exc} = 532 nm) to generate iodine radicals that induce *trans*-oligoene substructures (red). A) In graphene without defects the length of the substructures is only limited by the delocalization of the π-radical. B) Radical addition reactions occur around defects that also limit the length of the substructures. C) Raman spectrum of iodinated CVD graphene without defects. Strong v_1 and v_3-modes emerge and the v_2-mode can be observed but no D-mode. D) Raman spectra of r-oxo-$G_{50\%}$ with L_D ~2 nm before (black) and after (red) iodination reaction. The v_1 and v_3 modes form while no significant change of the graphene modes is observed.

that no Raman-active defects are introduced by the reaction and hence the formation of *trans*-oligoene substructures can be followed. With Statistical Raman spectroscopy (SRS) we reveal a correlation between the distance of defects and the intensity of the *trans*-oligoene Raman modes. The characteristic modes do not appear at defect distances below about 1 nm, which therefore is the lower limit of *trans*-oligoene substructure length probed under the given conditions.

Results and Discussion

To investigate the influence of lattice defects on *trans*-oligoene chain formation, we iodinated different graphene derivatives on 300 nm SiO_2/Si substrate with various distances of lattice defects. Graphene with a heterogenous quality was prepared by chemical vapor deposition (CVD) that cover the full range of defects in the Raman-sensitive range. Furthermore, we wet-chemically prepared oxo-graphene with defined distances of defects depending on the oxidation conditions. Purified oxo-graphene was transferred onto SiO_2/Si substrate by drop-casting and reduced with hot vapors of hydrogen iodide and trifluoroacetic acid, as reported earlier.[13] Depending on the oxo-functionalized graphene derivative, two kinds of graphene were prepared. The graphene derivative r-oxo-$G_{50\%}$ (the subscript indicates the degree of functionalization of oxo-graphene before reduction and the prefix "r" indicates that it was reduced to yield graphene) with I_D/I_G = 2.6 relates to L_D ~2 nm, (Figure S1A) and r-oxo-$G_{4\%}$ with I_D/I_G = 3.1 relates to L_D ~6 nm (Figure S1B), according to Equation 1. The atomic structures of those materials have been visualized by ac-TEM before.[14] A methanolic iodine solution (20 mM, 10 μL) was deposited onto the sample for the photochemical reaction and after complete evaporation of the solvent the sample was irradiated by the Raman laser (532 nm, 0.1 s irradiation time, 10 accumulations, Figure 1A and B). To exclude laser induced side reactions the experiments were tested without iodine as well, but no significant changes were observed.

Further on, we investigated whether Raman-active defects are introduced by the iodination reaction. No D-peak formation was observed for graphene without defects, as depicted in Figure 1C. Next, we used reduced oxo-graphene with an average defect distance of about 2 nm, for which Raman spectroscopy is most sensitive on changes in the distance of defects by monitoring the I_D/I_G ratio (Figure 1D). Despite the significant density of defects, v_1 and v_3 modes emerge in the Raman spectra, however with a ~10 times decreased intensity compared to defect-free graphene. Interestingly, the I_D/I_G ratio did not change within the limits of the reference experiment (Table S1) showing that any defects introduced by the iodination reaction must be either Raman silent or below the detection limit.

The covalent addition of substituents without significant D-mode introduction in graphene has been reported earlier, e.g. for chlorination and azidation reactions.[15] It has also been reported for the addition of nitrenes on carbon nanotubes, where re-aromatization after the addition reaction is proposed as explanation.[16] We expect that for halogen reactions zigzag edges are formed between the *trans*-oligoene chains and the graphene domains, which are known as Raman silent.[17] Consequently, this allows us to correlate the Raman modes of graphene with lattice defects and the *trans*-oligoene signals. Thus, we used the heterogenous CVD graphene to ensure same experimental conditions (laser power, amount of iodine) for all data points of the Raman maps, as displayed in Figure 2A. 528 spectra were collected and filtered to exclude substrate and adlayer spectra prior to analysis yielding a data set of 256 monolayer spectra of heterogenous CVD graphene. Those spectra were fitted using Lorentzian functions (Figure S2A). The area of the D-mode (A_D) was used as a measure for defects since it steadily increases with increasing density of defects and is also related to the distance of defects. Vecera *et al.* reported that A_D increases exponentially with the introduction of defects, which is also observed in our data set (Figure S2B).[18] This strong sensitivity allows the detection of minor changes within the graphene lattice.

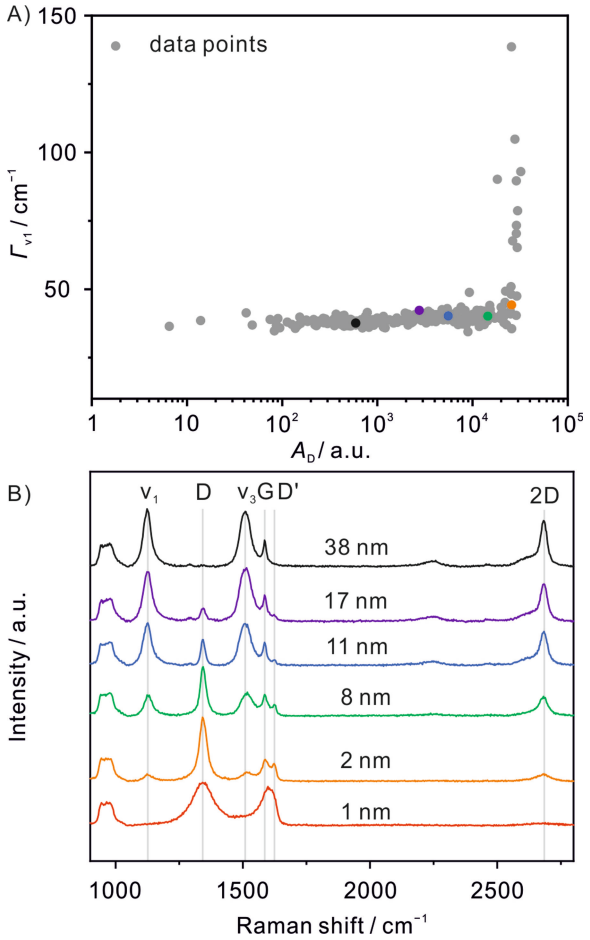

Figure 2. A) Scatter plot of Γ_{v1} against A_D of heterogenous CVD graphene. The coloured dots are the spectra shown in B. B) Raman spectra of iodinated CVD graphene with increasing defect densities (λ_{exc} = 532 nm). The important Raman modes are marked with grey lines.

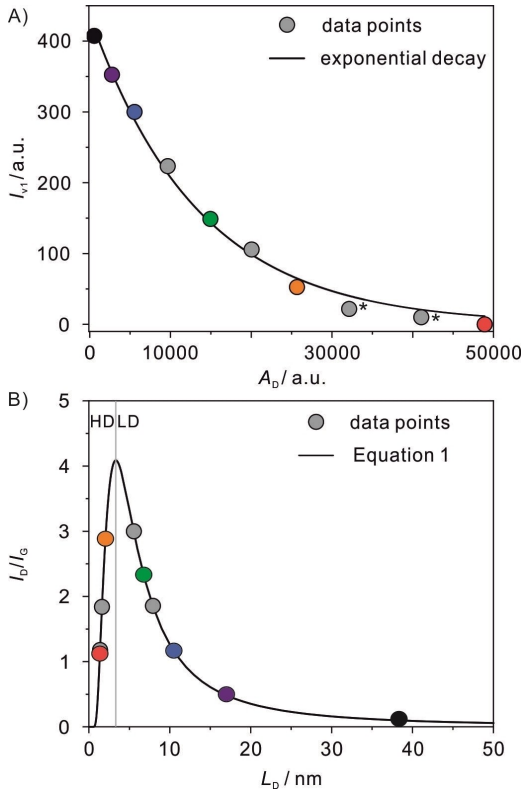

Figure 3. A) Plot of I_{v1} over A_D including the spectra shown in A. The data are in good agreement with an exponential decay fit (Equation 2). For spectra marked with an asterisk v_1 and v_3 could not be fitted anymore and I_{v1} was estimated (Figure S3). B) I_D/I_G ratios plotted against L_D; the solid line follows Equation 1. HD: high defect regime, LD: low defect regime. To distinguish between the HD and LD, Γ_{2D} (50 cm^{-1}) was used.

Plotting the full-width at half-maximum (Γ_{v1}, ~38 cm^{-1}, Figure 2A) and the peak position (xc_{v1}, ~1125 cm^{-1}) against A_D shows that these properties do not significantly vary over a large range of defect distances (Figure S3A and B). After irradiation, we generally observe that the intensity of the v_1- and v_3- modes are lower when the D- and D'-mode are stronger (Figure 2B). At L_D < 2 nm the decreasing intensity of the v_1-mode and the simultaneous increase of the D-mode make proper fitting of peaks challenging (spectra marked with an asterisk in Figure 3A) due to the overlap of D- and v_1-peak (Figure S4) and I_{v1} was approximated here. Plotting A_{v1} and I_{v1} against A_D shows that they are stable over three orders of magnitude before they drop at A_D~10,000 when plotted on a double logarithmic scale (Figure S3C and D) and increase again at high defect densities due to the increasing overlap of the D-mode in the area (Figure S4). Since I_{v1} decreases as the number of defects increases, we assume that it is related to the number of *trans*-oligoene substructures with a matching bandgap in the probed area by the 532 nm laser.

The measured data were fitted by an exponential decay function, as described by Equation 2 where I_0 is the intensity of v_1 without defects and a is an empirical parameter (Figure 3A).

$$I_{v1}(A_D) = I_0 e^{-\frac{A_D}{a}} \quad (2)$$

The observed correlation demonstrates the dependance of lattice defects in graphene and the formation of *trans*-oligoene substructures upon iodination reaction. The fitted parameters are summarized in Table S2. The fitting function covers the full range of defects and reveals a continuous correlation in the low- and high defect regimes (Figure 3B). For highly defective graphene with L_D < 1 nm the material structure significantly differs from intact graphene since defective graphene is polydisperse with carbon domains, which even no longer bear hexagonal carbon lattices and thus contain next to point-like defects, large holes, and also amorphous carbon domains.[19] Therefore, graphene with such high defect density is not suited for the formation *trans*-oligoene substructures. This observation can explain the absence of characteristic signals in defect-rich reduced graphene oxide, since the absence of sufficiently large graphene domains and the exponential increase of the graphene Raman modes would prevent the detection of *trans*-oligoene substructures.

Due to the resonance Raman effect only *trans*-oligoene chains with a bandgap close to the laser energy (2.33 eV) can be detected.[20] The observed signals are in good agreement with those of *tbu*-capped *trans*-oligoene molecules (Figure S5) reported by Schaffer *et al.*[21] containing around eleven double

bonds (bandgap: 2.35 eV, $v_1 = 1125.1\ cm^{-1}$, $v_3 = 1514\ cm^{-1}$). Such a carbon chain would have a length of ~2.6 nm, larger than the observed limit in our Raman spectra but on the same order of magnitude. Shorter substructures with a larger bandgap may also be present within the graphene domains (Figure 4) but are difficult to probe due to the reported defunctionalization at higher excitation energies.[5]

In graphene without defects the maximum chain length of *trans*-oligoene substructures is only limited by the extent of the π-radical delocalization within the graphene lattice. In defective graphene the reactivity towards iodine radicals is increased on the one hand, on the other hand defects limit the extension of π-radicals and therefore, the achievable *trans*-oligoene chain length is limited. In defective CVD graphene typical lattice defects are rearranged carbons, such as Stone-Wales defects and extended line defects.[7] In addition, the carbon lattice may be ruptured by the transfer process causing additional lattice defects. Reduced oxo-graphene consists of graphene with point defects and larger holes that are introduced by overoxidation of the graphene lattice during the functionalization process. From previous aberration corrected transmission electron microscopy (ac-TEM) studies the atomic structure of thermally annealed $oxoG_{4\%}$ was visualized and consists of graphene domains with few point-defects and holes due to the disproportionation of oxygen containing groups, resulting in L_D values of about 5–10 nm.[22]

Even for graphene with more defects, e.g. obtained from thermal annealing of oxo-$G_{50\%}$, at 300 °C highly intact graphene domains with diameters of ~5 nm have been observed by ac-TEM that would still allow *trans*-oligoene substructure formation, although most other graphene domains have diameters of about 1 nm.[19] This demonstrates the heterogeneity of defective graphene and the limitation of the model of statistically distributed defects within an otherwise intact graphene lattice. Thus, the inhomogeneity of materials can explain the emergence of *trans*-oligoene Raman signals at defect distances smaller than the length of the probed substructures. Due to the small number of such domains the observed signal is minor, since the major amount of present carbon results in larger signals (see Supplementary Note 5). The constant Γ_{v1} and xc_{v1} suggest a narrow distribution of *trans*-oligoene substructures (Figure S2), as expected by resonance Raman spectroscopy.[23] The strong decrease of I_{v1} is in good agreement with the necessity of intact graphene domains for *trans*-oligoene substructure formation, as evident in Figure 4: Iodine radicals add to defect-activated carbon bonds close to lattice defects and form *trans*-oligoene substructures by isolation of double bonds between the sp^3-defects. Thus, the number and length of the substructures are limited by the size of the intact graphene domains, which explains the disappearance of the *trans*-oligoene Raman modes in the high defect regime.

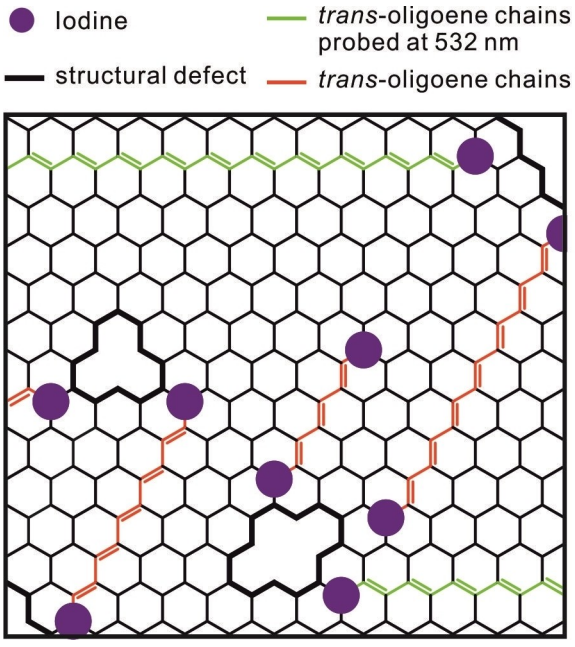

Figure 4. Schematic illustration of the proposed trans-oligoene substructures in defective graphene. Structural defects are starting points of substructure formation due to increased reactivity and limit the size of intact graphene domains. Substructures with a bandgap close to the laser energy (2.33 eV) are probed (green) while shorter ones with a larger bandgap (red) do not contribute significantly to the resonance Raman signal. Double bonds of graphene have been omitted for clarity.

Conclusions

Trans-oligoene substructure formation can be induced in graphene with lattice defects via photochemical iodination reaction and characteristic Raman modes are observed. No significant change of the D-mode intensity is detected in the most Raman-sensitive defect regime with defect distances around 2–3 nm, suggesting that newly formed defects by the iodination reaction are Raman silent or below the detection limit. For addition reactions to graphene, the reaction is mostly followed by D-mode formation and therefore, no study was possible investigating reactions on graphene without affecting the D-mode. Since the formation of *trans*-oligoene substructures does not affect the D-mode of graphene, the iodination reaction could be monitored by Raman spectroscopy as a function of defect density. Statistical Raman analysis of graphene samples with varying defect distances reveals the correlation between I_{v1} and the number of lattice defects, underscoring the strong dependence of *trans*-oligoene substructure formation on structural defects within the graphene lattice. At defect distances below ~1 nm no *trans*-oligoene Raman modes are observed, indicating that the size of the remaining intact graphene domains becomes too small for their formation and ability for probing by 532 nm laser excitation. Our observations may be exploited in the future to drive regiochemical functionalization strategies of graphene-type materials, leading to periodically functionalized materials suitable for various fields of research.

Experimental Section

Materials and Methods

Methanol used for sample preparation was distilled in a solvent circulation apparatus to remove any impurities before use. Iodine was purchased from TCI and used as received. Graphite type 3061 was obtained from Asbury Carbon Mills and all other materials were purchased from Sigma-Aldrich and used as received. Si wafers with a 300 nm thick SiO_2 layer were purchased from Fraunhofer Institut für Integrierte Systeme und Bauelementetechnologie IISB in Erlangen. Thermal annealing of samples in vacuum was made using a Nabertherm 30–3,000 °C oven.

Raman Spectroscopy

Statistical Raman spectroscopic characterization was carried out on a Horiba Jobin Yvon XploRA™ PLUS spectrometer equipped with a confocal microscope and an automated XYZ table. Spectra were recorded with a green laser (532 nm, 2.33 eV) combined with a 100x objective resulting in a spot size of about 700 nm and 1,200 groves mm^{-1} grating was used. The Raman shift was calibrated to the Si peak before measurement.

Raman data were analyzed using the Origin 2019b software and signals were fitted using single Lorentzian functions. Baseline corrections were directly made in the LabSpec6 software of the instrument and spikes were removed prior to data analysis. Statistical Raman data were analyzed using a Python script. The v_1-, D- and 2D-modes were fitted using single Lorentzian functions, while a triple Lorentzian function was used between 1450–1650 cm^{-1} to fit the v_3-, G- and D′-modes.

Preparation of CVD Graphene

Graphene was prepared by chemical vapor deposition on copper foil using the envelope method.[24] After annealing of the copper envelope for 1 h (1035 °C, 10 sccm H_2, 5 sccm Ar) a flow of methane (5 sccm) was added to the mixture for 10 min growth time. Then, the sample was rapidly cooled down to rt. Controlling growth time is critical if a heterogenous quality of graphene is desired.[25] The exact reaction time depends however on the setup. Arbitrary pieces of graphene were transferred onto substrates by wet-transfer method.

Preparation of oxo-$G_{4\%}$

High-quality oxo-functionalized graphene was prepared by our earlier reported method.[14] The oxo-graphite crystals were repeatedly washed by centrifugation and decanting of excess aqueous solution until a neutral pH was reached. The oxo-graphite crystals were freeze-dried in a lyophilizer to remove remaining water. High quality samples were prepared by tape exfoliation using the Scotch tape method and directly transferred onto SiO_2/Si substrates. After reduction, the samples were annealed in vacuum ($T = 300$ °C, $p = 1\times10^{-3}$ mbar, $t = 2$ h) to remove any remaining residues.

Preparation of oxo-$G_{50\%}$

Oxo-graphene with a degree of functionalization around 50 % was prepared by our controlled synthesis approach, reported earlier.[13]

Reduction of oxo-G with HI/TFA

Oxo-graphene was reduced using a mixture of HI and TFA according to our method published elsewhere.[26] Samples were reduced in the vapors of HI and TFA at 80 °C for 5 min. The wafers were placed on the hotplate for 5 min to remove any remaining reducing agents.

Photochemical Iodination Reaction

A solution of iodine in methanol (20 mM, 10 μL) was applied to the sample on the wafer. After complete evaporation of the solvent the sample was irradiated. Measurements of Raman spectra and the patterning experiments were performed at 3 mW laser power. Spectra were measured with an acquisition time of 0.1 s. The light dosage was controlled by the exposure time. For functionalization, 10 accumulations per spot were used with a total irradiation time of 1 s.

Acknowledgements

SE and FG gratefully acknowledge funding from Deutsche Forschungsgemeinschaft (DFG, German Research Foundation, Project No. 392444269). Open Access funding enabled and organized by Projekt DEAL.

Conflict of Interests

The authors declare no conflict of interest.

Keywords: defects · graphene · iodine · Raman spectroscopy · substructures

[1] I. Piquero-Zulaica, J. Lobo-Checa, Z. M. A. El-Fattah, J. E. Ortega, F. Klappenberger, W. Auwärter, J. V. Barth, *Rev. Mod. Phys.* **2022**, *94*.
[2] T. Wei, F. Hauke, A. Hirsch, *Adv. Mater.* **2021**, *33*, e2104060.
[3] J. J. Navarro, S. Leret, F. Calleja, D. Stradi, A. Black, R. Bernardo-Gavito, M. Garnica, D. Granados, A. L. Vazquez de Parga, E. M. Perez, R. Miranda, *Nano Lett.* **2016**, *16*, 355.
[4] a) M. Guo, Z. Qu, F. Min, Z. Li, Y. Qiao, Y. Song, *InfoMat* **2022**, *4*; b) M. Yu, C. Chen, Q. Liu, C. Mattioli, H. Sang, G. Shi, W. Huang, K. Shen, Z. Li, P. Ding, P. Guan, S. Wang, Y. Sun, J. Hu, A. Gourdon, L. Kantorovich, F. Besenbacher, M. Chen, F. Song, F. Rosei, *Nat. Chem.* **2020**, *12*, 1035.
[5] F. Grote, B. I. Weintrub, M. Kressler, Q. Cao, C. E. Halbig, P. Kusch, K. I. Bolotin, S. Eigler, *Small* **2024**, e2311987.
[6] a) P. Šimek, K. Klímová, D. Sedmidubský, O. Jankovský, M. Pumera, Z. Sofer, *Nanoscale* **2015**, *7*, 261; b) A. Wang, S. Bok, C. J. Mathai, K. Gangopadhyay, J. McFarland, M. R. Maschmann, S. Gangopadhyay, *Nano Futur.* **2020**, *4*; c) J. Chen, M. W. Xu, J. Wu, C. M. Li, *Nanoscale* **2018**, *10*, 9115; d) M. S. Mirshekarloo, M. C. D. Cooray, P. Jovanović, C. D. Easton, F. Wu, T. D. Gamot, M. J. Abedin, M. R. Yuce, M. Shaibani, M. Majumder, *Batteries & Supercaps* **2021**, *4*, 1175.
[7] M. D. Bhatt, H. Kim, G. Kim, *RSC Adv.* **2022**, *12*, 21520.
[8] a) C. E. Halbig, R. Lasch, J. Krüll, A. S. Pirzer, Z. Wang, J. N. Kirchhof, K. I. Bolotin, M. R. Heinrich, S. Eigler, *Angew. Chem. Int. Ed.* **2019**, *58*, 3599; b) Y. Wang, F. Grote, Q. Cao, S. Eigler, *J. Phys. Chem. Lett.* **2021**, *12*, 10009.
[9] a) M. M. Lucchese, F. Stavale, E. H. M. Ferreira, C. Vilani, M. V. O. Moutinho, R. B. Capaz, C. A. Achete, A. Jorio, *Carbon* **2010**, *48*, 1592; b) L. G. Cançado, A. Jorio, E. H. Ferreira, F. Stavale, C. A. Achete, R. B. Capaz, M. V. Moutinho, A. Lombardo, T. S. Kulmala, A. C. Ferrari, *Nano Lett.* **2011**, *11*, 3190.

[10] a) S. J. Goldie, S. Bush, J. A. Cumming, K. S. Coleman, *ACS Appl. Nano Mater.* **2020**, *3*, 11229; b) S. Eigler, F. Hof, M. Enzelberger-Heim, S. Grimm, P. Müller, A. Hirsch, *J. Phys. Chem. C* **2014**, *118*, 7698; c) A. A. Graf, S. P. Ogilvie, H. J. Wood, C. J. Brown, M. Tripathi, A. A. K. King, A. B. Dalton, M. J. Large, *Chem. Mater.* **2020**, *32*, 6213.
[11] J. M. Englert, P. Vecera, K. C. Knirsch, R. A. Schäfer, F. Hauke, A. Hirsch, *ACS Nano* **2013**, *7*, 5472.
[12] S. Eigler, C. Dotzer, A. Hirsch, *Carbon* **2012**, *50*, 3666.
[13] S. Eigler, *Chemistry* **2016**, *22*, 7012.
[14] S. Eigler, *Chem. Commun.* **2015**, *51*, 3162.
[15] a) G. Copetti, E. H. Nunes, G. K. Rolim, G. V. Soares, S. A. Correa, D. E. Weibel, C. Radtke, *J. Phys. Chem. C* **2018**, *122*, 16333; b) W. Li, Y. Li, K. Xu, *Nano Lett.* **2021**, *21*, 1150; c) X. Zhang, A. Hsu, H. Wang, Y. Song, J. Kong, M. S. Dresselhaus, T. Palacios, *ACS Nano* **2013**, *7*, 7262; d) W. Li, Y. Li, K. Xu, *Nano Lett.* **2020**, *20*, 534.
[16] A. Setaro, M. Adeli, M. Glaeske, D. Przyrembel, T. Bisswanger, G. Gordeev, F. Maschietto, A. Faghani, B. Paulus, M. Weinelt, R. Arenal, R. Haag, S. Reich, *Nat. Commun.* **2017**, *8*, 14281.
[17] C. Casiraghi, A. Hartschuh, H. Qian, S. Piscanec, C. Georgi, A. Fasoli, K. S. Novoselov, D. M. Basko, A. C. Ferrari, *Nano Lett.* **2009**, *9*, 1433.
[18] P. Vecera, S. Eigler, M. Kolesnik-Gray, V. Krstic, A. Vierck, J. Maultzsch, R. A. Schäfer, F. Hauke, A. Hirsch, *Sci. Rep.* **2017**, *7*, 45165.
[19] Z. Wang, Q. Yao, C. Neumann, F. Börrnert, J. Renner, U. Kaiser, A. Turchanin, H. J. W. Zandvliet, S. Eigler, *Angew. Chem. Int. Ed.* **2020**, *59*, 13657.
[20] K. Furuya, A. Sakamoto, M. Tasumi, *J. Phys. Chem. A* **2023**, *127*, 5344.
[21] H. E. Schaffer, R. R. Chance, R. J. Silbey, K. Knoll, R. R. Schrock, *J. Chem. Phys.* **1991**, *94*, 4161.
[22] F. Grote, C. Gruber, F. Börrnert, U. Kaiser, S. Eigler, *Angew. Chem. Int. Ed.* **2017**, *56*, 9222.
[23] H. Kuzmany, *Macromol. Symp.* **1990**, *37*, 81.
[24] X. Li, C. W. Magnuson, A. Venugopal, R. M. Tromp, J. B. Hannon, E. M. Vogel, L. Colombo, R. S. Ruoff, *J. Am. Chem. Soc.* **2011**, *133*, 2816.
[25] T. Niu, M. Zhou, J. Zhang, Y. Feng, W. Chen, *J. Am. Chem. Soc.* **2013**, *135*, 8409.
[26] S. Eigler, S. Grimm, M. Enzelberger-Heim, P. Müller, A. Hirsch, *Chem. Commun.* **2013**, *49*, 7391.

Manuscript received: March 13, 2024
Accepted manuscript online: April 8, 2024
Version of record online: ■■, ■■

Chemistry–A European Journal

Supporting Information

Influence of Lattice Defects on *Trans*-Oligoene Substructure Formation in Graphene

Fabian Grote and Siegfried Eigler*

Supporting Information

69451 Weinheim, Germany

Influence of Lattice Defects on *Trans*-Oligoene Substructure Formation in Graphene

Fabian Grote[a] and Siegfried Eigler[a]*

[a] M.Sc. F. Grote, Prof. Dr. S. Eigler
Institut für Chemie und Biochemie
Freie Universität Berlin
Altensteinstraße 23a, 14195 Berlin, Germany
E-Mail: siegfried.eigler@fu-berlin.de

Abstract: The photochemical reaction of iodine and graphene induces strong new Raman modes due to the formation of *trans*-oligoene substructures in graphene domains. This unique reactivity was demonstrated before on defect-free graphene, however leaving the influence of e.g. carbon vacancies, unexplored. Here, we investigate the photochemical reaction applied on graphene with varying average distances of lattice defects and statistically analyze the characteristic Raman modes which develop with the iodination reaction. We show that the iodination reaction does not lead to Raman-active defects and thus, the newly formed *trans*-oligoene substructures do not contribute to the D-mode of graphene. A statistical analysis reveals the correlation between the average distance of lattice defects and the intensity of the v_1-mode. For defective graphene with average defect distances below ~1 nm no new Raman modes evolve, which is the lower limit of the substructure size probed at 532 nm and explains why this observation was not possible before using common graphene oxide as graphene source.

DOI: 10.1002/chem.202401031

Supplementary Note 1: Introduction of Raman-active defects by iodination reaction

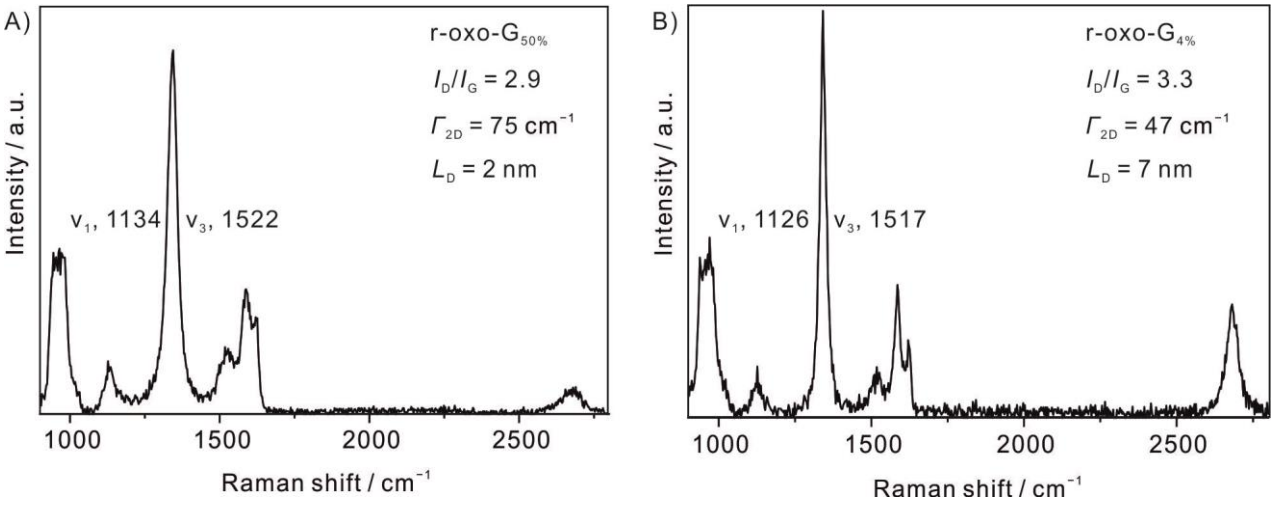

Figure S1. A) Representative Raman spectrum of r-oxo-$G_{50\%}$ showing the formation of the characteristic Raman modes in the high defect regime. B) Representative Raman spectrum of r-oxo-$G_{4\%}$ showing the formation of the characteristic Raman modes in the low defect regime.

The results of the iodination tests with two reduced oxo-graphene samples shown in **Figure S1** is summarized in **Table S1**. No significant change of the D-peak is observed in the samples. Since no significant correlation between functionalization and the D-mode can be observed, the defect-dependent signal intensity of v_1 and v_3 within a Raman spectrum can be assumed not to change the graphene related Raman signals.

Table S1. Intensity ratios of reduced oxo-graphene samples before and after iodination reaction showing no change within the error margin upon iodination reaction.

Compound	I_D/I_G	N_C
r-oxo-$G_{50\%}$_iodinated (I_{v1} > 100)	2.66 ± 0.19 (45)	125 ± 11
r-oxo-$G_{50\%}$_pristine (I_{v1} < 100)	2.73 ± 0.22 (694)	130 ± 14
r-oxo-$G_{4\%}$_iodinated	3.10 ± 0.23 (97)	942 ± 180
r-oxo-$G_{4\%}$_pristine	3.11 ± 0.22 (127)	942 ± 150

Supplementary Note 2: Selection of spectroscopic parameters

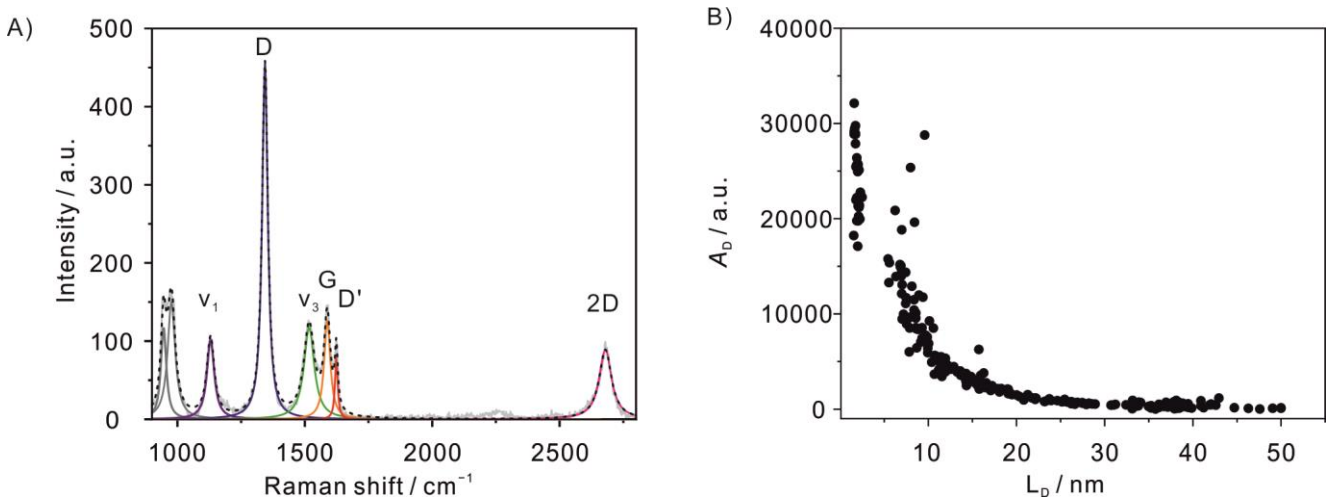

Figure S2. A) Raman spectrum of iodinated CVD graphene with Lorentzian peak fits. While the v_1- and D-mode fits are undisturbed by other peaks, v_3-, G- and D'-modes are close together and the Lorentzian fits overlap complicating the deconvolution of the signals. B) Plot of A_D against L_D calculated from **Equation 1** showing its exponential increase with decreasing defect distance. At around 5 nm there appears lack of data that may be due to the inaccurate description of the data in that region.

Figure S2A shows a representative Raman spectrum of iodinated CVD graphene with the peak fits to demonstrate the deconvolution of a typical Raman spectrum. Seven modes can be fitted that yield information on various properties of graphene and the *trans*-oligoene substructures.

The D-peak indicates the presence of scattering sites in the graphene lattice and is analyzed using the I_D/I_G ratio by fitting of the data to **Equation 1**. Since no significant D-mode formation is observed upon iodination we assume no change by *trans*-oligoene substructure formation. At high defect densities (below L_D ~3 nm) the obtained values become inaccurate due to the non-linear variation of I_D.

The v_1-mode was chosen to analyze *trans*-oligoene substructures due to its Lorentzian line shape and its isolated position in the spectrum that allows fitting without overlap for intact graphene. At large defect densities, the D-peak starts to overlap with v_1 in addition to its decreasing intensity (**Figure S3**). The proximity of the v_3- and G-peak complicate the fitting of both peaks and especially the extraction of the Γ_G value, that is typically used as a quality criterium, becomes problematic at higher defect densities when the D'-mode is also present. A triple Lorentzian fit function must be used.

Instead, we used the full-width at half-maximum of the 2D-mode (Γ_{2D}) to select spectra in that range due to its baseline-separation from the other peaks. It remains below 50 cm^{-1} for the highly intact region up to ~3 nm and increases strongly at smaller defect distances.[1]

In the high-defect regime the assignment has a high uncertainty since small changes of the ratio strongly influence the associated degree of functionalization.

The optimized values given in **Table S2** were used for all calculations using **Equation 1**. C_A is the maximum possible I_D/I_G ratio if all carbons contributed to the D-peak signal. The radii r_S and r_A correspond to the structurally disordered and the activated graphene area respectively and were assigned phenomenologically.[2]

Table S2. Parameters used in **Equation 1** to obtain L_D values from I_D/I_G ratios. Γ_{2D} (50 cm^{-1}) was used as a quality criterium to distinguish between the low- and high-defect region.

Parameter	value
E_L	2.33 eV
$C_A = 160*E_L^{-4}$	5.429
r_A	3.1 nm
r_S	1 nm

To calculate a defect degree in % from the measured spectra the statistical defect distance was converted to the area of intact graphene between defects F_D using **Equation S1**.

$$F_D\ (\mathrm{nm}^2) = \frac{\sqrt{3}}{2} L_D^2 \qquad (\mathbf{S1})$$

The area can be used to extract the number of intact carbon atoms N_C by division of F_D by the area of a single carbon atom using **Equation S2**.

$$N_C = \frac{\text{defect area}}{\text{area of a single carbon}} \qquad (\mathbf{S2})$$

The space taken by a single carbon in the graphene lattice of 0.02623 nm^2 was taken form literature.[3] The number of carbon atoms per defect then gives the defect degree θ using **Equation S3**.

$$\theta\ (\%) = \frac{1}{N_C} * 100 \qquad (\mathbf{S3})$$

Table S3. Fitted values of the exponential decay fit in **Figure 3A**.

Parameter	value
I_0	436 ± 10
a	13475 ± 608
Reduced Chi-Square	144.6
R-square	0.99

Supplementary Note 3: Statistical analysis of functionalization data

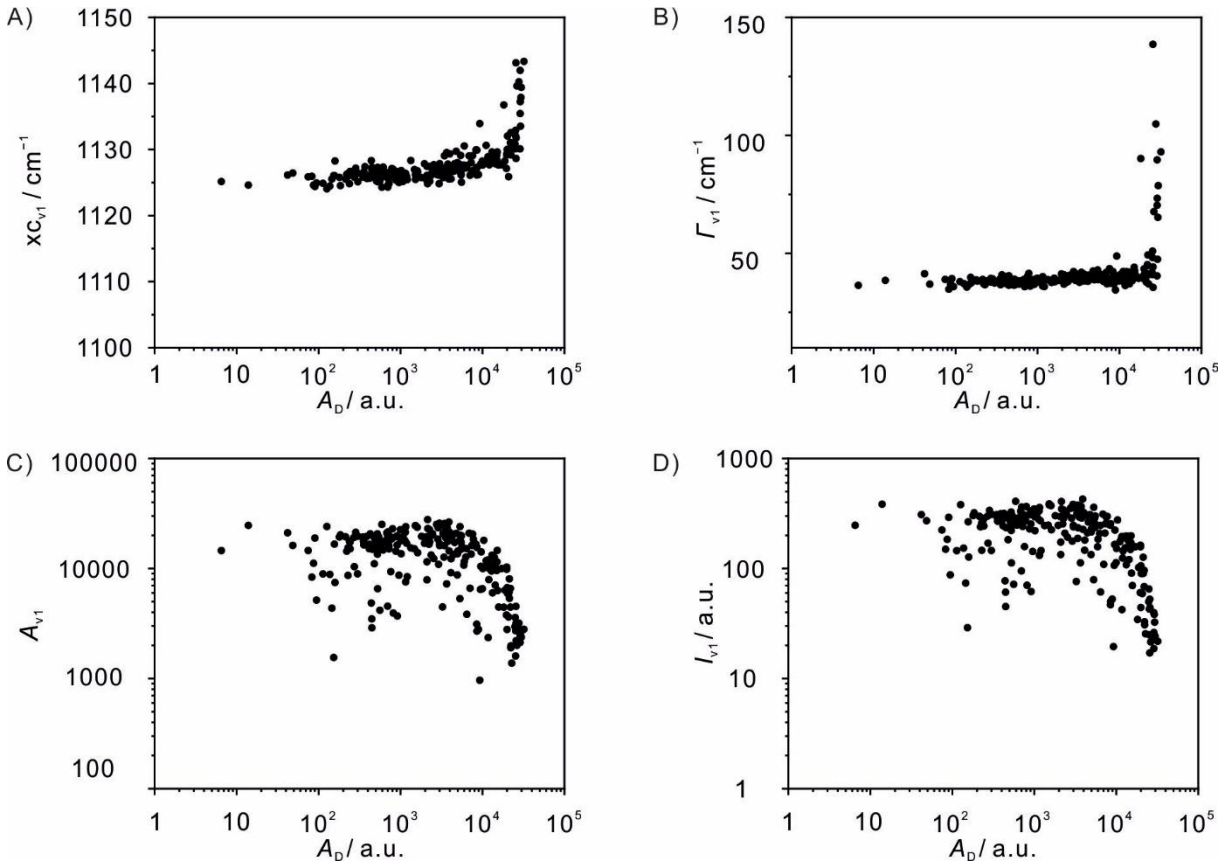

Figure S3. Statistical analysis of the spectroscopic parameters of v_1-mode from heterogenous CVD graphene. A) Scatter plot of xc_{v1} against A_D. B) Scatter plot of Γ_{v1} against A_D. C) Scatter plot of A_{v1} against A_D. D) Scatter plot of I_{v1} against A_D showing steep decline at large A_D values.

Figure S3 shows the statistical distribution of the Lorentzian peak fit parameters (I_{v1}, A_{v1}, Γ_{v1}, xc_{v1}) plotted against A_D. Only a small variation of the peak position (~1125 cm^{-1}) before increasing at high defect densities, which may also be due to the increasing difficulty to fit the small peaks with the strong influence of the adjacent D-peak. The full-width at half-maximum Γ_{v1} (~38 cm^{-1}) is also constant at low defect densities and, increases as the modes become smaller at high defect densities. These changes are likely influenced by the increasing contribution of the overlapping D-mode with the v_1-mode.

Supplementary Note 4: Fitting of v_1 mode at high structural defect densities

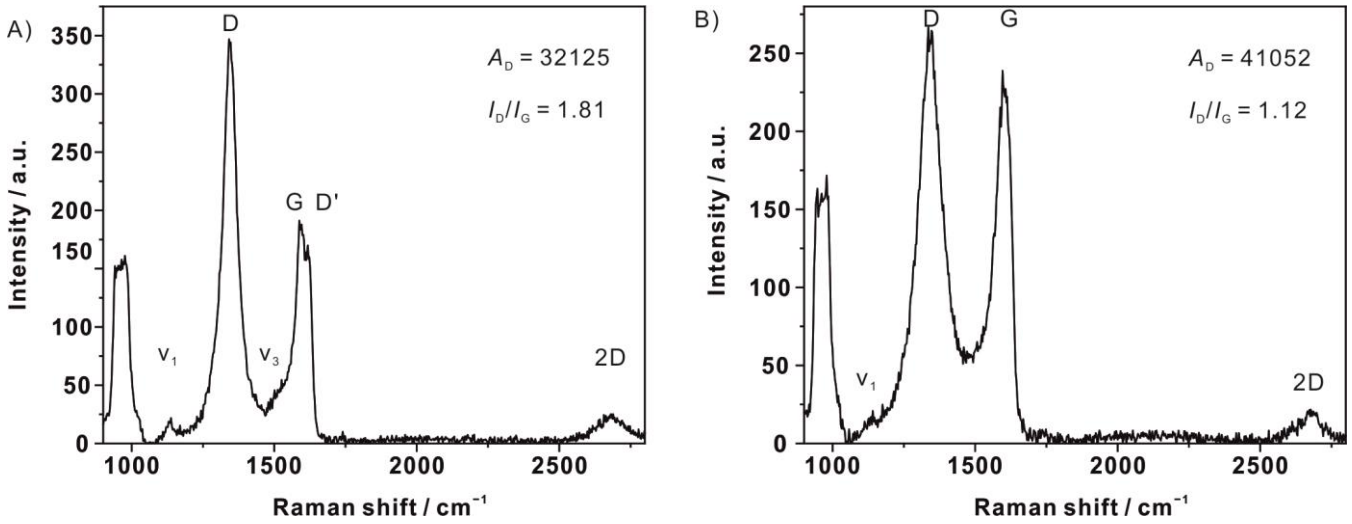

Figure S4. Raman spectra of iodinated graphene marked with an asterisk in **Figure 3A**. A) While the v_1-mode is only slightly influenced by the strong D-mode, the v_3-mode is only visible as a shoulder. B) Due to the strong overlap of the v_1- and D-mode, deconvolution is necessary to exclude the influence of the D-mode.

Figure S4 shows the Raman spectra corresponding to the data points marked with an asterisk in **Figure 3A** that are in the high-defect region. Without deconvolution of the spectra I_{v1} is overestimated since the overlapping D-peak contributes to the signal intensity, while I_{v1} decreases substantially. This causes the v_1 and v_3-modes to increase at high defect densities for the script-based data analysis and must be corrected manually.

Supplementary Note 5: Geometric considerations, effects of structural defects on substructure formation

A Raman spectrum is the sum of all carbon atoms within the irradiated area. Here, the laser spot size is about 700 nm corresponding to an area of 1.1 µm^2 per spectrum with ~4.2 x 10^7 carbon atoms (single carbon atom area: 0.02623 nm^2[3]). Point defects in the graphene lattice would not significantly reduce the number of intact carbon atoms available for *trans*-oligoene substructure formation. For example at L_D = 10 nm the number of intact carbons is only reduced by 0.03 %, while I_{v1} is reduced by ~60 % compared to defect-free graphene. In this range graphene properties are still largely unchanged as reflected by the sharp 2D-mode. In contrast, at L_D = 1 nm the number of intact carbon atom decreases to 3 % on average and graphene signals change strongly due to the exponential increase of the peak area and the 2D-mode becomes broad. However, defect formation does not occur in a defined manner as the statistical calculations suggest since larger holes are also formed e.g. by disproportionation reactions or rupture introduced during the transfer process, leading to areas with relatively intact graphene domains and large defective areas in which no substructure formation will be possible.

Supplementary Note 6: *Tbu*-capped *trans*-oligoene molecules

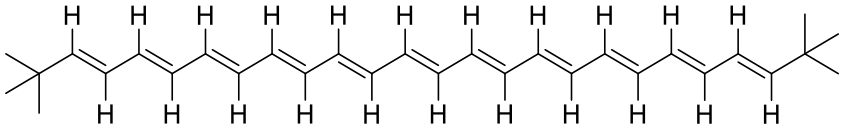

Figure S5. Molecular structure of a *tbu*-capped *trans*-oligoene with eleven double bonds possess a bandgap of 2.35 eV, close to the laser energy used in our experiments (2.33 eV) showing similar Raman signals.

Figure S5 shows the molecular structure of a *tbu*-capped *trans*-oligoene molecule synthesized by Knoll and Schrock[4] and was subsequently characterized in a series of *trans*-oligoenes to assess the chain-length dependent Raman properties. A bandgap of around 2.33 eV was measured for molecules with ten (2.25 eV, v_1 = 1130 cm^{-1}, v_3 = 1521 cm^{-1}) and eleven (2.35 eV, v_1 = 1125 cm^{-1}, v_3 = 1514 cm^{-1}) double bonds that have peak positions close to the Raman signals observed in iodinated graphene (**Figure S3A**). The length of such a chain containing 22 carbon atoms is ~2.6 nm.

References

[1] S. Eigler, F. Hof, M. Enzelberger-Heim, S. Grimm, P. Müller, A. Hirsch, *J. Phys. Chem. C* **2014**, *118*, 7698.
[2] M. M. Lucchese, F. Stavale, E. H. M. Ferreira, C. Vilani, M. V. O. Moutinho, R. B. Capaz, C. A. Achete, A. Jorio, *Carbon* **2010**, *48*, 1592.
[3] S. Reich, J. Maultzsch, C. Thomsen, P. Ordejón, *Phys. Rev. B* **2002**, *66*, 035412.
[4] K. Knoll, R. R. Schrock, *J. Am. Chem. Soc.* **1989**, *111*, 7989.

Author Contributions

Fabian Grote: Conceptualization, Data curation, Investigation, Visualization, Writing – original draft. **Siegfried Eigler:** Supervision, Validation, funding acquisition, methodology, project administration, resources, writing – review and editing.

7 Publications – Minor Contributions

7.1 The importance of molecular structure and functionalization of oxo-graphene sheets for gene silencing

Authors	G. Reina, C. Gabellini, M. Maranska, F. Grote, S.H. Chin, L. Jacquemin, F. Berger, P. Posocco, S. Eigler, A. Bianco
Journal	*Carbon* **2022**, *195*, 69.
DOI	10.1016/j.carbon.2022.03.066
Links	https://doi.org/10.1016/j.carbon.2022.03.066
Detailed scientific contribution	Samples for elemental analyses were prepared by F. Grote.
Estimated own contribution	~5%

7.2 Regiochemically Oxo-functionalized Graphene, Guided by Defect Sites, as Catalyst for Oxygen Reduction to Hydrogen Peroxide

Authors	Y. Wang, F. Grote, Q. Cao, S. Eigler
Journal	*J. Phys. Chem. Lett.* **2021**, *12*, 10009.
DOI	10.1021/acs.jpclett.1c02957
Links	https://doi.org/10.1021/acs.jpclett.1c02957
Detailed scientific contribution	Oxo-$G_{4\%}$ was synthesized and characterized by F. Grote. F. Grote assisted the revision of the manuscript.
Estimated own contribution	~10%

7.3 Emerging field of few-layered intercalated 2D materials

Authors	Q. Cao, F. Grote, M. Hußmann, S. Eigler
Journal	*Nanoscale Adv.* **2021**, *3*, 963.
DOI	10.1039/D0NA00987C
Links	https://doi.org/10.1039/D0NA00987C

Detailed scientific contribution	The chapter on electrochemical intercalation of 2D materials was written by F. Grote.
Estimated own contribution	~30%

8 References

[1] E. H. L. Falcao, F. Wudl, *J. Chem. Technol. Biotechnol.* **2007**, *82*, 524.
[2] A. Hirsch, *Nat. Mater.* **2010**, *9*, 868.
[3] P. Ares, K. S. Novoselov, *Nano Mater. Sci.* **2022**, *4*, 3.
[4] J. E. Field, *Rep. Prog. Phys.* **2012**, *75*, 126505.
[5] C. E. Nebel, in *Nanodiamonds*, **2017**, pp. 1.
[6] F. P. Bundy, W. A. Bassett, M. S. Weathers, R. J. Hemley, H. U. Mao, A. F. Goncharov, *Carbon* **1996**, *34*, 141.
[7] Y. Gong, D. Luo, M. Choe, Y. Kim, B. Ram, M. Zafari, W. K. Seong, P. Bakharev, M. Wang, I. K. Park, S. Lee, T. J. Shin, Z. Lee, G. Lee, R. S. Ruoff, *Nature* **2024**, *629*, 348.
[8] S. Reich, J. Maultzsch, C. Thomsen, P. Ordejón, *Phys. Rev. B* **2002**, *66*, 035412.
[9] A. K. Dutta, *Phys. Rev.* **1953**, *90*, 187.
[10] L. Hou, X. Cui, B. Guan, S. Wang, R. Li, Y. Liu, D. Zhu, J. Zheng, *Nature* **2022**, *606*, 507.
[11] Q. Fan, L. Yan, M. W. Tripp, O. Krejci, S. Dimosthenous, S. R. Kachel, M. Chen, A. S. Foster, U. Koert, P. Liljeroth, J. M. Gottfried, *Science* **2021**, *372*, 852.
[12] H. W. Kroto, J. R. Heath, S. C. O'Brien, R. F. Curl, R. E. Smalley, *Nature* **1985**, *318*, 162.
[13] A. V. Mumyatov, P. A. Troshin, *Energies* **2023**, *16*, 1924.
[14] S. Iijima, *Nature* **1991**, *354*, 56.
[15] A. D. Franklin, M. C. Hersam, H. P. Wong, *Science* **2022**, *378*, 726.
[16] Y. Lin, Y. Cao, S. Ding, P. Zhang, L. Xu, C. Liu, Q. Hu, C. Jin, L.-M. Peng, Z. Zhang, *Nat. Electron.* **2023**, *6*, 506.
[17] Y. Gao, R. R. Tykwinski, *Acc. Chem. Res.* **2022**, *55*, 3616.
[18] Y. Gao, Y. Hou, F. Gordillo Gamez, M. J. Ferguson, J. Casado, R. R. Tykwinski, *Nat. Chem.* **2020**, *12*, 1143.
[19] K. Kaiser, L. M. Scriven, F. Schulz, P. Gawel, L. Gross, H. L. Anderson, *Science* **2019**, *365*, 1299.
[20] Y. Gao, F. Albrecht, I. Roncevic, I. Ettedgui, P. Kumar, L. M. Scriven, K. E. Christensen, S. Mishra, L. Righetti, M. Rossmannek, I. Tavernelli, H. L. Anderson, L. Gross, *Nature* **2023**, *623*, 977.
[21] a) D. Malko, C. Neiss, F. Vines, A. Gorling, *Phy. Rev. Lett.* **2012**, *108*, 086804; b) X. Zheng, S. Chen, J. Li, H. Wu, C. Zhang, D. Zhang, X. Chen, Y. Gao, F. He, L. Hui, H. Liu, T. Jiu, N. Wang, G. Li, J. Xu, Y. Xue, C. Huang, C. Chen, Y. Guo, T. B. Lu, D. Wang, L. Mao, J. Zhang, Y. Zhang, L. Chi, W. Guo, X. H. Bu, H. Zhang, L. Dai, Y. Zhao, Y. Li, *ACS Nano* **2023**, *17*, 14309.
[22] L. Chen, Y. Hernandez, X. Feng, K. Müllen, *Angew. Chem. Int. Ed.* **2012**, *51*, 7640.
[23] C. D. Simpson, J. D. Brand, A. J. Berresheim, L. Przybilla, H. J. Rader, K. Müllen, *Chem. Eur. J.* **2002**, *8*, 1424.
[24] X. H. Ma, X. Gao, J. Y. Chen, M. Cao, Q. Dai, Z. K. Jia, Y. B. Zhou, X. J. Zhao, C. Chu, G. Liu, Y. Z. Tan, *J. Am. Chem. Soc.* **2024**, *146*, 2411.
[25] R. S. K. Houtsma, J. de la Rie, M. Stohr, *Chem. Soc. Rev.* **2021**, *50*, 6541.
[26] O. V. Yazyev, *Acc. Chem. Res.* **2013**, *46*, 2319.

[27] Y. Gu, Z. Qiu, K. Müllen, *J. Am. Chem. Soc.* **2022**, *144*, 11499.
[28] A. Peigney, C. Laurent, E. Flahaut, R. R. Bacsa, A. Rousset, *Carbon* **2001**, *39*, 507.
[29] K. S. Novoselov, A. K. Geim, S. V. Morozov, D. Jiang, Y. Zhang, S. V. Dubonos, I. V. Grigorieva, A. A. Firsov, *Science* **2004**, *306*, 666.
[30] N. D. Mermin, *Phys. Rev.* **1968**, *176*, 250.
[31] A. Fasolino, J. H. Los, M. I. Katsnelson, *Nat. Mater.* **2007**, *6*, 858.
[32] A. H. Castro Neto, F. Guinea, N. M. R. Peres, K. S. Novoselov, A. K. Geim, *Rev. Mod. Phys.* **2009**, *81*, 109.
[33] L. Banszerus, M. Schmitz, S. Engels, M. Goldsche, K. Watanabe, T. Taniguchi, B. Beschoten, C. Stampfer, *Nano Lett.* **2016**, *16*, 1387.
[34] A. A. Balandin, S. Ghosh, W. Bao, I. Calizo, D. Teweldebrhan, F. Miao, C. N. Lau, *Nano Lett.* **2008**, *8*, 902.
[35] F. Schwierz, *Nat. Nanotechnol.* **2010**, *5*, 487.
[36] Y. Cao, V. Fatemi, S. Fang, K. Watanabe, T. Taniguchi, E. Kaxiras, P. Jarillo-Herrero, *Nature* **2018**, *556*, 43.
[37] A. Nimbalkar, H. Kim, *Nano-Micro Lett.* **2020**, *12*, 126.
[38] G. Xie, R. Yang, P. Chen, J. Zhang, X. Tian, S. Wu, J. Zhao, M. Cheng, W. Yang, D. Wang, C. He, X. Bai, D. Shi, G. Zhang, *Small* **2014**, *10*, 2280.
[39] M. Acik, Y. J. Chabal, *Jpn. J. Appl. Phys.* **2011**, *50*, 070101.
[40] S. K. Tiwari, S. K. Pandey, R. Pandey, N. Wang, M. Bystrzejewski, Y. K. Mishra, Y. Zhu, *Small* **2023**, *19*, e2303340.
[41] F. Banhart, J. Kotakoski, A. V. Krasheninnikov, *ACS Nano* **2011**, *5*, 26.
[42] H. Lee, K. Paeng, I. S. Kim, *Synth. Met.* **2018**, *244*, 36.
[43] C. Wetzl, A. Silvestri, M. Garrido, H. L. Hou, A. Criado, M. Prato, *Angew. Chem. Int. Ed.* **2023**, *62*, e202212857.
[44] Y. Hu, Q. Cao, C. Neumann, T. Lehnert, F. Börrnert, Y. Wang, U. Kaiser, A. Turchanin, S. Eigler, *Carbon* **2021**, *185*, 568.
[45] C. Casiraghi, A. Hartschuh, H. Qian, S. Piscanec, C. Georgi, A. Fasoli, K. S. Novoselov, D. M. Basko, A. C. Ferrari, *Nano Lett.* **2009**, *9*, 1433.
[46] A. Bellunato, H. Arjmandi Tash, Y. Cesa, G. F. Schneider, *ChemPhysChem.* **2016**, *17*, 785.
[47] M. H. Gass, U. Bangert, A. L. Bleloch, P. Wang, R. R. Nair, A. K. Geim, *Nat. Nanotechnol.* **2008**, *3*, 676.
[48] Y. An, A. F. Oliveira, T. Brumme, A. Kuc, T. Heine, *Adv. Mater.* **2020**, *32*, 2002442.
[49] P. Z. Sun, Q. Yang, W. J. Kuang, Y. V. Stebunov, W. Q. Xiong, J. Yu, R. R. Nair, M. I. Katsnelson, S. J. Yuan, I. V. Grigorieva, M. Lozada-Hidalgo, F. C. Wang, A. K. Geim, *Nature* **2020**, *579*, 229.
[50] a) S. Eigler, C. Dotzer, A. Hirsch, M. Enzelberger, P. Müller, *Chem. Mater.* **2012**, *24*, 1276; b) F. Grote, C. Gruber, F. Börrnert, U. Kaiser, S. Eigler, *Angew. Chem. Int. Ed.* **2017**, *56*, 9222.
[51] S. Grimm, M. Schweiger, S. Eigler, J. Zaumseil, *J. Phys. Chem. C* **2016**, *120*, 3036.
[52] Y. Wang, C. Neumann, M. Hußmann, Q. Cao, Y. Hu, O. Garrity, P. Kusch, A. Turchanin, S. Eigler, *Adv. Mater. Interfaces* **2021**, *8*, 2100783.
[53] P. Feicht, S. Eigler, *ChemNanoMat* **2018**, *4*, 244.
[54] a) C. E. Halbig, R. Lasch, J. Krüll, A. S. Pirzer, Z. Wang, J. N. Kirchhof, K. I. Bolotin, M. R. Heinrich, S. Eigler, *Angew. Chem. Int. Ed.* **2019**, *58*,

3599; b) Y. Wang, F. Grote, Q. Cao, S. Eigler, *J. Phys. Chem. Lett.* **2021**, *12*, 10009.
[55] T. Wei, X. Liu, M. Kohring, S. Al-Fogra, M. Moritz, D. Hemmeter, U. Paap, C. Papp, H. P. Steinrück, J. Bachmann, H. B. Weber, F. Hauke, A. Hirsch, *Angew. Chem. Int. Ed.* **2022**, *61*, e202201169.
[56] T. Wei, F. Hauke, A. Hirsch, *Adv. Mater.* **2021**, *33*, e2104060.
[57] S. Guo, S. Garaj, A. Bianco, C. Ménard-Moyon, *Nat. Rev. Phys.* **2022**, *4*, 247.
[58] R. A. Schäfer, K. Weber, M. Kolesnik-Gray, F. Hauke, V. Krstic, B. Meyer, A. Hirsch, *Angew. Chem. Int. Ed.* **2016**, *55*, 14858.
[59] L. Rodriguez-Perez, M. A. Herranz, N. Martin, *Chem. Commun.* **2013**, *49*, 3721.
[60] a) Q. Wu, Y. Wu, Y. Hao, J. Geng, M. Charlton, S. Chen, Y. Ren, H. Ji, H. Li, D. W. Boukhvalov, R. D. Piner, C. W. Bielawski, R. S. Ruoff, *Chem. Commun.* **2013**, *49*, 677; b) M. A. Bissett, S. Konabe, S. Okada, M. Tsuji, H. Ago, *ACS Nano* **2013**, *7*, 10335.
[61] T. Wei, M. Kohring, H. B. Weber, F. Hauke, A. Hirsch, *Nat. Commun.* **2021**, *12*, 552.
[62] I. Piquero-Zulaica, J. Lobo-Checa, Z. M. A. El-Fattah, J. E. Ortega, F. Klappenberger, W. Auwärter, J. V. Barth, *Rev. Mod. Phys.* **2022**, *94*, 045008.
[63] H. González-Herrero, J. M. Gómez-Rodríguez, P. Mallet, M. Moaied, J. J. Palacios, C. Salgado, M. M. Ugeda, J. Y. Veuillen, F. Yndurain, I. Brihuega, *Science* **2016**, *352*, 437.
[64] V. Strauss, R. A. Schäfer, F. Hauke, A. Hirsch, D. M. Guldi, *J. Am. Chem. Soc.* **2015**, *137*, 13079.
[65] X. Gao, Z. Wei, V. Meunier, Y. Sun, S. B. Zhang, *Chem. Phys. Lett.* **2013**, *555*, 1.
[66] S. Rahul, M. C. Rodriguez Gonzalez, S. Hirose, H. Kaneko, K. Tahara, K. S. Mali, S. De Feyter, *Nanoscale* **2023**, *15*, 10295.
[67] K. Tahara, T. Ishikawa, B. E. Hirsch, Y. Kubo, A. Brown, S. Eyley, L. Daukiya, W. Thielemans, Z. Li, P. Walke, S. Hirose, S. Hashimoto, S. De Feyter, Y. Tobe, *ACS Nano* **2018**, *12*, 11520.
[68] a) J. J. Navarro, S. Leret, F. Calleja, D. Stradi, A. Black, R. Bernardo-Gavito, M. Garnica, D. Granados, A. L. Vazquez de Parga, E. M. Perez, R. Miranda, *Nano Lett.* **2016**, *16*, 355; b) P. Szirmai, B. G. Markus, J. C. Chacon-Torres, P. Eckerlein, K. Edelthalhammer, J. M. Englert, U. Mundloch, A. Hirsch, F. Hauke, B. Nafradi, L. Forro, C. Kramberger, T. Pichler, F. Simon, *Sci. Rep.* **2019**, *9*, 19480.
[69] L. Zhou, L. Liao, J. Wang, J. Yu, D. Li, Q. Xie, Z. Liu, Y. Yang, X. Guo, Z. Liu, *Adv. Mater.* **2016**, *28*, 2148.
[70] M. Yu, C. Chen, Q. Liu, C. Mattioli, H. Sang, G. Shi, W. Huang, K. Shen, Z. Li, P. Ding, P. Guan, S. Wang, Y. Sun, J. Hu, A. Gourdon, L. Kantorovich, F. Besenbacher, M. Chen, F. Song, F. Rosei, *Nat. Chem.* **2020**, *12*, 1035.
[71] R. Hoffmann, *Angew. Chem. Int. Ed.* **1987**, *26*, 846.
[72] T. Ito, H. Shirakawa, S. Ikeda, *J. Polym. Sci., Polym. Chem. Ed.* **1975**, *13*, 1943.
[73] W. P. Su, J. R. Schrieffer, A. J. Heeger, *Phys. Rev. B* **1980**, *22*, 2099.
[74] K. Knoll, R. R. Schrock, *J. Am. Chem. Soc.* **1989**, *111*, 7989.

[75] H. Shirakawa, E. J. Louis, A. G. MacDiarmid, C. K. Chiang, A. J. Heeger, *J. Chem. Soc., Chem. Commun.* **1977**, 578.
[76] B. S. Hudson, *Materials* **2018**, *11*, 242.
[77] M. Thakur, *Macromolecules* **1988**, *21*, 661.
[78] S. Wang, Q. Sun, O. Groning, R. Widmer, C. A. Pignedoli, L. Cai, X. Yu, B. Yuan, C. Li, H. Ju, J. Zhu, P. Ruffieux, R. Fasel, W. Xu, *Nat. Chem.* **2019**, *11*, 924.
[79] a) A. C. Ferrari, J. Robertson, *Phys. Rev. B* **2001**, *63*, 121405; b) R. Pfeiffer, H. Kuzmany, P. Knoll, S. Bokova, N. Salk, B. Günther, *Diam. Relat. Mater.* **2003**, *12*, 268.
[80] K. Sonnenberg, L. Mann, F. A. Redeker, B. Schmidt, S. Riedel, *Angew. Chem. Int. Ed.* **2020**, *59*, 5464.
[81] P. H. Svensson, L. Kloo, *Chem. Rev.* **2003**, *103*, 1649.
[82] a) R. A. Hoyt, E. M. Remillard, E. D. Cubuk, C. D. Vecitis, E. Kaxiras, *J. Phys. Chem. C* **2016**, *121*, 609; b) Z. Wu, Y. Han, R. Huang, X. Chen, Y. Guo, Y. He, W. Li, Y. Cai, N. Wang, *Nanoscale* **2014**, *6*, 13196; c) N. Jung, N. Kim, S. Jockusch, N. J. Turro, P. Kim, L. Brus, *Nano Lett.* **2009**, *9*, 4133; d) S. W. Chu, S. J. Baek, D. C. Kim, S. Seo, J. S. Kim, Y. W. Park, *Synth. Met.* **2012**, *162*, 1689.
[83] L. Troian-Gautier, M. D. Turlington, S. A. M. Wehlin, A. B. Maurer, M. D. Brady, W. B. Swords, G. J. Meyer, *Chem. Rev.* **2019**, *119*, 4628.
[84] J. M. Gardner, M. Abrahamsson, B. H. Farnum, G. J. Meyer, *J. Am. Chem. Soc.* **2009**, *131*, 16206.
[85] G. Boschloo, A. Hagfeldt, *Acc. Chem. Res.* **2009**, *42*, 1819.
[86] X. Tang, T. Fan, C. Wang, H. Zhang, *Small* **2021**, *17*, e2005640.
[87] a) Y. Rho, K. Lee, L. Wang, C. Ko, Y. Chen, P. Ci, J. Pei, A. Zettl, J. Wu, C. P. Grigoropoulos, *Nat. Electron.* **2022**, *5*, 505; b) B. Li, L. Zhou, D. Wu, H. Peng, K. Yan, Y. Zhou, Z. Liu, *ACS Nano* **2011**, *5*, 5957; c) L. Zhou, L. Zhou, M. Yang, D. Wu, L. Liao, K. Yan, Q. Xie, Z. Liu, H. Peng, Z. Liu, *Small* **2013**, *9*, 1388.
[88] a) X. Zhang, T. Schiros, D. Nordlund, Y. C. Shin, J. Kong, M. Dresselhaus, T. Palacios, *Adv. Funct. Mater.* **2015**, *25*, 4163; b) W. Li, Y. Li, K. Xu, *Nano Lett.* **2020**, *20*, 534.
[89] G. Copetti, E. H. Nunes, G. K. Rolim, G. V. Soares, S. A. Correa, D. E. Weibel, C. Radtke, *J. Phys. Chem. C* **2018**, *122*, 16333.
[90] a) P. Šimek, K. Klímová, D. Sedmidubský, O. Jankovský, M. Pumera, Z. Sofer, *Nanoscale* **2015**, *7*, 261; b) A. Wang, S. Bok, C. J. Mathai, K. Gangopadhyay, J. McFarland, M. R. Maschmann, S. Gangopadhyay, *Nano Futures* **2020**, *4*, 045002; c) J. Chen, M. W. Xu, J. Wu, C. M. Li, *Nanoscale* **2018**, *10*, 9115; d) M. S. Mirshekarloo, M. C. D. Cooray, P. Jovanović, C. D. Easton, F. Wu, T. D. Gamot, M. J. Abedin, M. R. Yuce, M. Shaibani, M. Majumder, *Batter. Supercaps* **2021**, *4*, 1175; e) A. Kalicharan, J. Pitchaimani, C. Barath Kanna, V. Rajesh, M. R. Tamtam, R. Koutavarapu, P. Baby Shakila, P. Ramesh, *ChemistrySelect* **2024**, *9*, e202400820.
[91] W. Li, Y. Li, K. Xu, *Nano Lett.* **2021**, *21*, 1150.
[92] a) F. Grote, B. I. Weintrub, M. Kressler, Q. Cao, C. E. Halbig, P. Kusch, K. I. Bolotin, S. Eigler, *Small* **2024**, e2311987; b) F. Grote, S. Eigler, *Chem. Eur. J.* **2024**, e202401031.
[93] C. Backes, A. M. Abdelkader, C. Alonso, A. Andrieux-Ledier, R. Arenal, J. Azpeitia, N. Balakrishnan, L. Banszerus, J. Barjon, R. Bartali, S.

Bellani, C. Berger, R. Berger, M. M. B. Ortega, C. Bernard, P. H. Beton, A. Beyer, A. Bianco, P. Bøggild, F. Bonaccorso, G. B. Barin, C. Botas, R. A. Bueno, D. Carriazo, A. Castellanos-Gomez, M. Christian, A. Ciesielski, T. Ciuk, M. T. Cole, J. Coleman, C. Coletti, L. Crema, H. Cun, D. Dasler, D. De Fazio, N. Díez, S. Drieschner, G. S. Duesberg, R. Fasel, X. Feng, A. Fina, S. Forti, C. Galiotis, G. Garberoglio, J. M. García, J. A. Garrido, M. Gibertini, A. Gölzhäuser, J. Gómez, T. Greber, F. Hauke, A. Hemmi, I. Hernandez-Rodriguez, A. Hirsch, S. A. Hodge, Y. Huttel, P. U. Jepsen, I. Jimenez, U. Kaiser, T. Kaplas, H. Kim, A. Kis, K. Papagelis, K. Kostarelos, A. Krajewska, K. Lee, C. Li, H. Lipsanen, A. Liscio, M. R. Lohe, A. Loiseau, L. Lombardi, M. Francisca López, O. Martin, C. Martín, L. Martínez, J. A. Martin-Gago, J. Ignacio Martínez, N. Marzari, Á. Mayoral, J. McManus, M. Melucci, J. Méndez, C. Merino, P. Merino, A. P. Meyer, E. Miniussi, V. Miseikis, N. Mishra, V. Morandi, C. Munuera, R. Muñoz, H. Nolan, L. Ortolani, A. K. Ott, I. Palacio, V. Palermo, J. Parthenios, I. Pasternak, A. Patane, M. Prato, H. Prevost, V. Prudkovskiy, N. Pugno, T. Rojo, A. Rossi, P. Ruffieux, P. Samorì, L. Schué, E. Setijadi, T. Seyller, G. Speranza, C. Stampfer, I. Stenger, W. Strupinski, Y. Svirko, S. Taioli, K. B. K. Teo, M. Testi, F. Tomarchio, M. Tortello, E. Treossi, A. Turchanin, E. Vazquez, E. Villaro, P. R. Whelan, Z. Xia, R. Yakimova, S. Yang, G. R. Yazdi, C. Yim, D. Yoon, X. Zhang, X. Zhuang, L. Colombo, A. C. Ferrari, M. Garcia-Hernandez, *2D Mater.* **2020**, *7*, 022001.

[94] L. Sun, G. Yuan, L. Gao, J. Yang, M. Chhowalla, M. H. Gharahcheshmeh, K. K. Gleason, Y. S. Choi, B. H. Hong, Z. Liu, *Nat. Rev. Methods Primers* **2021**, *1*, 5.

[95] N. Kumar, R. Salehiyan, V. Chauke, O. Joseph Botlhoko, K. Setshedi, M. Scriba, M. Masukume, S. Sinha Ray, *FlatChem* **2021**, *27*, 100224.

[96] Z. Zhang, A. Fraser, S. Ye, G. Merle, J. Barralet, *Nano Futures* **2019**, *3*, 042003.

[97] H. Sun, E. W. Sirott, J. Mastandrea, H. M. Gramling, Y. Zhou, M. Poschmann, H. K. Taylor, J. W. Ager, D. C. Chrzan, *Phys. Rev. Mater.* **2018**, *2*, 094004.

[98] F. Liu, *Prog. Surf. Sci.* **2021**, *96*, 100626.

[99] P. Blake, E. W. Hill, A. H. Castro Neto, K. S. Novoselov, D. Jiang, R. Yang, T. J. Booth, A. K. Geim, *Appl. Phys. Lett.* **2007**, *91*, 063124.

[100] Y. Huang, Y. H. Pan, R. Yang, L. H. Bao, L. Meng, H. L. Luo, Y. Q. Cai, G. D. Liu, W. J. Zhao, Z. Zhou, L. M. Wu, Z. L. Zhu, M. Huang, L. W. Liu, L. Liu, P. Cheng, K. H. Wu, S. B. Tian, C. Z. Gu, Y. G. Shi, Y. F. Guo, Z. G. Cheng, J. P. Hu, L. Zhao, G. H. Yang, E. Sutter, P. Sutter, Y. L. Wang, W. Ji, X. J. Zhou, H. J. Gao, *Nat. Commun.* **2020**, *11*, 2453.

[101] J. Y. Moon, M. Kim, S. I. Kim, S. Xu, J. H. Choi, D. Whang, K. Watanabe, T. Taniguchi, D. S. Park, J. Seo, S. H. Cho, S. K. Son, J. H. Lee, *Sci. Adv.* **2020**, *6*, eabc6601.

[102] A. Castellanos-Gomez, X. Duan, Z. Fei, H. R. Gutierrez, Y. Huang, X. Huang, J. Quereda, Q. Qian, E. Sutter, P. Sutter, *Nat. Rev. Methods Primers* **2022**, *2*, 58.

[103] A. M. Dimiev, S. Eigler, *Graphene Oxide*, **2016**.

[104] A. M. Dimiev, G. Ceriotti, A. Metzger, N. D. Kim, J. M. Tour, *ACS Nano* **2016**, *10*, 274.

[105] C. E. Halbig, B. Mukherjee, S. Eigler, S. Garaj, *J. Am. Chem. Soc.* **2024**, *146*, 7431.
[106] C. Schafhaeutl, *Lond. Edinb. Dubl. Phil. Mag.* **1840**, *16*, 570.
[107] W. Rüdorff, U. Hofmann, *Z. Anorg. Allg. Chem.* **1938**, *238*, 1.
[108] B. C. Brodie, *Philos. Trans. R. Soc. London* **1859**, *149*, 249.
[109] P. P. Brisebois, M. Siaj, *J. Mater. Chem. C* **2020**, *8*, 1517.
[110] W. S. Hummers, R. E. Offeman, *J. Am. Chem. Soc.* **1958**, *80*, 1339.
[111] U. Hofmann, A. Frenzel, *Ber. Dtsch. Chem. Ges.* **1930**, *63*, 1248.
[112] J. I. Paredes, S. Villar-Rodil, A. Martinez-Alonso, J. M. Tascon, *Langmuir* **2008**, *24*, 10560.
[113] S. Eigler, M. Enzelberger-Heim, S. Grimm, P. Hofmann, W. Kroener, A. Geworski, C. Dotzer, M. Rockert, J. Xiao, C. Papp, O. Lytken, H. P. Steinruck, P. Müller, A. Hirsch, *Adv. Mater.* **2013**, *25*, 3583.
[114] P. Feicht, J. Biskupek, T. E. Gorelik, J. Renner, C. E. Halbig, M. Maranska, F. Puchtler, U. Kaiser, S. Eigler, *Chem. Eur. J.* **2019**, *25*, 8955.
[115] J. Walter, T. J. Nacken, C. Damm, T. Thajudeen, S. Eigler, W. Peukert, *Small* **2015**, *11*, 814.
[116] A. Bagri, C. Mattevi, M. Acik, Y. J. Chabal, M. Chhowalla, V. B. Shenoy, *Nat. Chem.* **2010**, *2*, 581.
[117] S. Eigler, S. Grimm, M. Enzelberger-Heim, P. Müller, A. Hirsch, *Chem. Commun.* **2013**, *49*, 7391.
[118] Y. Zhu, H. Ji, H.-M. Cheng, R. S. Ruoff, *Natl. Sci. Rev.* **2018**, *5*, 90.
[119] S. Xu, L. Zhang, B. Wang, R. S. Ruoff, *Cell. Rep. Phys. Sci.* **2021**, *2*, 100410.
[120] X. Li, W. Cai, J. An, S. Kim, J. Nah, D. Yang, R. Piner, A. Velamakanni, I. Jung, E. Tutuc, S. K. Banerjee, L. Colombo, R. S. Ruoff, *Science* **2009**, *324*, 1312.
[121] C. Mattevi, H. Kim, M. Chhowalla, *J. Mater. Chem.* **2011**, *21*, 3324.
[122] X. Li, W. Cai, L. Colombo, R. S. Ruoff, *Nano Lett.* **2009**, *9*, 4268.
[123] T. Niu, M. Zhou, J. Zhang, Y. Feng, W. Chen, *J. Am. Chem. Soc.* **2013**, *135*, 8409.
[124] V. L. Nguyen, D. J. Perello, S. Lee, C. T. Nai, B. G. Shin, J. G. Kim, H. Y. Park, H. Y. Jeong, J. Zhao, Q. A. Vu, S. H. Lee, K. P. Loh, S. Y. Jeong, Y. H. Lee, *Adv. Mater.* **2016**, *28*, 8177.
[125] Y. N. Trehan, *Z. Anorg. Allg. Chem.* **1962**, *318*, 107.
[126] a) S. Jin, M. Huang, Y. Kwon, L. Zhang, B. W. Li, S. Oh, J. Dong, D. Luo, M. Biswal, B. V. Cunning, P. V. Bakharev, I. Moon, W. J. Yoo, D. C. Camacho-Mojica, Y. J. Kim, S. H. Lee, B. Wang, W. K. Seong, M. Saxena, F. Ding, H. J. Shin, R. S. Ruoff, *Science* **2018**, *362*, 1021; b) M. Wang, M. Huang, D. Luo, Y. Li, M. Choe, W. K. Seong, M. Kim, S. Jin, M. Wang, S. Chatterjee, Y. Kwon, Z. Lee, R. S. Ruoff, *Nature* **2021**, *596*, 519.
[127] R. Zan, A. Altuntepe, *J. Mol. Struct.* **2020**, *1199*, 127026.
[128] M. Hasan, W. Meiou, L. Yulian, S. Ullah, H. Q. Ta, L. Zhao, R. G. Mendes, Z. P. Malik, N. M. Ahmad, Z. Liu, M. H. Rummeli, *RSC Adv.* **2019**, *9*, 13527.
[129] J. W. Suk, A. Kitt, C. W. Magnuson, Y. Hao, S. Ahmed, J. An, A. K. Swan, B. B. Goldberg, R. S. Ruoff, *ACS Nano* **2011**, *5*, 6916.
[130] Y. Wang, Y. Zheng, X. Xu, E. Dubuisson, Q. Bao, J. Lu, K. P. Loh, *ACS Nano* **2011**, *5*, 9927.

[131] Y. Song, W. Zou, Q. Lu, L. Lin, Z. Liu, *Small* **2021**, *17*, e2007600.
[132] C. V. Raman, K. S. Krishnan, *Nature* **1928**, *121*, 501.
[133] Z. Li, L. Deng, I. A. Kinloch, R. J. Young, *Prog. Mater. Sci.* **2023**, *135*, 101089.
[134] L. D. Ziegler, *Acc. Chem. Res.* **1994**, *27*, 1.
[135] T. Venkatarayudu, *J. Chem. Phys.* **1954**, *22*, 1269.
[136] E. J. Heller, Y. Yang, L. Kocia, *ACS Cent. Sci.* **2015**, *1*, 40.
[137] a) C. Castiglioni, M. Tommasini, G. Zerbi, *Phil. Trans. R. Soc. A* **2004**, *362*, 2425; b) E. J. Heller, Y. Yang, L. Kocia, W. Chen, S. Fang, M. Borunda, E. Kaxiras, *ACS Nano* **2016**, *10*, 2803.
[138] Y. Furukawa, N. J. Everall, in *Handbook of Vibrational Spectroscopy*, **2001**.
[139] H. E. Schaffer, R. R. Chance, R. J. Silbey, K. Knoll, R. R. Schrock, *J. Chem. Phys.* **1991**, *94*, 4161.
[140] H. Kuzmany, J. Kürti, *Synth. Met.* **1987**, *21*, 95.
[141] H. Kuzmany, *Macromol. Symp.* **1990**, *37*, 81.
[142] M. A. Schen, J. C. W. Chien, E. Perrin, S. Lefrant, E. Mulazzi, *J. Chem. Phys.* **1988**, *89*, 7615.
[143] K. Furuya, A. Sakamoto, M. Tasumi, *J. Phys. Chem. A* **2023**, *127*, 5344.
[144] A. C. Ferrari, D. M. Basko, *Nat. Nanotechnol.* **2013**, *8*, 235.
[145] P. Klar, E. Lidorikis, A. Eckmann, I. A. Verzhbitskiy, A. C. Ferrari, C. Casiraghi, *Phys. Rev. B* **2013**, *87*, 205435.
[146] L. M. Malard, M. A. Pimenta, G. Dresselhaus, M. S. Dresselhaus, *Phys. Rep.* **2009**, *473*, 51.
[147] A. C. Ferrari, J. C. Meyer, V. Scardaci, C. Casiraghi, M. Lazzeri, F. Mauri, S. Piscanec, D. Jiang, K. S. Novoselov, S. Roth, A. K. Geim, *Phy. Rev. Lett.* **2006**, *97*, 187401.
[148] A. Eckmann, A. Felten, A. Mishchenko, L. Britnell, R. Krupke, K. S. Novoselov, C. Casiraghi, *Nano Lett.* **2012**, *12*, 3925.
[149] S. J. Goldie, S. Bush, J. A. Cumming, K. S. Coleman, *ACS Appl. Nano Mater.* **2020**, *3*, 11229.
[150] B. Krauss, P. Nemes-Incze, V. Skakalova, L. P. Biro, K. Klitzing, J. H. Smet, *Nano Lett.* **2010**, *10*, 4544.
[151] F. Tuinstra, J. L. Koenig, *J. Chem. Phys.* **1970**, *53*, 1126.
[152] a) M. M. Lucchese, F. Stavale, E. H. M. Ferreira, C. Vilani, M. V. O. Moutinho, R. B. Capaz, C. A. Achete, A. Jorio, *Carbon* **2010**, *48*, 1592; b) L. G. Cançado, A. Jorio, E. H. Ferreira, F. Stavale, C. A. Achete, R. B. Capaz, M. V. Moutinho, A. Lombardo, T. S. Kulmala, A. C. Ferrari, *Nano Lett.* **2011**, *11*, 3190.
[153] P. Vecera, S. Eigler, M. Kolesnik-Gray, V. Krstic, A. Vierck, J. Maultzsch, R. A. Schäfer, F. Hauke, A. Hirsch, *Sci. Rep.* **2017**, *7*, 45165.
[154] G. Binnig, H. Rohrer, *Rev. Mod. Phys.* **1987**, *59*, 615.
[155] G. Binnig, C. F. Quate, C. Gerber, *Phy. Rev. Lett.* **1986**, *56*, 930.
[156] L. Gross, F. Mohn, N. Moll, P. Liljeroth, G. Meyer, *Science* **2009**, *325*, 1110.
[157] G. R. Heath, E. Kots, J. L. Robertson, S. Lansky, G. Khelashvili, H. Weinstein, S. Scheuring, *Nature* **2021**, *594*, 385.
[158] H. Zhang, J. Huang, Y. Wang, R. Liu, X. Huai, J. Jiang, C. Anfuso, *Opt. Commun.* **2018**, *406*, 3.
[159] a) S. Eigler, F. Hof, M. Enzelberger-Heim, S. Grimm, P. Müller, A. Hirsch, *J. Phys. Chem. C* **2014**, *118*, 7698; b) A. M. Goossens, V. E. Calado, A.

Barreiro, K. Watanabe, T. Taniguchi, L. M. K. Vandersypen, *Appl. Phys. Lett.* **2012**, *100*, 073110.
[160] K. Bian, C. Gerber, A. J. Heinrich, D. J. Müller, S. Scheuring, Y. Jiang, *Nat. Rev. Methods Primers* **2021**, *1*, 36.
[161] C. J. Shearer, A. D. Slattery, A. J. Stapleton, J. G. Shapter, C. T. Gibson, *Nanotechnology* **2016**, *27*, 125704.
[162] M. Nonnenmacher, M. P. O'Boyle, H. K. Wickramasinghe, *Appl. Phys. Lett.* **1991**, *58*, 2921.
[163] L. Kelvin, *Lond. Edinb. Dubl. Phil. Mag.* **1898**, *46*, 82.
[164] W. Melitz, J. Shen, A. C. Kummel, S. Lee, *Surf. Sci. Rep.* **2011**, *66*, 1.
[165] S. Al-Fogra, B. Yang, L. Jurkiewicz, F. Hauke, A. Hirsch, T. Wei, *J. Am. Chem. Soc.* **2022**, *144*, 19825.
[166] L. Bao, B. Zhao, B. Yang, M. Halik, F. Hauke, A. Hirsch, *Adv. Mater.* **2021**, *33*, e2101653.
[167] J. Yu, R. Giridharagopal, Y. Li, K. Xie, J. Li, T. Cao, X. Xu, D. S. Ginger, *Nano Lett.* **2021**, *21*, 3280.
[168] Z. Wang, Q. Cao, K. Sotthewes, Y. Hu, H. S. Shin, S. Eigler, *Nanoscale* **2021**, *13*, 15464.
[169] F. A. Stevie, C. L. Donley, *J. Vac. Sci. Technol. A* **2020**, *38*, 063204.
[170] H. Hertz, *Ann. Phys.* **1887**, *267*, 983.
[171] A. Einstein, *Ann. Phys.* **1905**, *322*, 132.
[172] D. E. Starr, in *Ambient Pressure Spectroscopy in Complex Chemical Environments*, **2021**, pp. 1.
[173] M. P. Seah, *Surf. Interface Anal.* **1980**, *2*, 222.
[174] a) L. Meitner, *Z. Phys.* **1922**, *9*, 131; b) P. Auger, *CR Acad. Sci(F)* **1923**, *177*, 169.
[175] G. Greczynski, R. T. Haasch, N. Hellgren, E. Lewin, L. Hultman, *Nat. Rev. Methods Primers* **2023**, *3*, 40.
[176] M. A. Kelly, *J. Electron. Spectrosc. Relat. Phenom.* **2010**, *176*, 5.
[177] M. P. Seah, I. S. Gilmore, *Phys. Rev. B* **2006**, *73*, 174113.
[178] E. B. Saloman, J. H. Hubbell, J. H. Scofield, *At. Data Nucl. Data Tables* **1988**, *38*, 1.
[179] X. Chen, X. Wang, D. Fang, *Fuller. Nanotub. Car. N.* **2020**, *28*, 1048.
[180] a) D. A. Shirley, *Phys. Rev. B* **1972**, *5*, 4709; b) J. Végh, *Surf. Sci.* **2004**, *563*, 183.
[181] W. Cao, H. Bu, M. Vinet, M. Cao, S. Takagi, S. Hwang, T. Ghani, K. Banerjee, *Nature* **2023**, *620*, 501.
[182] J. A. del Alamo, *Nature* **2011**, *479*, 317.
[183] M. Chhowalla, D. Jena, H. Zhang, *Nat. Rev. Mater.* **2016**, *1*, 16052.
[184] D. J. Frank, *IBM J. Res. Dev.* **2002**, *46*, 235.
[185] Y. Lu, B. Goldsmith, D. R. Strachan, J. H. Lim, Z. Luo, A. T. Johnson, *Small* **2010**, *6*, 2748.
[186] J. Xia, F. Chen, J. Li, N. Tao, *Nat. Nanotechnol.* **2009**, *4*, 505.
[187] S. Ghosh, S. K. Behera, A. Mishra, C. S. Casari, K. K. Ostrikov, *Energy Fuels* **2023**, *37*, 17836.
[188] C. Hwang, D. A. Siegel, S.-K. Mo, W. Regan, A. Ismach, Y. Zhang, A. Zettl, A. Lanzara, *Sci. Rep.* **2012**, *2*, 590.
[189] Z. Wang, Q. Yao, Y. Hu, C. Li, M. Hussmann, B. Weintrub, J. N. Kirchhof, K. Bolotin, T. Taniguchi, K. Watanabe, S. Eigler, *RSC Adv.* **2019**, *9*, 38011.

[190] W. Fu, L. Jiang, E. P. van Geest, L. M. Lima, G. F. Schneider, *Adv. Mater.* **2017**, *29*, 1603610.
[191] M. P. Murrell, M. E. Welland, S. J. O'Shea, T. M. H. Wong, J. R. Barnes, A. W. McKinnon, M. Heyns, S. Verhaverbeke, *Appl. Phys. Lett.* **1993**, *62*, 786.
[192] B. I. Weintrub, Y. L. Hsieh, S. Kovalchuk, J. N. Kirchhof, K. Greben, K. I. Bolotin, *Nat. Commun.* **2022**, *13*, 6601.
[193] J. Zhao, P. Ji, Y. Li, R. Li, K. Zhang, H. Tian, K. Yu, B. Bian, L. Hao, X. Xiao, W. Griffin, N. Dudeck, R. Moro, L. Ma, W. A. de Heer, *Nature* **2024**, *625*, 60.

9 List of Abbreviations

2D	two-dimensional
A	area
Å	Ångström (10^{-10} m)
a.u.	arbitrary units
AFM	atomic force microscopy
C	capacitance
C_{geo}	geometric capacitance
C_{quant}	quantum capacitance
C_{tot}	sum of geometric and quantum capacitance
C_A	maximum I_D/I_G ratio obtainable in graphene
CNP	charge neutrality point
CNT	carbon nanotube
CPD	contact potential difference
CVD	chemical vapor deposition
d	thickness
DFT	density functional theory
DOS	density of states
E_B	binding energy
E_F	Fermi energy
E_{kin}	kinetic energy
$E_{external}$	external electric field
eV	electron volts
E_{vac}	energy of the vacuum level
F	Farad
$F_{\parallel}$	force acting parallel to the graphene plane (shear force)
$F_{\perp}$	force acting perpendicular to the graphene plane (normal force)
FET	field-effect transistor
GIC	graphite intercalation compound
GNR	graphene nanoribbon
hBN	hexagonal boron nitride

HOMO	highest occupied molecular orbital
I	intensity
K	Kelvin
KPFM	Kelvin probe force microscopy
L_D	average defect distance
L_α	crystallite size
LUMO	lowest unoccupied molecular orbital
N	number of double bonds
n	charge carrier density
nm	nanometer (10^{-9} m)
oxo-	oxygen-containing
oxoG	oxo-functionalized graphene
$p_{induced}$	induced dipole moment
pm	picometer (10^{-12} m)
PMMA	polymethyl methacrylate
q_{phonon}	phonon wave vector
r_a	Radius of activated graphene area
r_s	Radius of structurally disordered area
RSF	relative sensitivity factor
s	second
STM	scanning tunnelling microscopy
V	voltage
V_{CNP}	charge neutrality point voltage
V_{CPD}	contact potential difference voltage
V_g	gate voltage
W	Watt
X	atomic fraction
XPS	X-ray photoelectron spectroscopy
α	polarizability
Γ	full width at half maximum
λ	wavelength
µm	micrometer (10^{-6} m)
v_F	Fermi velocity
Φ	work function

10 List of Publications

1.	F. Grote, S. Eigler Influence of Lattice Defects on *Trans*-Oligoene Substructure Formation in Graphene *Chem. Eur. J.* **2024**, e202401031.
2.	F. Grote, B.I. Weintrub, M. Kreßler, Q. Cao, P. Kusch, K.I. Bolotin, S. Eigler Evidence for *Trans*-Oligoene Chain Formation in Graphene Induced by Iodine *Small* **2024**, e202311987.
3.	G. Reina, C. Gabellini, M. Maranska, F. Grote, S.H. Chin, L. Jacquemin, F. Berger, P. Posocco, S. Eigler, A. Bianco The importance of molecular structure and functionalization of oxo-graphene sheets for gene silencing *Carbon* **2022**, *195*, 69.
4.	Y. Wang, F. Grote, Q. Cao, S. Eigler Regiochemically Oxo-functionalized Graphene, Guided by Defect Sites, as Catalyst for Oxygen Reduction to Hydrogen Peroxide *J. Phys. Chem. Lett.* **2021**, *12*, 10009.
5.	Q. Cao, F. Grote, M. Hußmann, S. Eigler Emerging field of few-layered intercalated 2D materials *Nanoscale Advances* **2021**, *3*, 963.
6.	A. Valimukhametova, C. Ryan, T. Paz, F. Grote, A. V. Naumov Experimental and theoretical inquiry into optical properties of graphene derivatives *Nanotechnology* **2020**, *32*, 015709.
7.	B.H. Lee, A. Valimukhametova, C. Ryan, T. Paz, F. Grote, A.V. Naumov Electric field quenching of graphene oxide photoluminescence *Nanotechnology* **2020**, *31*, 465203.
8.	S. Seiler, C.E. Halbig, F. Grote, P. Rietsch, F. Börrnert, U. Kaiser, B. Meyer, S. Eigler Effect of friction on oxidative graphite intercalation and high-quality graphene formation *Nat. Commun*. **2018**, *9*, 836.
9.	F. Grote, C. Gruber, F. Börrnert, U. Kaiser, S. Eigler Thermal Disproportionation of Oxo-Functionalized Graphene *Angew. Chem. Int. Ed.* **2017**, *56*, 9222.
10.	A.V. Naumov, F. Grote, M. Overgaard, A. Roth, C.E. Halbig, K. Nørgaard, D. M. Guldi, S. Eigler Graphene Oxide: A One versus Two-Component Material *J. Am. Chem. Soc.* **2016**, *138*, 1145.

11 Acknowledgements

First of all, I would like to thank my supervisor Prof. Dr. Siegfried Eigler for giving me the opportunity to join his group and the possibility to carry out this interesting research topic on graphene substructures. I would also like to thank him for his interest in the progress of my work, his professional support, and the creative freedom that I enjoyed in my research.

I would like to acknowledge Prof. Dr. Kannan Balasubramanian for being the second examiner of this dissertation.

I would like to thank Melanie Wellmann for her great advice and support in all organizational matters.

I am also grateful to all current and former members of the Eigler group for the pleasant working atmosphere, inspiring ideas, encouragement, and fruitful discussions. Special thanks go to Dr. Christian Halbig, Dr. Yiqing Wang, Marleen Hußmann, and Qing Cao for the successful collaboration. I would also like to thank my former students I have supervised, who worked with me on various projects and who taught me a lot.

I would also like to thank my collaborators, Prof. Dr. Bolotin, Ben Weintrub, Dr. Patryk Kusch, and Mira Kreßler for the successful partnership. Special thanks go to Ben for many fruitful discussions and support.

A big thanks to Dr. Christian Halbig for his tremendous support both inside and outside the laboratory throughout my academic career and for proofreading this thesis.

Finally, I am extremely grateful to my family and my girlfriend Pauline for their endless support throughout my studies.

12 Declaration of Authorship

I hereby declare that I alone am responsible for the content of my doctoral dissertation “Generation and Characterization of Substructures in Graphene” and that I have only used the sources or references cited in the dissertation.

Berlin, 28.05.2024

Fabian Grote